COHERENT OPTICAL STUDIES OF ELECTRONIC AND SPIN STATES IN GAAS

by

Qiong Huang

A dissertation submitted in partial fulfillment
of the requirements for the degree of
Doctor of Philosophy
(Electrical Engineering)
In The University of Michigan
2008

Doctoral Committee:

Professor Duncan G. Steel, Chair
Professor Theodore B. Norris
Professor Hebert Graves Winful
Associate Professor Luming Duan

To my mother and my wife who together made me a human being

Acknowledgements

First and most, I would like to thank my thesis advisor, Professor Duncan Steel, for the guidance and support to help me make through this unpredictable journey and learning experience which I would not obtain anywhere and anytime else. Not only did I learn how to approach problems as a physicist, but also I am influenced by his vision, attitude, passion, and the way he takes care of people. I would also like to thank my committee members: Professor Theodore B. Norris, Professor Hebert G. Winful, and Professor Luming Duan, for their teaching and encouragement.

Also, I would like to thank my lab mates, who had gone through or are going through the PhD journey with me. Dr. Elaine Li, Dr. Gurudev Dutt, Dr. Jun Cheng, and Dr. Yanwen Wu had led me into the real scientific research, without which I may not have started. Wencan He, Xiaodong Xu, Erik Kim, Hailing Chen, Dong Sun, Katherine Smirl, Bo Sun, John Schaible, and Vasudev Lal, had helped me with experiments, lab work, and especially thesis writing, without which I may not have finished.

At the end, I would like to thank my family and friends. My son has been born and grew up with my thesis work, giving me an opportunity to keep thinking about how to do research the right way. My wife has given me the most important support during the years of my study by going through all the difficult time with me. My parents also gave me the help I needed when I struggled as a graduate student parent. My friends have supported and encouraged me throughout the PhD study.

Table of Contents

List of Figures

Figure

Chapter 1

Introduction

The revolution of information technology including both computing and communication has dramatically changed human society over the past decades. Computers and cell phones have become important tools in our daily lives so that it is impossible for us to imagine how to live without them. Research on semiconductors has been well developed to provide cheap, reliable, and functional devices with high performance. As computers and cell phones become more and more powerful as well as smaller, people may wonder how long this trend will last and what will happen after the limit is reached. Far before classical information technology reaches its limits, physicists have started to ponder the future of information system and technologies. This thesis aims to address issues associated with the study and development of devices that lie beyond the limit, with the immediate focus being quantum computing.

This chapter provides a brief introduction. First, the motivation of the work is discussed, including the history and progress of quantum computing. The history of quantum computing is reviewed with a focus on selecting a good physical system to implement quantum computing. Quantum dot based quantum computing is reviewed with progress on charge and spin based quantum dot

quantum computing. Then, the research problems studied in this thesis are discussed. An outline of the thesis is presented at the end of the chapter.

1.1 Motivation for quantum computing

Semiconductor technology has produced powerful integrated circuits with low cost and small size to make complicated electronics affordable and portable. In 1965, Moore predicted that the number of transistors on a single chip would double every two years [1]. This prediction is known as Moore's law and turned out to be surprisingly accurate over the past forty years, as shown in Figure 1.1.

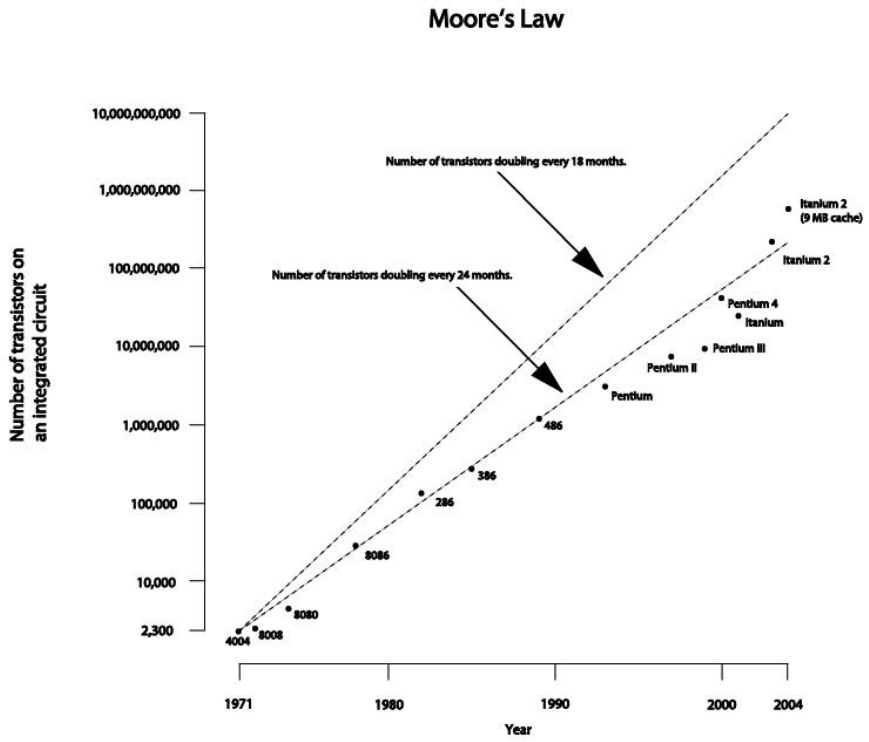

Figure 1.1 Growth of transistor counts for Intel processors (dots) and Moore's Law (logarithmic vertical scale) (from http://en.wikipedia.org/wiki/Moore's_law)

Moore explained that as the size of transistors approaches the size of atoms [2], quantum interactions will take over classical interactions in describing the physics of the devices. Current information technology is based on classical bits, defined as 0 or 1, usually represented by an ON or OFF state of a transistor. Classical information can only be processed in series in a single device, which has a fundamental limit that only allows linear increase by increasing the processing speed or number of processors. To process information faster, the operating frequency has to be increased until it hits a limit caused by either physics or engineering. To keep increasing the processing speed, parallel processing has to be used, which requires using multiple physical devices working simultaneously in the frame of classical information technology.

Quantum information aims to break this linear increase limit to gain exponential growth by parallel processing, at least for some special problems of great imporatnce. By using quantum bits (qubits), superpositions of quantum eigenstates, quantum gates can operate on multiple quantum eigenstates simultaneously. For example, a qubit is represented as $\alpha|0\rangle+\beta|1\rangle$, where $|0\rangle$ and $|1\rangle$ are the two eigenstates of a two-level system, and α and β are the population coefficients at the corresponding eigenstate. A Rabi oscillation can invert the two eigenstates simultaneously as a quantum NOT gate operation. To make a quantum computer run faster, we can increase the number of qubits rather than the operating frequency or number of processors. More importantly, the gain from increasing the number of qubits is exponential. For example, from a 2-qubits to N-qubits, the gain is 2^{N-1} rather than $\frac{N}{2}$ times.

Research for quantum computing spans from physics to computer science, including different aspects such as quantum computing algorithm design and implementation of functional quantum gates. After the Turning's classical

computing theory [3] and Shannon's information theory [4], for the first time Feynman proposed the idea of quantum computing by using quantum complexity to achieve computational capability beyond that of classical computation [5]. It took a long time for quantum computing algorithms to be developed [6-8], providing evidence that quantum computing algorithms can efficiently solve some problems that are unsolvable within a limited time (e.g. the life of the universe) for classical algorithms due to the exponential growth of the computing time. However, quantum computing algorithms can not be implemented on classical computers running on classical gates. Quantum algorithms require a quantum computer with quantum gates; that is, a physical quantum system that can represent and process information quantum mechanically [9,10]. To provide an experimental guide for implementing quantum computing algorithms, DiVincenzo listed a set of criteria with five fundamental requirements [11].

1. A scalable physical system with well characterized qubits,
2. The ability to initialize the state of the qubits to a simple initial state,
3. Long relevant decoherence times, much longer than the gate operation time,
4. A "universal" set of quantum gates,
5. A qubit-specific measurement capability.

The first criterion requires that the physical system should have a well-defined quantum system that can interact with external operations as predicted and designed, and can be scaled up to a large number of qubits without losing the performance of the operation. Physical systems not controllable or scalable are not good candidates for large scale quantum computing. The second criterion requires that the physical system should be able to be initialized to a repeatable initial state, which is the start of quantum operations. Physical systems without controllable and stable initial states can not be used for building quantum computers. The third criterion requires that the physical system needs to remain coherent during the repetitive quantum operations, since multiple quantum

operations are necessary to handle possible errors in a single quantum operation. A relevant decoherence time of 10^4 times the operations time is required before the system decoheres to achieve error corrected quantum operations. The fourth criteria requires that operations on the physical system be able to create an established universal gate such as a controlled not combined with single qubit rotations. The fifth criteria requires that the results of the quantum operation can be read out, which means that the final states after the quantum operation can be measured.

A few different approaches, including approaches based on the use of single photons, NMR, trapped ions, and QDs, have been proposed for implementing quantum computing algorithms.

Single photons can be used for quantum computing with qubits being a superposition of two orthogonal polarization states [12]. Single photon based systems have been well studied for quantum communications with experimental demonstration of long distance quantum key distribution in optical fibers [13] and free space [14]. Commercial systems for quantum key distribution to improve security are even available on the market [15]. An all-optical controlled NOT gate was also demonstrated [16]. However, the lack of stable and controllable single photon sources limits the feasibility of polarization based single photon quantum computing.

NMR can be used for quantum computing with qubits as superpositions of ensemble spin states [17]. Some quantum computing algorithms have been demonstrated on NMR quantum computing systems [18, 19]. However, the NMR systems are not practical for scalable quantum computing due to the fact that the readout signal drops exponentially when the system scales up. This is because the qubits states in NMR are not pure states and they are susceptible to thermal effects [20].

Trapped ions are good candidates for quantum computing, which satisfies all five criteria, with qubits as a superposition of spin states of single electrons [21]. Atoms and ions have nature-created stable and controllable quantum states with excellent stability (lifetime up to minutes) due to weak interactions with the environment for trapped isolated ions. Initialization, quantum operations, and read out schemes are already available by optical transitions though a history of extensive studies on the properties of atomic states. Especially due to the development of laser cooling and trapping to provide stable ions with ultra low temperature, trapped ion quantum computing has made the most advanced progress towards making a functional quantum computer. Gate operations [21-23], entanglement between multiple trapped ions [24, 25], quantum computing algorithms [26, 27], and entanglement between atoms and photons [28] have been demonstrated by experiments. By using electrodes on a chip to build multiple ion trap regions, scalability has been demonstrated [29, 30].

Semiconductor quantum dots (QDs), using a superposition of electron spin states as qubits, is another promising candidate for quantum computing that satisfies all five criteria [31,32]. Semiconductor QDs have controllable and stable quantum states that can be optically manipulated as ions or atoms. The initialization, operation, and readout can be achieved optically similar to ions through optical pumping, Rabi oscillation, and population measurement. The long decoherence time can be achieved through spin based QD quantum computing. Compared with the trapped ion quantum computing, semiconductor QD quantum computing has the scalability advantage due to its compatibility of semiconductor fabrication infrastructures.

Implementation of QD quantum computing started with optically driven population based QD quantum computing due its simplicity. One scheme is using optically excited excitons, electron-hole pairs, in QDs as qubits [33]. For

example, the absence of an exciton is defined as $|0\rangle$ and the presence of an exciton as $|1\rangle$. Quantum gate operations can be achieved by two-level Rabi oscillation. It has been shown that excitons in QDs have an average life time of around 50ps without much pure phase dephasing [34]. To achieve qubit operation, Rabi oscillations were demonstrated in a single QD [35-38]. Furthermore, the entanglement of excitons and biexcitons have been created and detected in a single dot [39-42]. A major breakthrough was the demonstration of a quantum control-ROT gate with high fidelity [43]. Besides, a density matrix mapping of qubit rotation has been measured [44]. However, due to the short lifetime of excitons, the number of operations that can be applied on exciton based qubits is limited.

To avoid the short exciton life time and to obtain a long decoherence time as required by the third criteria, electron spin can be used as the qubit [31, 45] since spin has a much longer decoherence time up to at least micro seconds [46]. The spin down state is defined as $|0\rangle$, and the spin up state is defined as $|1\rangle$. It has been shown that spin based qubits are longer-lived than the exciton qubits [31]. Spin decoherence times of at least 10ns in ensemble QDs with inhomogeneous broadening have been measured by time domain spin beats [47]. It is expected that the spin decoherence time in a single QD without inhomogeneous broadening would be much longer, since the spin relaxation time is much longer [48]. Recently, spin initializations with high fidelity have demonstrated [49, 50], and coherent control on spin states has been achieved [47, 51].

1.2 Problems studied in this thesis

To implement spin based QD quantum computing, the number of electrons in the QD needs to be controlled. Two techniques have been studied to control the

number of electrons in a single QD. One technique is to provide extra electrons by proper doping. With a silicon doping layer close to the QD layer, doped electrons can tunnel into a QD with a certain tunneling probability and get trapped in the QD. With a proper doping layer with the right doping density, thickness, and distance to the QD layer it is possible to obtain a single QD with an extra electron trapped within the QD. However, there are a few problems associated with the doped electrons. First, the doped electrons are not stable due to tunneling. The electrons that tunneled into QDs may tunnel out of QDs when the temperature changes. Second, the number of electrons within a single QD is not controllable in experiments after the sample is grown. Third, practically the possibility of getting exactly one electron in a single QD is very small due to the difficulty of controlling the doping density, position, and thickness of the doping layer in the sample growth procedure.

Another technique is to obtain extra electrons by electric injection. By adding electrodes on the top and bottom of a QD sample, a bias voltage can be applied on the QD samples [52]. Electrons can be electrically injected into the QDs and be trapped within the QDs. The electron tunneling rate depends on the applied bias voltage. With a proper sample design, the number of electrons within a single QD can be controlled by adjusting the bias voltage in experiments. The electrically gated samples give better control and a more stable system for QD study, but they also bring new problems. To put electrodes on a QD sample, thick GaAs substrates are needed, which absorb light at the exciton energy of interface fluctuation QDs (IFQDs). To study the optical properties of IFQD for spin based QD quantum computing, interaction of the light with a single IFQDs must be studied in the reflection geometry.

Another experimental challenge is how to measure the voltage dependent absorption of QDs quickly and with a high signal noise ratio (SNR). For the electrically gated QD samples, optical properties of a QD are affected by the

number of electrons in the QD, which depends on the bias voltage [53-55]. Single QD photoluminescence (PL) and absorption need to be measured over not only energy, but also bias voltage, which creates an extra dimension for the measurement. Voltage dependent PL is relatively easy because the PL can be measured with high speed and a high signal noise ratio (SNR). However, voltage dependent absorption of single QDs is challenging due to the poor SNR in single QD absorption measurements. A single QD leads to a relatively small absorption at the same level as laser noise. A single scan over laser energy measures the single QD absorption with a poor SNR; hence this requires a large number of averages to improve the SNR. Single QD absorption measurements are time consuming, and typically tens of minutes are required to obtain a single QD absorption with an acceptable SNR. For the gated sample, the absorption of a single QD needs to be repeatedly measured many times over a voltage range. The entire process is very time consuming. The available measurement time for single QD study is limited by the stability of cryogenic systems, usually on the order of tens of minutes or a few hours. Experimental techniques capable of measuring the voltage dependent absorption of a single QD with high speed and SNR needs to be developed.

Precise measurement of the electron spin decoherence time of a QD is also important for spin based QD quantum computing. The spin relaxation time limits the spin decoherence time. Most experimental techniques in laser spectroscopy study the relaxation time by resonant or above resonance energy excitation, which may affect the spin relaxation time. Recently, it was found that the measured spin relaxation time in bulk GaAs is affected by the optical excitation energy [56]. Hence, the effects of the optical excitation on spin relaxation time in semiconductor QDs needs be studied.

1.3 Thesis outline

This thesis will discuss experimental work on biased IFQDs through differential reflection (DR) and voltage modulation (VM) techniques, and spin noise measurements on n-GaAs.

Chapter 2 gives an introduction to semiconductor physics and the biased IFQD sample we used in this study. The basic optical properties of semiconductor and semiconductor QDs are briefly discussed. The energy diagrams of neutral and charged IFQDs are described. The biased IFQD sample structure is provided with characterization results by photoluminescence.

Chapter 3 discusses noise in laser spectroscopy to explain the experimental challenges in studying optical properties of single QDs. The statistics and physics of two kinds of fundamental noise, laser shot noise and electrical thermal noise, are studied. Practical noise coming from various sources including the light source, propagation, and detection are discussed. This chapter provides a foundation to understand the experimental challenges of QD study and the experimental techniques to reduce the effects of the noise on the measurements.

Chapter 4 studies the nonlinear absorption of IFQDs with the DR technique. The differential transmission (DT) technique with bandwidth reduced detection is discussed to illustrate how to measure a small signal out of a noisy background by reducing measurement bandwidth. The DT technique in the reflection geometry, DR is studied. Voltage dependent nonlinear absorption of ensemble of and single QDs from biased IFQDs samples are measured by the DR.

Chapter 5 studies the VM technique to measure the voltage dependent absorption map of single QDs with high speed and high SNR. The voltage dependent nonlinear absorption of QDs shows a quantum confined Stark effect (QCSE), which enables VM to measure the absorption of a single QD with higher speed and SNR compared with DR. The VM technique is discussed with an analytic model based on Lorentzian shaped absorption, and a numerical

simulation with a linear QCSE. The voltage dependent absorption measured by VM agrees with DR.

Chapter 6 discusses the spin noise measurement technique, which can measure the spin relaxation time with below resonance excitation and with a capability of measuring a weak signal below the apparent laser shot noise and electrical thermal noise. The physics of the spin noise measurement is discussed as a Faraday rotation caused by the weak oscillating magnetic field due to the intrinsic spin flips at the Lamor frequency, which gives a Lorentzian shaped spin noise spectrum. Spin noise measurements on an n-GaAs sample give the absolute value of electron g factor and spin relaxation time.

Chapter 7 studies the optical effects of the laser energy and intensity on the spin relaxation time in n-GaAs. The laser energy and intensity dependence of the spin noise spectra are measured. Both spin noise power and width increase dramatically when the laser energy approaches the resonance. The spin noise power fits with a two-level model with a Lorentzian shaped absorption and saturation behavior. It is found that the spin noise width has a linear relation with the optically excited ionized impurity density under the same two-level system model with a Lorentzian shaped absorption and two-level saturation behavior. By extracting the spin noise with at zero laser intensity or far below resonance, it is inferred that the spin relaxation time would be longer when there is no optical excitation.

Chapter 8 concludes the thesis with a summary and a few possible directions for future work. To apply the spin noise technique to QDs, it will be necessary to put the QD in a high Q micro-cavity. By increasing the laser energy range of the spin noise measurement, the effect of above resonance excitation can be studied. Effects of doping density and external fields on the spin relaxation time can also be studied.

Bibliography

[1] G. E. Moore, Cramming more components onto integrated circuits, Electronics 38 (1965).

[2] G. E. Moore, No Exponential is Forever...but We Can Delay 'Forever', presentation at International Solid State Circuits Conference (ISSCC) (2003).

[3] A. M. Turing, On computable numbers, with an application to the Entscheidung problem, Proc. Lond. Math. Soc. 42, 230 (1936).

[4] C. E. Shannon, A mathematical theory of communication, Bell System Tech. J. 27, 379 (1948).

[5] R. E. Feynman, American Physical Society lecture, Dec 29, 1959: There's plenty of room at the bottom, Engineering and Science, Caltech publication (1960).

[6] D. Deutsch, R. Jozsa, Rapid Solution of Problems by Quantum Computation, Proc. R. Soc. Lond. A 439, 553 (1992).

[7] P. W. Shor, Polynomial-Time Algorithms for Prime Factorization and Discrete Logarithms on a Quantum Computer, SIAM J. Comput. 26, 1484 (1997).

[8] L. K. Grover, Quantum Mechanics Helps in Searching for a Needle in a Haystack, Phys. Rev. Lett. 79, 325 (1997).

[9] J. Preskill, Lecture Notes for Physics 229: Quantum information and Computation, California Institute of Technology (September, 1998).

[10] M. A. Nielsen, I. L. Chuang, Quantum Computation and Quantum Information, Cambridge University Press, Cambridge, United Kingdom, first edition (2000).

[11] D. P. DiVincenzo, Universal quantum computation with the exchange interaction, Nature 408 (2000).

[12] D. Gottesman, I. Chuang, Quantum networks as enabling for quantum information science, Nature 402, 390 (1999).

[13] P. A. Hiskett, D. Rosenberg, C. G. Peterson, R. J. Hughes, S. Nam, A. E. Lita, A. J. Miller, J. E. Nordholt, Long-distance quantum key distribution in optical fibre, New Journal of Physics 8, 193 (2006).

[14] R. Ursin, F. Tiefenbacher, T. Schmitt-Manderbach, H. Weier, T. Scheidl, M. Lindenthal, B. Blauensteiner, T. Jennewein, J. Perdigues, P. Trojek, B. Oemer, M. Fuerst, M. Meyenburg, J. Rarity, Z. Sodnik, C. Barbieri, H.Weinfurter, A. Zeilinger, Free-Space distribution of entanglement and single photons over 144 km, Nature Physics 3, 481 (2007).

[15] http://idquantique.com
http://www.smartquantum.com
http://magiqtech.com

[16] J. L. O'Brien, G. J. Pryde, A. G. White, T. C. Ralph, D. Branning, Demonstration of an all-optical quantum controlled-not gate, Nature 426, 264 (2003).
[17] J. A. Jones, M. Mosca, Implementation of a quantum algorithm on a nuclear magnetic resonance quantum computer, Journal of Chemical Physics 109 (1998).
[18] N. Linden, H. Barjat, R. Freeman, An implementation of the Deutsch-Jozsa algorithm on a three-qubit NMR quantum computer, Chemical Physics Letters, 296 (1998).
[19] L. M. K. Vandersypen, M. Steren, G. Breyta, C. S. Yannoni, M. H. Sherwood, I. L. Chuang, Experimental realization of Shor's quantum factoring algorithm using nuclear magnetic resonance, Nature 429 (2004).
[20] S. L. Braunstein, C. M. Caves, R. Jozsa, N. Linden, S. Popescu, R. Schack, Separability of Very Noisy Mixed States and Implications for NMR Quantum Computing, Phys. Rev. Lett. 83, 1054 (1999).
[21] C. Monroe, D. Meekhof, B. King, W. Itano, D. Wineland, Demonstration of a Universal Quantum Logic Gate, Phys. Rev. Lett. 75 (1995).
[22] F. Schmidt-Kaler, H. HÄarner, M. Riebe, S. Gulde, G. P. T. Lancaster, T. Deuschle, C. Becher, C. F. Roos, J. Eschner, R. Blatt, Realization of the Cirac-Zoller controlled-NOT quantum gate, Nature 422, 408 (2003).
[23] D. Leibfried, B. DeMarco, V. Meyer, D. Lucas, M. Barrett, J. Britton, W. M. Itano, B. Jelenkovic, C. Langer, T. Rosenband, D. J. Wineland, Experimental demonstration of a robust, high-fidelity geometric two ion-qubit phase gate, Nature 422, 412 (2004).
[24] K. Molmer, A. Sirensen, Multiparticle Entanglement of Hot Trapped Ions, Phys. Rev. Lett. 82, 1835 (1999).
[25] C. A. Sackett, D. Kielpinski, B. E. King, C. Langer, V. Meyer, C. J. Myatt, M. Rowe, Q. A. Turchette, W. M. Itano, D. J. Wineland, C. Monroe, Experimental entanglement of four particles, Nature 404, 256 (2000).
[26] S. Gulde, M. Riebe, G. P. T. Lancaster, C. Becher, J. Eschner, H. HÄarner, F. Schmidt Kaler, I. L. Chuang, R. Blatt, Implementation of the DeutschCJozsa algorithm on an ion-trap quantum computer, Nature 421, 48 (2003).
[27] K.-A. Brickman, P. C. Haljan, P. J. Lee, M. Acton, L. Deslauriers, C. Monroe, Implementation of Grover's quantum search algorithm in a scalable system, Phys. Rev. A 72 (2005).
[28] B. B. Blinov, D. L. Moehring, L. M. Duan, C. Monroe, Observation of entanglement between a single trapped atom and a single photon, Nature 428, 153 (2004).
[29] D. Kielpinski, C. Monroe, D. J. Wineland, Architecture for a large-scale ion-trap quantum computer, Nature 417, 709 (2002).

[30] D. Stick, W. K. Hensinger, S. Olmschenk, M. J. Madsen, K. Schwab, C. Monroe, Ion trap in a semiconductor chip, Nature Physics 2, 36 (2006).
[31] D. Loss, D. P. Divincenzo, Quantum Computation with quantum dots, Phys. Rev. A 57, 120 (1998).
[32] A. Imamoglu, D. D. Awschalom, G. Burkard, D. P. DiVincenzo, D. Loss, M. Sherwin, A. Small, Quantum Information Processing Using Quantum Dot Spins and Cavity QED, Phys. Rev. Lett. 83, 4204 (1999).
[33] P. Chen, C. Piermarocchi, L. J. Sham, Control of Exciton Dynamics in Nanodots for Quantum Operations, Phys. Rev. Lett. 87, 067401 (2001).
[34] N. H. Bonadeo, G. Chen, D. Gammon, D. S. Katzer, D. Park, D. G. Steel, Nonlinear Nano-Optics: Probing One Exciton at a Time, Phys. Rev. Lett. 81, 2759 (1998).
[35] H. Kamada, H. Gotoh, J. Temmyo, T. Takagahara, H. Ando, Exciton Rabi Oscillation in a Single Quantum Dot, Phys. Rev. Lett. 87, 246401 (2001).
[36] T. H. Stievater, X. Li, D. G. Steel, D. Gammon, D. S. Katzer, D. Park, C. Piermarocchi, L. J. Sham, Rabi oscillations of excitons in single quantum dots, Phys. Rev. Lett. 87, 133603 (2001).
[37] A. Zrenner, E. Beham, S. Stuter, F. Findeis, M. Bichler, G. Abstreiter, Coherent properties of a two-level system based on a quantum-dot photodiode, Nature 418, 612 (2002).
[38] S. Stuer, P. Machnikowski, P. Ester, M. Bichler, V. M. Axt, T. Kuhn, A. Zrenner, Two-photon Rabi oscillations in a single InxGa1-xAs/GaAs quantum dot, Phys. Rev. B 73, 125304 (2006).
[39] G. Chen, N. H. Bonadeo, D. G. Steel, D. Gammon, D. S. Katzer, D. Park, L. J. Sham, Optically Induced Entanglement of Excitons in a Single Quantum Dot, Science 289, 1906 (2000).
[40] G. Chen, T. H. Stievater, E. T. Batteh, X. Li, D. G. Steel, D. Gammon, D. S. Katzer, D. Park, L. J. Sham, Biexciton quantum coherence in a single quantum dot, Phys. Rev. Lett. 88, 117901 (2002).
[41] X. Li, Y. Wu, D. G. Steel, D. Gammon, L. J. Sham, Raman coherence beats from the entangled state involving polarized excitons in single quantum dots", Phys. Rev. B 70, 195330 (2004).
[42] X. Li, Y. Wu, X. Xu, D. G. Steel, D. Gammon, Transient nonlinear optical spectroscopy studies involving biexciton coherence in single quantum dots, Phys. Rev. B 73, 153304 (2006).
[43] X. Li, Y. Wu, D. Steel, D. Gammon, T. H. Stievater, D. S. Katzer, D. Park, C. Piermarocchi, L. J. Sham, An All-Optical Quantum Gate in a Semiconductor Quantum Dot, Science 301, 809 (2003).
[44] Y. Wu, X. Li, L. M. Duan, D. G. Steel, D. Gammon, Density Matrix Tomography through Sequential Coherent Optical Rotations of an Exciton Qubit in a Single Quantum Dot, Phys. Rev. Lett. 96, 087402 (2006).

[45] C. Piermarocchi, P. Chen, L. J. Sham, D. G. Steel, Optical RKKY Interaction between charged semiconductor quantum dots, Phys. Rev. Lett. 89, 167402 (2002).
[46] J. R. Petta, A. C. Johnson, J. M. Taylor, E. A. Laird, A. Yacoby, M. D. Lukin, C. M. Marcus, M. P. Hanson, and A. C. Gossard, Coherent Manipulation of Coupled Electron Spins in Semiconductor Quantum Dots, Science, 309, 2180 (2005).
[47] M.V.G. Dutt, J. Cheng; B. Li; X. Xu; X. Li; P. R. Berman, D. G. Steel, A. S. Bracker, D. Gammon, S. E. Economou, R. Liu, L. J. Sham, Stimulated and Spontaneous Optical Generation of Electron Spin Coherence in Charged GaAs Quantum Dots, Phys. Rev. Lett., 94, 227403 (2005).
[48] Cheng J, Wu YW, Xu XD, et al., Spin relaxation in charged quantum dots measured by coherent optical phase modulation spectroscopy, Solid State Comm., 140, 381 (2006).
[49] M. Atatüre, J. Dreiser, A. Badolato, A. Högele, K. Karrai, and A. Imamoglu, Quantum-Dot Spin-State Preparation with Near-Unity Fidelity, Science 312, 551 (2006).
[50] X. Xu,, Y. Wu, B. Sun, Q. Huang, J. Cheng, D. G. Steel, A. S. Bracker, D. Gammon, C. Emary, L. J. Sham, Fast Spin State Initialization in a Singly Charged InAs-GaAs Quantum Dot by Optical Cooling, Phys. Rev. Lett. 99, 097401 (2007).
[51] Y. Wu, E. D. Kim, X. Xu, J. Cheng, D. G. Steel, A. S. Bracker, D. Gammon, S. E. Economou, L. J. Sham, Selective optical control of electron spin coherence in singly charged GaAs-Al0.3Ga0.7As quantum dots, Phys. Rev. Lett. 99, 097402 (2007).
[52] R. J. Warburton, C. SchÃ¤flein, D. Haft, F. Bickel, A. Lorke, K. Karrai, J. M. Garcia, W. Schoenfeld, P. M. Petroff, Optical emission from a charge-tunable quantum ring, Nature 405, 926 (2000).
[53] Regelman DV, Dekel E, Gershoni D, et al., Optical spectroscopy of single quantum dots at tunable positive, neutral, and negative charge states, Phys. Rev. B, 64, 165301 (2001).
[54] Urbaszek B, Warburton RJ, Karrai K, et al., Fine structure of highly charged excitons in semiconductor quantum dots, Phys. Rev. Lett., 90, 247403 (2003).
[55] A. S. Bracker, E. A. Stinaff, D. Gammon, M. E. Ware, J. G. Tischler, A. Shabaev, Al. L. Efros, D. Park, D. Gershoni, V. L. Korenev, and I. A. Merkulov, Optical Pumping of the Electronic and Nuclear Spin of Single Charge-Tunable Quantum Dots, Phys. Rev. Lett. 94, 047402 (2005).
[56] M. Oestreich, M. Romer, R. J. Haug, et al., Spin noise spectroscopy in GaAs, Phys. Rev. Lett. 95, 216603 (2005).

Chapter 2

Biased Semiconductor Quantum Dot Samples

The semiconductor is the most important material used to build powerful electronics devices with high performance and low cost widely used for information technologies. The massive production of high performance integrated circuit chips makes high tech products affordable for daily consumer electronics. Quantum dot (QD) based quantum computing is promising because of the feasibility to make QD based quantum computing systems and devices at low cost once the technology is developed. However, fundamental research needs to be done to understand the QD growth technique, material properties, and optical properties far before making any functional device.

Studies on QD are a large research area covering physics, materials, optics, and electrical engineering [1-5]. QD growth remains an active area of research to find ways to grow QDs with better uniformity, desired wavelength, and complicated structures like quantum dot molecules. QDs have been studied in many different areas for both fundamental physics and application devices [6-10].

This chapter will give a brief discussion about the background material properties and sample structures used in the study. First, a brief introduction of semiconductor material and its optical properties is provided. Then, QDs with discrete states are introduced with explanation of QDs used for quantum computing with different growth techniques and different charge properties. At the end of the chapter, the bias interface fluctuation QD (IFQD) sample is discussed with its structure and characterization described by photoluminescence.

2.1 Semiconductors

It is important to understand the semiconductor band structure to study semiconductor QDs. Here is a brief introduction of the band structure, while a detailed discussion is available in References [11, 12]. Crystalline solid materials, like semiconductors, are formed by a large number of atoms, usually in the order of $10^{23}/cm^3$, built on periodic lattice structures. Isolated individual atoms have discrete energy levels due to strong Coulomb interaction between nuclei and electrons. When the number of atoms is large, they can form a crystal with periodic lattice structures, leading to the formation of band structure. The energetically forbidden regions between the energy bands are called bandgaps. Electrons are filled from the lowest energy band to the higher energy bands. The highest energy band filled with electrons can be either completely filled or partially filled. Without any thermal or optical excitation, the crystal with the highest energy band partially filled is a metal, characterized by good electric and thermal conductivity, and the crystal with the highest energy band completely filled is an insulator or a semiconductor (depending on the bandgap), characterized by poor electric and thermal conductivity.

The last filled energy band is called the valance band and the unfilled energy band above the valance band is called conduction band. The energy difference between the valance band and conduction band, called bandgap energy, determines the electric and optical properties of the crystal. Crystals with the highest energy band completely filled and with the bandgap energy larger than the energy of thermal and optical excitation are insulators. Crystals with the highest energy band completely filled and with the bandgap energy comparable with the energy of thermal and optical excitation are semiconductors. With thermal or optical excitation, the electrons in semiconductors can be excited from the valance band into the conduction band, leaving equivalent positive changes in the valence band, called holes. The electron- hole pair generation causes the phonon energy from thermal excitation or the photon energy from optical energy to be absorbed. The recombination of an electron-hole pair may emit a phonon or photon.

GaAs is the most commonly used semiconductor material for optoelectronics. It is an III-V compound semiconductor with a cubic crystal structure, which has a lack of inversion symmetry. The crystal structure and the bandgap energy diagram of bulk GaAs are shown in Figure 2.1.

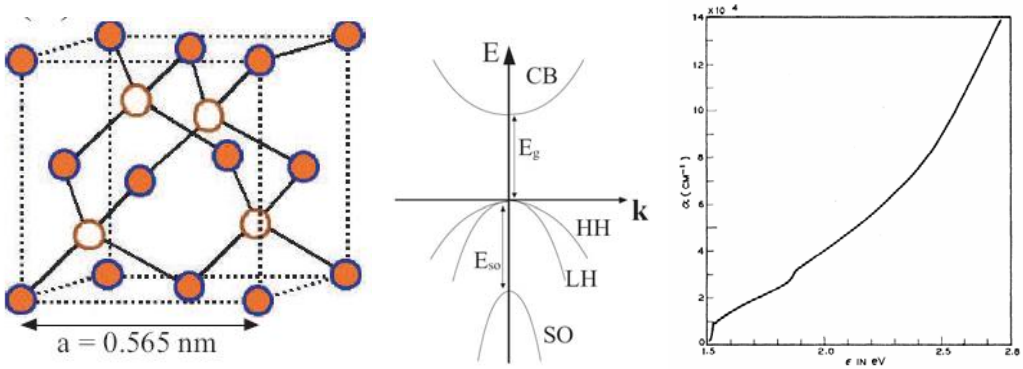

(a) (b) (c)

Figure 2.1 (a) Crystal structure of GaAs (b) expanded view of GaAs band structure near k~0 (bandgap energy E_g is 1.519eV) (c) optical absorption in bulk GaAs [13]

Optical properties of semiconductor are characterized by its laser energy dependent absorption and luminescence. Semiconductors are transparent to the light with energy below the bandgap energy, and have strong absorption of light with energy above the bandgap energy. The transition from transparency to strong absorption is called the Urbach tail, where impurity absorption dominates. Optical absorption of GaAs is shown in Figure 2.1(c).

The optical absorption of semiconductors can be understood with the band structure. Light with energy lower than the bandgap energy can not be absorbed since the photon energy is not enough to excite electrons from valence band to conduction band. Light with energy above the bandgap energy is strongly absorbed since the photons excite electron-hole pairs. The electron-hole pair may recombine and emit a photon, which gives photoluminescence. Since the optical transitions are associated with electron energy states, optical absorption and photoluminescence give information about the energy states in the semiconductor

materials, but absorption and photoluminescence may give different energy states since they are different processes.

Depending on the Bohr radius and de-Broglie wavelength, the optically generated electron and hole can be either non-interacting particles or be bounded as an interacting exciton subjected to the Coulomb interaction, like a positronium atom. Since an electron has a negative charge and a hole has a positive charge, the binding energy of an exciton is negative, about -5meV in GaAs.

2.2 Semiconductor quantum dots

In bulk semiconductor, excited electrons may have any energy over a continuous energy spectrum. Quantum confinement, for example, an abrupt energy change over a small spatial region comparable with the electron wave function, will lead to quantization of energy, causing the energy states available to electrons changing from continuous to discrete.

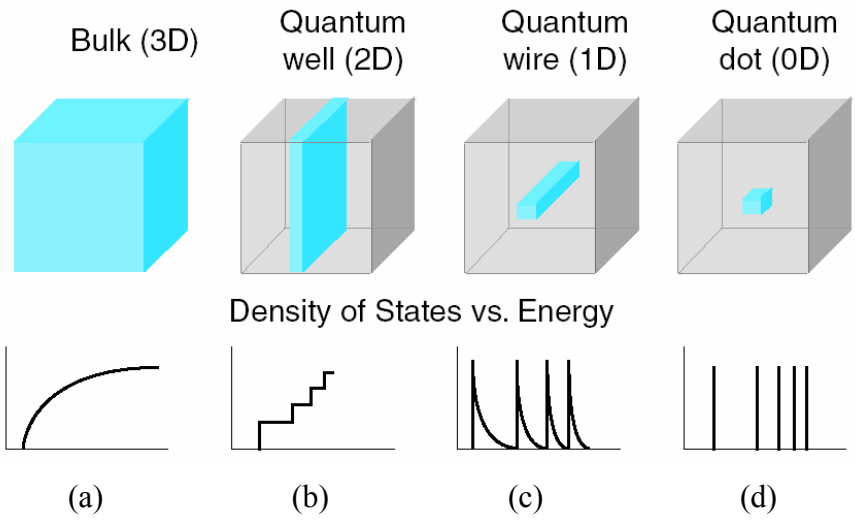

Figure 2.2 DOS of semiconductors with different level of quantum confinements (a) 3D bulk (b) 2D quantum well (c) 1D quantum wire (d) 0D quantum dot

The density of states electrons can occupy over a unit energy range can be calculated as the Density of State (DOS) [12]. Figure 2.2 shows the DOS for systems with different level of confinement. Bulk semiconductors, a 3D structure

without any confinement, have a continuous DOS. Quantum wells, a 2D structure with one-dimensional confinement, have step like DOS. Quantum wires, a 1D structure with two-dimensional confinement, have a palm like DOS. Quantum dots, a 0D structure with the ultimate three-dimensional confinement provides delta function like DOS. The DOS of the bulk, quantum well, quantum wire, and quantum dot can be represented as,

3D bulk: $$DOS_{3D}(E) = \frac{1}{2\pi^2}\left(\frac{2m}{\hbar^2}\right)^{\frac{3}{2}}\sqrt{E}$$

2D quantum well: $$DOS_{2D}(E) = \frac{m}{\pi\hbar^2}\sum_i \Theta(E - E_i)$$

1D quantum wire: $$DOS_{1D}(E) = \frac{1}{\pi}\left(\frac{m}{2\hbar^2}\right)^{\frac{1}{2}}\sum_{i,j}\frac{1}{E - E_{ij}}$$

0D quantum dot: $$DOS_{0D}(E) = 2\sum_{i,j,k}\delta(E - E_{ijk})$$

where Θ is the Heavyside step function, and δ is the Dirac delta function.

Quantum confinement gives discrete energy states, which is similar to atoms with discrete states due to strong confinement and Coulomb interaction. The exact energy of the discrete states depends on the strength of confinement, size and shape of QDs, which can be controlled in the material growth. It is possible to make QDs with controllable discrete states, so QDs are also called “artificial atoms”.

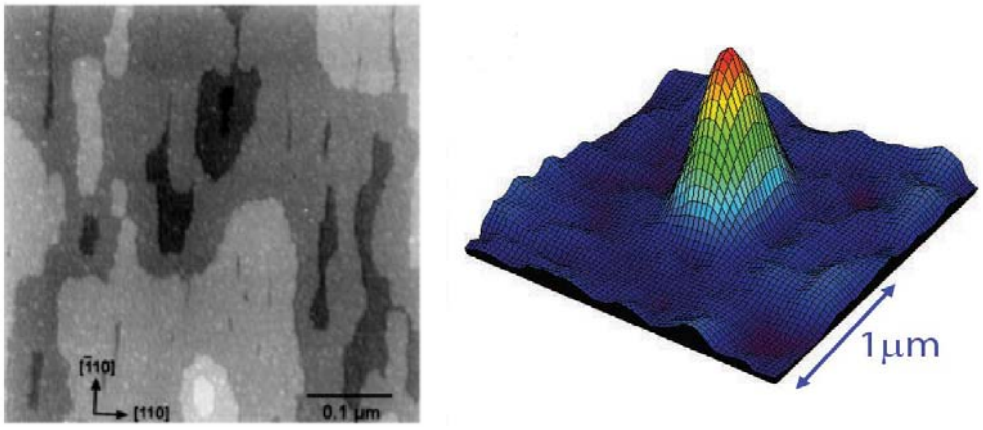

(a) (b)

Figure 2.3 (a) STM image of QDs [13] (b) NSOM image of a single QD [14]

Usually the size of the confinement in a few to tens of nm, and the energy change is a few hundred or thousand meV in QDs. Due to this strong confinement in a size smaller than the electron de-Broglie wavelength, the wave function of exciton in localized within a QD. Figure 2.3(a) shows a scanning tunneling microscope (STM) image of QDs for a cross section along the growth direction [13]. The near-field scanning optical microscopy (NSOM) image of a single QD shows that the exciton wave function is localized in a confined area, shown in Figure 2.3(b) [14].

Due to the feature of discrete energy states and large oscillator strength, QDs have been extensively studied for a wide range of quantum optical phenomena, including the quantum confined Stark effect [15], quantum interference [16], photon antibunching [17], electromagnetically induced transparency [18], spin blockade [19], and Autler-Townes splitting [20]. QDs have also being extensively studied to make application devices with better performances than current devices. QD lasers have the advantage of low threshold current, high output power and efficiency, and better temperature independence. Significant efforts have been made to make QD lasers running at room temperature commercially available [21-25]. QDs photodetectors have the advantage of low dark current and high temperature operation [26-30]. QDs modulators have the advantage of high efficiency and broad frequency range [31-32]. Our interest is using QDs for quantum computing.

2.2.1 Semiconductor QDs for quantum computing

Many different QDs have been grown with different techniques including electrostatically and lithographically defined QDs [33-38], chemically synthesized QDs [39-44], interface fluctuation QDs (IFQD) [45-49], and self-assembled QDs (SAQD) [50-53]. The QDs used for optically driven QD quantum computing are mainly the last two kinds of QDs.

IFQDs are formed by the clustering of atoms caused by growth interruption when a QW is grown [46]. The GaAs/$Al_{0.3}Ga_{0.7}As$ IFQDs used for QD quantum computing are random islands of GaAs clusters surrounded by $Al_{0.3}Ga_{0.7}As$ with a

vertical height of a few nm and a lateral size around 40~100 nm. From the STM image shown in Figure 2.3(a), the IFQDs are randomly distributed with irregular shapes elongated along one direction. Since the bandgap energy is 1.52eV for GaAs and 1.95eV for $Al_{0.3}Ga_{0.7}As$, the vertical confinement energy is about 0.43eV. The dipole momentum measured from single IFQD absorption is around 60~100 Debye [13]. Due to its relatively large dipole compared with SAQD, IFQD gives a relatively strong optical absorption, which makes it easier to measure signals in experiments.

SAQDs are clusters of atoms formed naturally with regular shapes by the strain caused by lattice mismatch when growing a different material on an expitaxial surface [50]. InAs/GaAs SAQDs used for QD quantum computing are disk or pyramid shaped clusters of InAs atoms surrounded by GaAs with a vertical confinement of around 3nm and a lateral size of around 20nm. Since the bandgap energy is 0.43eV for InAs and 1.52eV for GaAs, the confinement energy in SAQD is about 1.09eV. Compared with IFQDs, SAQDs have stronger confinement and smaller dipole momentum. Different from IFQDs, the height and location of SAQDs can be controlled by growth processes, which provides possibilities to grow desired SAQDs with certain energy and patterned spatial distributions [53]. This engineering capability makes SAQDs a primary focus for semiconductor QD study and research. However, small dipole moments give small optical signals, which requires more sensitive experimental techniques.

2.2.2 Neutral and charged quantum dots

To implement spin based QD quantum computing, extra electrons are introduced into QDs. Depending on the initial charging state, neutral or charged, the optical property of the QD can be different.

A neutral QD absorbs a photon and generates an exciton. Due to the selection rules, only two transitions are optically allowed. For ideally symmetric QDs, circular polarization is expected. However, in real QDs, linear polarization is observed due to the asymmetry in QDs, which is elongated along y direction in the IFQD we studied, as shown in Figure 2.3(a). The energy diagram of a neutral

exciton is shown in Figure 2.4(a). Due to the lateral asymmetry, there is a small splitting of about 25μeV between the horizontal and vertical polarization [13].

For the exciton population based QD quantum computing, the qubit is a superposition of the population of the two level system composed of the crystal ground state (no exciton) and the exciton state. The decoherenece time is limited by the exciton decay time in the QDs, usually in the order of 100ps, since not much pure dephasing was observed in these QDs [54]. Even with ultrafast laser pulse with a pulse width of tens of fs, the number of operations within the decoherence time is limited. However, the simplicity of the exciton population based QD quantum computing makes it a good starting system to make fast and significant progresses, including exciton Rabi oscillation [55], entanglement between two excitons [56], a two-qubit controlled ROT gate [57], and density matrix tomography of a qubit [59].

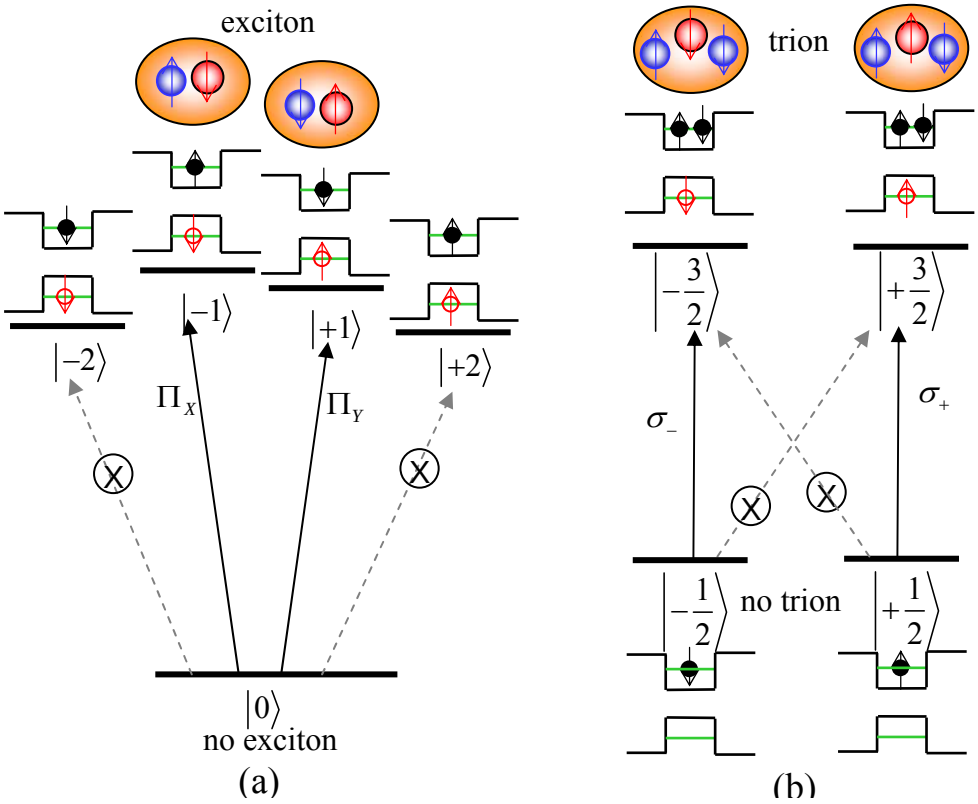

Figure 2.4 Bandgap energy level diagram and two level representation for (a) excitons and (b) trions (CB and VB stand for conduction band and valence band.)

For a charged QD, an optically generated exciton can combine with the extra electron existing in the QD to form a charged exciton, two electrons and one hole, called trion. The selection rule is circular due to the Pauli principle. Only the left and the right transitions are allowed due to the selection rule. The energy diagram is shown in Figure 2.4(b). In our study of IFQD, no magnetic field is applied. The selection rule will be different when a magnetic field exists. The two cross transitions can be turned on by applying a magnetic field, which allow the two spin states optically coupled by a shared trion state. Detailed study about the trion coupled spin states can be found in Reference [59-61].

For the spin based QD quantum computing, the qubit is a superposition of the population of a two level system composed of electron spin states. By optically manipulating the electron spin states through the trion states, optically driven spin based QD quantum computing can be implemented. The electron spin has a long decoherence time up to microsecond, which allows 10^7 or more quantum operation with fs ultrafast laser pulses. Even through the trion life time (in the order of 100ps) is much shorter than the spin decoherence time, it does not limit the speed of operation. To experimentally manipulate the trion state, it becomes important to understand the optical properities of exciton and trions in QDs.

2.3 Biased Interface Fluctuation Quantum Dot Samples

The sample we studied is an electrically gated or biased, IFQD sample as illustrated in Figure 2.5(a). It is a 4.2nm GaAs QW sandwiched between two 50nm $Al_{0.3}Ga_{0.7}As$ layers grown on a GaAs substrate. A thin titanium oxide layer is deposited above the 50nm capping $Al_{0.3}Ga_{0.7}As$ layer to serve as an electrode and an Al mask layer is laid on top to provide 25μm-diameter apertures for ensemble study, and sub-micron-sized small apertures for single dot study. A bias voltage can be applied across the sample through the substrate and the Ti/Al layer. With a bias voltage, an applied electric field adjusts the QD energy state with respect to the Fermi energy level, as shown in Figure 2.5(b), and the number of extra electrons tunneled into the QD can be controlled. Within a certain bias voltage range, there is no electron in the QD. Under optical excitation caused by a

laser beam, a neutral exciton is created in the QD, illustrated in Figure 2.5(a) as X. Within a given voltage range, only one electron can tunnel and be trapped in the QD. Under the optical excitation where an exciton is created, the extra electron will bind with the exciton in the QD to form a trion, labeled in Figure 2.5(a) as X^-, with energy a few meV below the exciton. A transition from exciton to trion occurs when the bias voltage is adjusted continuously over the exciton-trion voltage range. By measuring the bias voltage dependent absorption and photoluminescence of the QD, we can study the optical signature of the exciton-trion transition.

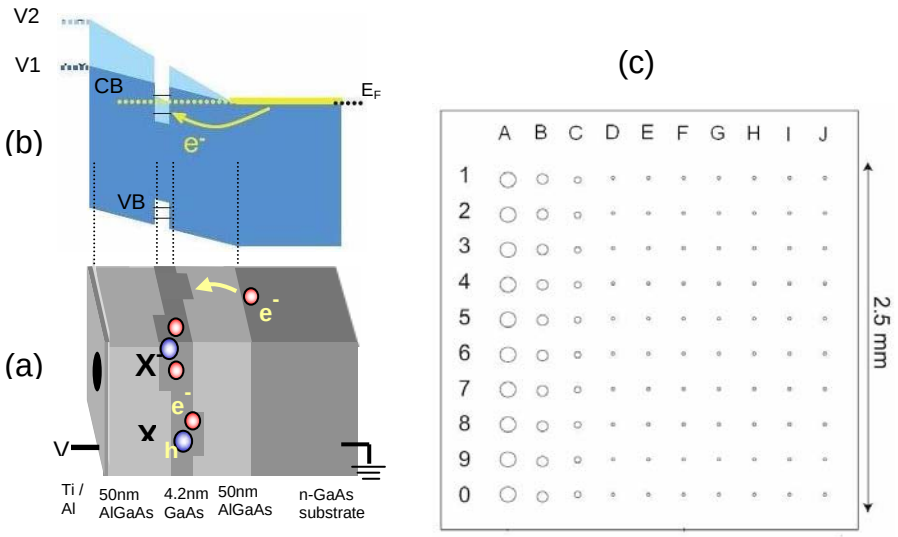

Figure 2.5 Biased IFQD sample (a) structure (not to scale) (X and X^- represent exciton and trion (b) charging scheme (CB and VB stand for conduction band and valence band. E_F represents Fermi energy) (c) aperture map

Figure 2.5(c) shows the aperture map on the sample. The dots density of the sample is about 1QD/μm^2. Under a big aperture with a diameter about 25μm, ensemble of QDs in the order of a few hundred QDs is studied. Due to the difficulty of controlling QD size and confinement, the ensemble QD shows an inhomogeneous broadening. With a small aperture with a diameter less than a micron, the QD density gives a an average of one QD per aperture, single QD can be studied due to the low possibility of two QDs under one small aperture having

the exact same energy. It has proved that the aperture provides an effective method to study optical properties of single QDs [46].

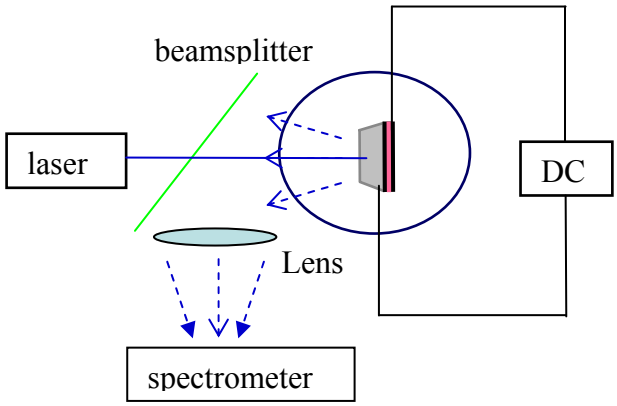

Figure 2.6 PL setup

The sample is characterized by photoluminescence (PL) in order to obtain the energy states of QDs. As shown by Figure 2.6, a green laser beam at 540nm or a red laser beam at 700nm is focused on the sample. The laser excitation creates excitons or trions in the sample, and they recombine to generate photo luminescence emission coming out of the sample from all directions. Due to the fact that the GaAs substrate absorbs the luminescence light going in the forward direction, the luminescence light going to the backward direction is collected in reflection geometry with a beam splitter and a lens directed to a spectrometer.

For biased IFQD, PL as function of energy and voltage need to be measured to obtain a bias voltage dependent PL map, which provides an optical signature of excitons and trions in QDs. Figure 2.7 shows the PL map measured for an ensemble of IFQDs through a 25μm aperture and for single IFQDs through a sub-micron aperture. Figure 2.7(a) shows the PL map of ensemble QDs. In the voltage range from -2V to -1.3V, the PL has about 2meV FWHM centered at 1630meV. In the voltage range from -1.2V to 1V, the PL is centered at 1627.5meV with the same FWHM. Based on the width of the PL peak, the energy separation between the two peaks, and the corresponding voltage, the peak at 1630meV in the voltage range from -2V to -1.3V is assigned as possible excitons; the one at 1627.5meV in the voltage range from -1.2V to 1V is assigned as possible trions [62, 63].

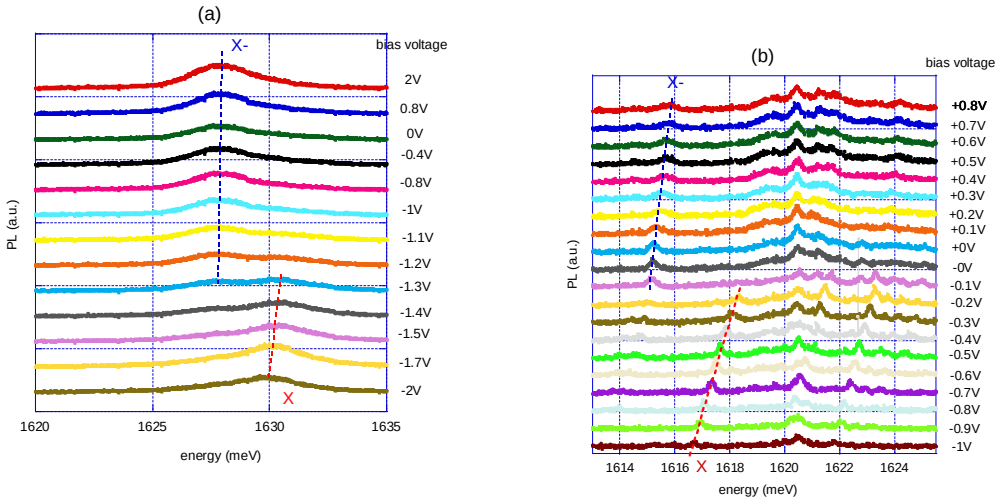

Figure 2.7 PL maps of biased IFQDs (a) ensemble QDs (b) single QDs

Figure 2.7(b) shows the PL map of single QDs through a sub-micron aperture. Following the exciton-trion transition feature, the PL peak around 1617meV-1618meV appeared in the voltage range from -1V to -0.2V is assigned as a possible exciton, labeled as X. The peak around 1615meV-1616meV existing in the voltage range from -0.1V to 0.8V is assigned as a possible trion, labeled as X-. Verification of exciton or trion needs more careful investigation including polarization, power dependence, and temperature dependence. Since our interest is in absorption rather than PL, here we just provide a simple characterization to find out the energy ranges of the QDs for absorption studies to be discussed later.

In summary, semiconductor QD samples used for this thesis work were discussed in this chapter. Semiconductor materials are introduced with the band theory to explain their optical properties. Semiconductor QDs were discussed to show their discrete energy states. Semiconductor QDs for quantum computing were reviewed with their properties. Neutral and charged QDs were introduced to illustrate why we need to study absorption of single QDs. At the end, the biased IFQD sample for this thesis work was discussed with its structure. Characterization of the biased IFQD sample by PL map showed optical signatures of exciton-trion transition in both ensemble QDs and a single QD.

Bibliography

[1] D. Bimberg, M. Grundmann, N. N. Ledentsov, Quantum Dot Heterostructures, Wiley, Chichester, 1999.

[2] M. Grundmann (Ed.), Nano-optoelectronics concepts, physics and devices, Springer, Berlin, 2002.

[3] V.A. Shchukin, N.N. Ledentsov, D. Bimberg, Epitaxy of nanostructures, Springer, Berlin, 2003.

[4] M.S. Skolnick, D. J. Mowbray, Self-assembled semiconductor quantum dots: Fundamental physics and device applications, Annual Review of Materials Research, 34, 181 (2004).

[5] D. J. Mowbray, M. S. Skolnick, New physics and devices based on self-assembled semiconductor quantum dots, Journal of Physics D: Applied Physics, 38, 2059 (2005).

[6] S. Franchi, G. Trevisi, L. Seravalli, P. Frigeri, Quantum dot nanostructures and molecular beam epitaxy, Progress in Crystal Growth and Characterization of Materials, v 47, n 2-3, Vapour Growth of Bulk Crystals and Expitaxy: Part I, 2005, p 166-195

[7] E. Beham, M. Betz, S. Trumm, M. Kroutvar, Y. Ducommun, H. J. Krenner, M. Bichler, A. Leitenstorfer, J. J. Finley, A. Zrenner, G. Abstreiter, Physics and applications of self-assembled quantum dots, Physica Status Solidi C: Conferences, v 1, n 8, 2004, p 2131-2159

[8] M. Grundmann, The Present Status of Quantum Dot Lasers, Physica E 5, 167 (2000).

[9] A. D. Yoffe, Semiconductor quantum dots and related systems: electronic, optical, luminescence and related properties of low dimensional systems, Advances in Physics, 50, 1 (2001).

[10] Arakawa, Yasuhiko, Progress in self-assembled quantum dots for optoelectronic device application, IEICE Transactions on Electronics, v E85-C, n 1 SPEC., January, 2002, 37-44

[11] N. Peyghambarian, S. W. Koch, A. Mysyrowicz, Introduction to Semiconductor Optics, Prentice-Hall, Inc, New Jersey, first edition (1993).

[12] N. W. Ashcroft, N. D. Mermin, Solid State Physics, Thomson Learning, Inc, USA, first edition (1976).

[13] D. Gammon, E. S. Snow, B. V. Shanabrook, D. S. Katzer, D. Park, Fine Structure Splitting in the Optical Spectra of Single GaAs Quantum Dots, Phys. Rev. Lett. 76, 3005 (1996).

[14] J. R. Guest, T. H. Stievater, G. Chen, E. A. Tabak, B. G. Orr, D. G. Steel, D. Gammon, D. S. Katzer, Near-Field Coherent Spectroscopy and Microscopy of a Quantum Dot System, Science 293, 2224 (2001).

[15] S. A. Empedocles, M. G. Bawendi, Quantum-Confined Stark Effect in Single CdSe Nanocrystallite Quantum Dots, Science 278, 2114 (1997).

[16] N. H. Bonadeo, J. Erland, D. Gammon, D. Park, D. S. Katzer, D. G. Steel, Coherent optical control of the quantum state of a single quantum dot, Science 282, 1473 (1998).

[17] P. Michler, A. Imamoglu, M. D. Mason, P. J. Carson, G. F. Strouse, S. K. Buratto, Quantum correlation among photons from a single quantum dot at room temperature, Nature 406, 968 (2000).
[18] M. Phillips, H. Wang, Spin Coherence and Electromagnetically Induced Transparency via Exciton Correlations, Phys. Rev. Lett. 89, 186401 (2002).
[19] M. Pioro-Ladriμere, M. Ciorga, J. Lapointe, P. Zawadzki, M. Korkusiski, P. Hawrylak, A. S. Sachrajda, Spin-Blockade Spectroscopy of a Two-Level Artificial Molecule, Phys. Rev. Lett. 91, 026803 (2003).
[20] X. Xu, B. Sun, P. R. Berman, D. G. Steel, A. S. Bracker, D. Gammon, L. J. Sham, Coherent Optical Spectroscopy of a Strongly Driven Quantum Dot, Science, 317, 929 (2007).
[21] N. Kirstaedter, N. Ledentsov, M. Grundmann, D. Bimberg, V. Ustinov, S. Ruvimov, M. Maximov, P. Kopμev, Z. Alferov, U. Richter, P. Werner, U. GÄosele, J. Heydenreich, Low threshold, large To injection laser emission from (InGa)As quantum dots, Electron. Lett. 30, 1416 (1994).
[22] K. Kamath, P. Bhattacharya, T. Sosnowski, T. Norris, J. Phillips, Room-temperature operation of In0:4Ga0:6As/GaAs self-organised quantum dot lasers, Electronics Letters 32, 1374 (1996).
[23] R. Mirin, A. Gossard, J. Bowers, Room temperature lasing from InGaAs quantum dots, Electron. Lett. 32, 1732 (1996).
[24] R. L. Sellin, C. Ribbat, M. Grundmann, N. N. Ledentsov, D. Bimberg, Close-to-ideal device characteristics of high-power InGaAs/GaAs quantum dot lasers, Appl. Phys. Lett. 78, 1207 (2001).
[25] R. L. Sellin, C. Ribbat, D. Bimberg, F. Rinner, H. Konstanzer, M. T. Kelemen, M.Mikulla, High-reliability MOCVD-grown quantum dot laser, Electron. Lett. 38, 883 (2002).
[26] Xu SJ, Chua SJ, Mei T, et al., Characteristics of InGaAs quantum dot infrared photodetectors, Appl. Phys. Lett., 73, 3153 (1998).
[27] Stiff AD, Krishna S, Bhattacharya P, et al., Normal-incidence, high-temperature, mid-infrared, InAs-GaAs vertical quantum-dot infrared photodetector, IEEE Journl. Quan. Elec., 37, 1412 (2001).
[28] Jiang L, Li SS, Yeh NT, et al., In0.6Ga0.4As/GaAs quantum-dot infrared photodetector with operating temperature up to 260 K, Appl. Phys. Lett., 82, 1986 (2003).
[29] Bhattacharya P, Su XH, Chakrabarti S, et al., Characteristics of a tunneling quantum-dot infrared photodetector operating at room temperature, Appl. Phys. Lett., 86, 191106, (2005).
[30] Lim H, Tsao S, Zhang W, et al., High-performance InAs quantum-dot infrared photodetectors grown on InP substrate operating at room temperature, Appl. Phys. Lett., 90, 131112 (2007).
[31] Sahara R, Matsuda M, Shoji H, et al., Proposal for quantum-dot electroabsorption modulator, IEEE Photo. Tech. Lett., 8, 1477 (1996).
[32] Malins DB, Gomez-Iglesias A, White SJ, et al., Ultrafast electroabsorption dynamics in an InAs quantum dot saturable absorber at 1.3 um , Appl. Phys. Lett., 89, 171111 (2006).

[33] K. Brunner, U. Bockelmann, G. Abstreiter, M. Walther, G. BÄohm, G. TrÄankle, G. Weimann, Photoluminescence from a single GaAs/AlGaAs quantum dot, Phys. Rev. Lett. 76, 3216 (1992).
[34] R. Steren, T. Koch, J. Oshinowo, F. Faller, A. Forchel, Photoluminescence study of deep etched InGaAs/GaAs quantum wires and dots de¯ned by low-voltage electron beam lithography, Appl. Phys. Lett. 68, 223 (1995).
[35] U. Bockelmann, P. Roussignol, A. Filoramo, W. Heller, G. Abstreiter1, K. Brunner, G. BÄohm, G. Weimann, Time resolved spectroscopy of single quantum dots: Fermi gas of excitons, Phys. Rev. Lett. 76, 3622 (1996).
[36] W. Wegscheider, G. Schedelbeck, G. Abstreiter, M. Rother, M. Bichler, Atomically precise GaAs/AlGaAs quantum dots fabricated by twofold cleaved edge overgrowth, Phys. Rev. Lett. 79, 1917 (1997).
[37] U. Bockelmann, W. Heller, A. Filoramo, P. Roussignol, Microphotolumines cence studies of single quantum dots. I. Time-resolved experiments, Phys. Rev. B 55, 4456 (1997).
[38] U. Bockelmann, W. Heller, G. Abstreiter, Microphotoluminescence studies of single quantum dots. II. Magnetic field experiments, Phys. Rev. B 55, 4469 (1997).
[39] A. Eychmuller, A. Mews, H. Weller, A quantum-dot quantum-well CdS/HgS/CdS, Chem. Phys. Lett. 208, 59 (1993).
[40] A. P. Alivisatos, Semiconductor clusters, nanocrystals, and quantum dots, Science 271, 933 (1996).
[41] M. A. Hines, P. Guyot-Sionnest, Synthesis and characterization of strongly luminescing ZnS-capped CdSe nanocrystals, J. Phys. Chem. 100, 468 (1996).
[42] X. G. Peng, M. C. Schlamp, A. V. Kadavanich, A. P. Alivisatos, Epitaxial growth of highly luminescent CdSe/GdS core/shell nanocrystals with photostability and electronic accessibility, J. Am. Chem. Soc. 119, 7019 (1997).
[43] M. Bruchez, Jr., M. Monronne, P. Gin, S. Weiss, A. P. Alivisatos, Semiconductor nanocrystals as fluorescent biological labels, Science 281, 2013 (1998).
[44] W. C. W. Chan, S. Nie, Quantum dot bioconjugates for ultrasensitive nonisotopic detection, Science 281, 2016 (1998).
[45] A. Zrenner, L. V. Butov, M. Hagn, G. Abstreiter, G. BÄohm, G. Weimann, Quantum dots formed by interface fluctuations in AlAs/GaAs coupled quantum well structures, Phys. Rev. Lett. 72, 3382 (1994).
[46] D. Gammon, E. S. Snow, B. V. Shanabrook, D. S. Katzer, D. Park, Homogeneous Linewidths in the Optical Spectrum of a Single Gallium Arsenide Quantum Dot, Science 273, 87 (1996).
[47] Q. Wu, R. D. Grober, D. Gammon, D. S. Katzer, Imaging Spectroscopy of Two-Dimensional Excitons in a Narrow GaAs/AlGaAs Quantum Well, Phys. Rev. Lett. 83, 2652 (1999).
[48] J. G. Tischler, A. S. Bracker, D. Gammon, D. Park, Fine Structure of Trions and Excitons in Single GaAs Quantum Dots, Phys. Rev. B 66, 081310 (2002).

[49] A. ThrÄanhardt, C. Ell, G. Khitrova, H. M. Gibbs, Anisotropic emisinterface fluctuation quantum dots, Eur. Phys. J. B 27, 571 (2002).
[50] P. M. Petro, S. P. DenBaars, MBE and MOCVD growth and properties of self-assembling quantum dot arrays in III-V semiconductor structures, Superlattices and Microstructures 15, 15 (1994).
[51] D. J. Eaglesham, M. Cerullo, Dislocation-free Stranski-Krastanow growth of Ge on Si (100), Phys. Rev. Lett. 64, 1943 (1994).
[52] N. Richard, Self-organized growth of quantum dot structures, Semicond. Sci. Tech. 11, 1365 (1996).
[53] P. M. Petro, A. Lorke, A. Imamoglu, Epitaxially self-assembled quantum dots, Physics Today 54, 46 (2001).
[54] N. H. Bonadeo, G. Chen, D. Gammon, D. S. Katzer, D. Park, D. G. Steel, Nonlinear Nano-Optics: Probing One Exciton at a Time, Phys. Rev. Lett. 81, 2759 (1998).
[55] T. H. Stievater, X. Li, D. G. Steel, D. Gammon, D. S. Katzer, D. Park, C. Piermarocchi, L. J. Sham, Rabi oscillations of excitons in single quantum dots, Phys. Rev. Lett. 87, 133603 (2001).
[56] G. Chen, T. H. Stievater, E. T. Batteh, X. Li, D. G. Steel, D. Gammon, D. S. Katzer, D. Park, L. J. Sham, Biexciton quantum coherence in a single quantum dot, Phys. Rev. Lett. 88, 117901 (2002).
[57] X. Li, Y. Wu, D. Steel, D. Gammon, T. H. Stievater, D. S. Katzer, D. Park, C. Piermarocchi, L. J. Sham, An All-Optical Quantum Gate in a Semiconductor Quantum Dot, Science 301, 809 (2003).
[58] Y. Wu, X. Li, L. M. Duan, D. G. Steel, D. Gammon, Density Matrix Tomography through Sequential Coherent Optical Rotations of an Exciton Qubit in a Single Quantum Dot, Phys. Rev. Lett. 96, 087402 (2006).
[59] G. Dutt, PhD Thesis, University of Michigan, 2005.
[60] J. Cheng, PhD Thesis, University of Michigan, 2006.
[61] Y. Wu, PhD Thesis, University of Michigan, 2007.
[62] R. J. Warburton et al., Nature 405, 926 (2000).
[63] A. S. Bracker, E. A. Stinaff, D. Gammon, M. E. Ware, J. G. Tischler, A. Shabaev, Al. L. Efros, D. Park, D. Gershoni, V. L. Korenev, and I. A. Merkulov, Optical Pumping of the Electronic and Nuclear Spin of Single Charge-Tunable Quantum Dots, Phys. Rev. Lett. 94, 047402 (2005).

Chapter 3

Noise in Laser Spectroscopy

Laser spectroscopy experiments are carefully designed to measure specific optical signals despite the presence of fluctuating noise. The signals are physical observables with certain characteristics we are interested in, and the noise is the same physical variable changing in an undesired way. If there were no noise, laser spectroscopy would be much easier. Ideally, no matter how small the signal may be, we can always use amplifiers to boost signals up to a level detectable by instruments, assuming there is no noise. However, in practice the amplifier approach does not always work because amplifiers amplify both signals and noise in the same way and amplifiers bring extra noises into the measurement.

To be specific, noise, defined as random fluctuations in a particular measurement, is distinguished from signals, the measured quantities themselves, for experimental studies. Noise always exists in the experiments, for example, in the lasers, detectors, etc. Whether we can measure the signals of interest depends on the ratio between the signal and noise, the SNR (Signal to Noise Ratio). In some experiments, the signals are much bigger than the noise so that noise can be essentially ignored. In other experiments, where the signals are comparable or even weaker than the noise, measuring the weak signals could be challenging. It is important to study the properties of noise to develop experimental noise reduction techniques to improve the SNR for laser spectroscopy.

This chapter studies noise statistics, noise physics, and the actual noise seen in laser spectroscopy experiments. First, some statistical models for the noise are

introduced to lay down a mathematical foundation for the properties of noise. Then the physics of two kinds of fundamental noise, electrical thermal noise and laser shot noise, are discussed to understand the underlying principles. At the end of the chapter, the practical noise, seen in laser spectroscopy, from the light source, optical devices, detectors, and electrical signal processing, are discussed to illustrate how noise affects experiments.

3.1 Noise Statistics

Noise consists of nondeterministic random fluctuations which require statistical descriptions. Some simple description of the statistics will help in understanding the noise properties to be discussed later. In this section, first some statistical terms are defined for noise measurements. Then two statistical models, a random walk model and a rare event model, are discussed along with their respective statistical distributions.

3.1.1 Statistics for noise measurement

The properties of random variables can be described by a statistical distribution [1]. The statistical distribution gives the probability of the random variable taking a given value. Once the statistical distribution is known, important properties of a random variable X can be estimated. The mean and the variance are the two most important characteristics. The mean $\langle X \rangle$, defined as the average over a certain number of repeated measurements, gives the expected value of the random variable. For a discrete random variable where p_i is the probability for $X = x_i$,

$$\langle X \rangle = \sum_i p_i x_i \tag{3-1}$$

For a continuous random variable where $f(x)$ is the probability distribution function,

$$\langle X \rangle = \int_{-\infty}^{\infty} x f(x) dx \tag{3-2}$$

The variance $\langle \Delta X^2 \rangle$,

$$\langle \Delta X^2 \rangle = \left\langle \left(X - \langle X \rangle \right)^2 \right\rangle = \langle X^2 \rangle - \langle X \rangle^2 \tag{3-3}$$

is defined as the averaged square of the variation of the measured value from the mean, represents the amount of fluctuation of the random variable.

Experiments are designed to measure physical observables, for instance, voltage or current. Although experimentalists try to keep all parameters fixed as much as possible, repeated measurements yield different values due to uncontrollable changes in experimental parameters. Usually a large number of repeated measurements under the same conditions are taken to obtain reliable experimental results. In experiments the measured quantities are modeled as random variables with certain statistical distributions. Under the assumption that all noise and measurement errors are random and independent, experimental data will follow Gaussian distributions. The average represents the most probable value of the physical measurable, and the variance indicates the noise in the experiment.

Another statistical model is the binominal distribution. Binominal statistics is a simple model to describe the probability of the number of successes in a consecutive yes/no experiments with a fixed rate. Assume the rate for yes is *p* and the rate for no is $1-p$. After *n* trials the number of success could be any number from 0 to *n*. The probability of getting *k* success follows the binominal distribution.

$$f(k,n,p) = \frac{n!}{k!(n-k)!} p^k (1-p)^{n-k} \tag{3-4}$$

The binominal coefficient is defied as

$$\binom{n}{k} = \frac{n!}{k!(n-k)!} \tag{3-5}$$

This statistical distribution will be used in the next subsection to help describe more complicated models.

3.1.2 Random walk model

The random walk model [2] is a statistical model to describe the offset from an origin after successive steps of the same step size without preferred directions. There are three assumptions. First, the walk starts from the origin. Second, each step is the same size. Third, the probability of stepping into any direction is the same. The random walk model gives the average straight-line distance after N steps.

The simplest random walk is a one-dimensional random walk, which means the walk is confined in a line and there are only two possible directions. A simple derivation shows that the average straight-line distance is 0 and the variance is $\sqrt{N}$ times the step size.

Assume there are a total of N random steps of equal length l, and n_1 (n_2) is the respective number of steps in the positive (negative) direction. The straight-line distance L from the origin after N steps is

$$L = l(n_1 - n_2) = l(n_1 - (N - n_2)) = l(2n_1 - N) \tag{3-6}$$

The probability of getting n_1 positive steps is given by the binomial coefficient

$$P(n_1) = \binom{N}{n_1} \frac{1}{2^N} \tag{3-7}$$

The average and variance can be estimated as

$$\langle L \rangle = \sum_{n_1} LP(n_1) = \frac{l}{2^N} \sum_{n_1} (2n_1 - N) \binom{N}{n_1} \tag{3-8}$$

$$\langle L^2 \rangle = \sum_{n_1} L^2 P(n_1) = \frac{l^2}{2^N} \sum_{n_1} (2n_1 - N)^2 \binom{N}{n_1} \tag{3-9}$$

With the aid of the binomial theorem

$$(1+x)^n = \sum_{k=0}^{n} \binom{n}{k} x^k , \tag{3-10}$$

we get

$$\langle L \rangle = 0 \tag{3-11}$$

$$\langle L^2 \rangle = Nl^2 . \tag{3-12}$$

It shows the average distance is 0, as expected from the randomness about the origin, and the variance is $\sqrt{N}$, due to the independence of adjacent steps.

The random walk model is more complicated in two-dimensions and three-dimensions. There are many applications of the random walk model in physics and mathematics. The Brownian motion of particles suspended in liquid is an example of a three-dimensional random walk. We will show how it describes the thermal noise in a later section.

3.1.3 Rare events model with the Poisson distribution

Another statistical model related to noise is the rare event model, which describes the probability of a given number of independent events occurring in a certain time if the events have a known average occurrence rate. Many physical processes are repeated independent single events with fixed probabilities. We will use photon detection here as an example [3]. There are three assumptions. First, a single event has a certain probability and the probability of the event occuring is proportional to the length of the time interval.

$$P(1,t,t+\Delta t)=\lambda\Delta t \tag{3-13}$$

where λ is the probability coefficient, and Δt is the time interval.

Second, no multiple events occur simultaneously. The probability of getting more than one photon in the short time interval is zero.

$$P(n,t,t+\Delta t)=0 \text{ for } n\geq 2 \text{ and } P(0,t,t+\Delta t)=1-\lambda\Delta t \tag{3-14}$$

Third, the system has no memory. Photon detection occurring in any two non-overlapping time intervals is statistically independent.

The probability of getting k photons can only occur in two ways. One is getting k photons in the time interval $(t,t+\tau)$ and getting 0 photons in the time interval $(t+\tau,t+\tau+\Delta\tau)$. The other is getting k-1 photons in the time interval $(t,t+\tau)$ and getting 1 photon in the time interval $(t+\tau,t+\tau+\Delta\tau)$.

$$P(K;t,t+\tau+\Delta\tau)=P(k;t,t+\tau)[1-\lambda(t+\tau)\Delta\tau]+P(k-1;t,t+\tau)[\lambda(t+\tau)\Delta\tau] \tag{3-15}$$

Rearranging terms, we get

$$\frac{P(k;t,t+\tau+\Delta\tau)-P(k;t,t+\tau)}{\Delta\tau}=\lambda(t+\tau)[P(k-1;t,t+\tau)-P(k;t,t+\tau)] \quad (3\text{-}16)$$

Taking $\Delta\tau \to 0$,

$$\frac{dP(k;t,t+\tau)}{d\tau}=\lambda(t+\tau)[P(k-1;t,t+\tau)-P(k;t,t+\tau)] \quad (3\text{-}17)$$

The boundary condition is

$P(0;t,t)=1$.

Solving Equation (2-17) gives

$$P(k;t,t+\tau)=\frac{(\lambda\tau)^k}{k!}e^{-\lambda\tau} \quad . \quad (3\text{-}18)$$

Taking τ as the unit of time, we get the Poisson distribution.

$$P(k)=\frac{\lambda^k}{k!}e^{-\lambda} \quad (3\text{-}19)$$

The mean and the variance are

$$< k >= \int_0^\infty P(k)k = \lambda \quad (3\text{-}20)$$

$$\sigma_k^{\,2} \equiv < k^2 > - < k >^2 = \lambda \, . \quad (3\text{-}21)$$

The quantification factor for the fluctuation is λ. Since the quantity is independent of time, the same amount of fluctuation, λ, occurs at any frequency. Figure 3.1 gives the plot of the Poisson distribution.

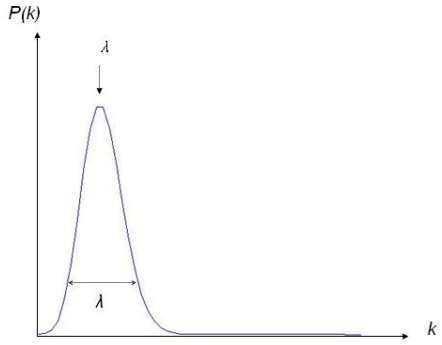

Figure 3.1 An example of a Poisson distribution (λ indicates the expected number of occurrence and the variance).

Another more intuitive way to understand the Poisson statistics is by studying the occurrence probabilities of rare events in the limit of an infinite number of trials. A rare event is an event that may or may not occur in a single trial. Assume the probability that an event occurs is p, which means the probability that the event does not occur is $1-p$. For n independent trials, the probability that the event occurs k times follows a Binominal distribution $f(k,n,p)$ as in Equation (2-4). Taking the limit as n goes to infinity, we get

$$\begin{aligned}&\lim_{n\to\infty}\frac{n!}{k!(n-k)!}p^k(1-p)^{n-k}=\lim_{n\to\infty}\frac{n!}{k!(n-k)!}(np)^k(1-\frac{np}{n})^{n-k}\\&=\lim_{n\to\infty}\left(\frac{n}{n}\right)\left(\frac{n-1}{n}\right)\left(\frac{n-2}{n}\right)\bullet\bullet\bullet\left(\frac{n-k+1}{n}\right)\frac{\lambda^k}{k!}\left(1-\frac{\lambda}{n}\right)^n\left(1-\frac{\lambda}{n}\right)^{-k}\end{aligned} \tag{3-22}$$

$$\text{Since } \lim_{n\to\infty}\left(1-\frac{\lambda}{n}\right)^n=e^{\lambda} \tag{3-23}$$

$$\lim_{n\to\infty}\frac{n!}{k!(n-k)!}p^k(1-p)^{n-k}=\frac{\lambda^k e^{-\lambda}}{k!} \tag{3-24}$$

Distributions with a standard deviation larger than n are called super-Poisson distributions, and distributions with a standard deviation smaller than n are called sub-Poisson distributions.

3.2 Noise physics

In laser spectroscopy all kinds of noise exist. Some noise is internal, coming from fundamental physical processes. Some noise is undesired fluctuation caused by the environment. This section focuses on the underlying physics of the properties of internal noise. Two types of fundamental noise are discussed here. One is electrical thermal noise due to thermal fluctuation of the electrons' motion, and the other is laser shot noise due to fluctuation of the quantized optical fields.

3.2.1 Electrical thermal noise

Electrical thermal noise, also called Johnson noise, giving rise to the fluctuation of electrical currents in electrical circuits, is ubiquitous for all electronics. At any temperature above 0K, the thermal motion of electrons in any

electronic component changes randomly due to collisions, which causes random fluctuations of the current. When measuring the current on a resistor in a closed circuit precisely, we will see this small thermal noise. Equivalently, the thermal noise can also be represented as voltage or power.

Johnson and Nyquist first studied electrical thermal noise from statistical and thermal physics [4, 5]. The intrinsic electrical thermal noise is independent of the size, current, or voltage on the resistor. It is notable that the amount of electrical thermal noise depends on $4k_BT$ only, which is related to the thermal energy causing the noise. At temperature T, electrons have random thermal motion of energy k_BT, which gives rise to fluctuations of the electron velocity. A simple picture is that at higher temperatures, electrons move faster, and the fluctuation of the electron speed increases. For a completely random fluctuation, the speed change can happen on any time scale with an equal probability, which gives a frequency-independent (white) noise spectrum.

Electrical thermal noise can be understood with a simple random walk model [6]. Assume the electrons in a circuit go through a one-dimensional random walk with a step size d due to the thermal motion at temperature T. According to the statistical properties we obtained in Section 3.1.2, after N steps, the average displacement $\langle x_N \rangle$ is 0, but the fluctuation $\langle x_N{}^2 \rangle$ is nonzero.

$$\langle x_N \rangle = \sum_1^N \langle d_i \rangle = 0 \tag{3-25}$$

$$\langle x_N{}^2 \rangle = \left\langle \left[\sum_1^N d_i \right]^2 \right\rangle = \sum_1^N d_i{}^2 = N\langle d^2 \rangle \tag{3-26}$$

The average step size d depends on the velocity of the thermal motion v, determined by the temperature T.

$$E = \frac{1}{2} m \langle v \rangle^2 = k_B T \tag{3-27}$$

$$\langle d \rangle^2 = \langle v\tau \rangle^2 = \langle v \rangle^2 \tau^2 = \frac{2k_BT}{m} \tau^2 \tag{3-28}$$

where v is the electron velocity, k_B is the Boltzmann constant, and m is the mass of electrons.

In a volume with an area A and a length L, the number of steps N during a time period t_0 can be estimated as:

$$N = \frac{nALt_0}{\tau} \tag{3-29}$$

where n is the electron density, and τ is the time between collisions.

The thermal noise current can be evaluated as

$$i = \frac{e\left(\left\langle x_N{}^2 \right\rangle\right)^{1/2}}{Lt_0} = \frac{e}{Lt_0}\left(N\left\langle d^2 \right\rangle\right)^{1/2} = \frac{e}{Lt_0}\left(\frac{nALt_0}{\tau}\frac{2k_BT}{m}\tau^2\right)^{1/2}. \tag{3-30}$$

The resistance R and the conductivity σ are

$$R = \frac{L}{\sigma A} \text{ and} \tag{3-31}$$

$$\sigma = ne\frac{e\tau}{2m}, \tag{3-32}$$

Taking $t_0 = 1\text{sec}$ to normalize the bandwidth to 1Hz, we thus get for the thermal noise current.

$$i = \left(\frac{4k_BT}{R}\right)^{1/2}. \tag{3-33}$$

It is shown that electrical thermal noise current depends on the temperature T and the resistance of the resistor R. The resistor, usually 50 ohms for impendence matching in radio frequency (RF) circuits, is to convert the thermal fluctuation into a current or voltage.

Electrical thermal noise is a form of white noise, i.e. it is independent of frequency. A simulation of thermal noise is illustrated in Figure 3.2 (a) and (b). Experimentally, the electrical thermal noise can be measured with an amplifier. Figure 3.2(c) shows the electrical thermal noise as the background noise floor of the measurement system when there is no input. This noise floor includes the thermal noise from the opto-electronics and the amplifier noise. The electrical thermal noise is responsible for most electronics noise commonly seen in

optoelectronics detectors, electrical circuits, amplifiers, and electrical instruments, which will be discussed in Section 3.3.

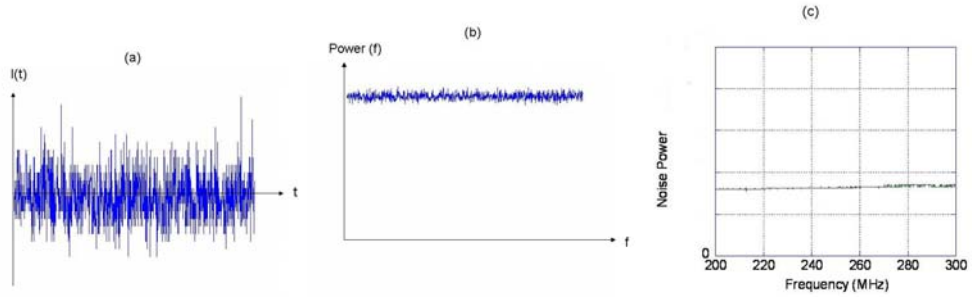

Figure 3.2 Electrical thermal noise in time and frequency domains (a) simulation of electrical thermal noise in the time domain (b) simulation of electrical thermal noise in the frequency domain (c) measured electrical thermal noise spectrum

There are a few ways to reduce the electrical thermal noise. One way is to reduce the temperature since the thermal noise power drops linearly with the temperature. Practically it is not hard to keep the detection electronics at low temperature, especially for cryogenic experiments. But the final stage of measurement always involves large-size commercial instruments, such as lock-in amplifiers or spectrum analyzers, which are usually specified for room temperature operation. Another method of reducing the electrical thermal noise is by using large resistance. This is also hard to implement since standard RF circuits use a 50 ohm impendence. Some experimental techniques can reduce the effects of thermal noise in measurement and they will be discussed in later chapters.

3.2.2 Laser shot noise

The fundamental optical noise is laser shot noise, which appears as the fluctuation of the laser intensity in repeated measurements, even for an ideal laser without any external noise caused by the environment. All lasers, as coherent light sources, are subjected to laser shot noise due to the quantum properties of light.

In classical physics, an ideal monochromatic coherent light is described as a continuous electromagnetic wave with well defined amplitude and phase, like a

classical particle having well defined momentum and position. However, in reality the optical amplitude and phase are not infinitely well defined, but always fluctuating with a small variance according to some statistical models. Usually a laser beam has a very large number of photons, for example, 10^{13} for a few μW, so that the small fluctuation can be ignored. However, in some precise measurements where the fluctuation becomes important, or in low light intensity measurements where the fluctuation is comparable with the light intensity, those fluctuations cannot be ignored, and quantum optics is necessary to study the quantum fluctuations shown in laser shot noise.

In this section, first a simple photon number model is introduced to illustrate the properties of laser shot noise. Then a quantum optics model is presented to explain the origin of laser shot noise and how different optical quantum states demonstrate laser shot noise.

3.2.2.1 A photon number laser shot noise model

A simple understanding of laser shot noise is based on the Poisson distribution of photon number as discussed in Section 3.1.3. The photon number fluctuation in a quantized coherent laser light source is a random process following the assumptions of the rare event model, due to the probabilistic nature of quantum mechanics. For a laser beam with an average number of photons N in a unit of time, the number of photons measured in repeated measurement follows a Poisson distribution.

Based on this model, two important properties of laser shot noise can be derived. First, laser shot noise, like electrical thermal noise, is white noise. Since the standard derivation of a Poisson distribution is $\sqrt{N}$ and the fluctuation is random over any time scale, the amount of the laser shot noise is $\sqrt{N}$ over any frequency. Second, the noise spectra of two laser beams with same power are completely independent. These properties will be the foundation for our work in measuring signal below the laser shot noise. Figure 3.3 illustrates laser shot noise in time and frequency domains, as fluctuations of electric field, fluctuation of laser intensity, and noise spectrum.

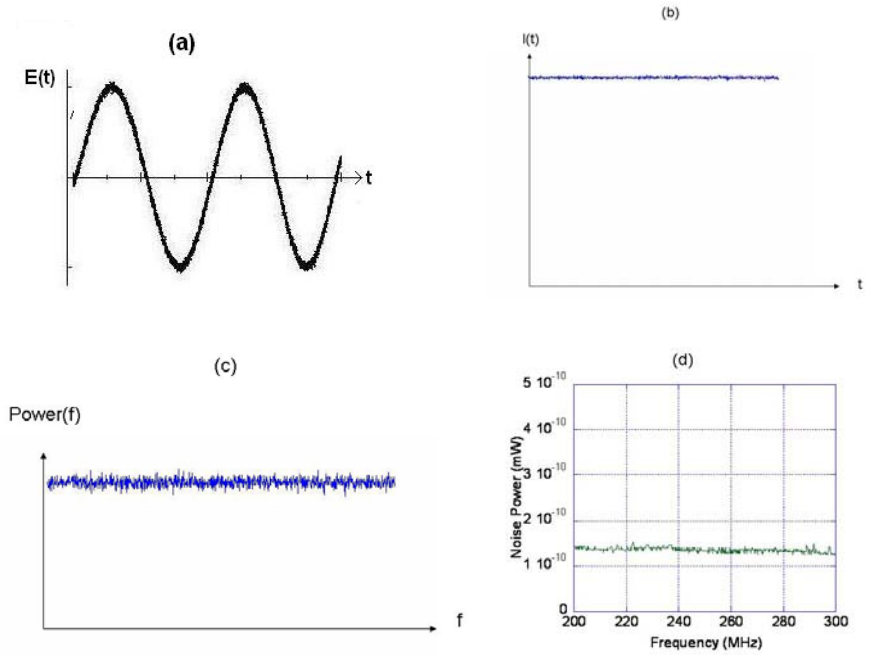

Figure 3.3 Laser shot noise in time and frequency domains (a) laser shot noise as E-field amplitude fluctuations in the time domain by simulation (b) laser shot noise as laser intensity fluctuations in the time domain by simulation (c) laser shot noise spectrum of the (b) obtained by Fourier Transform (d) laser shot noise spectrum measured with a Coherent 699 dye laser

Usually laser shot noise is very small compared with the average intensity so that it can be ignored in most laser spectroscopy experiments. Figure 3.4 gives the amount of laser shot noise and the corresponding ratio between the laser shot noise and the average intensity over the photon number and laser power. The inserts illustrate the electric field amplitude fluctuation caused by the laser shot noise with a normalized scale when photon number is small (<100). It is clear that at the laser power range used in most laser spectroscopy experiments, μW to mW, the laser shot noise can be ignored. However, laser shot noise becomes important for laser spectroscopy with small signals comparable to or even lower than the shot noise, which is the focus of this study.

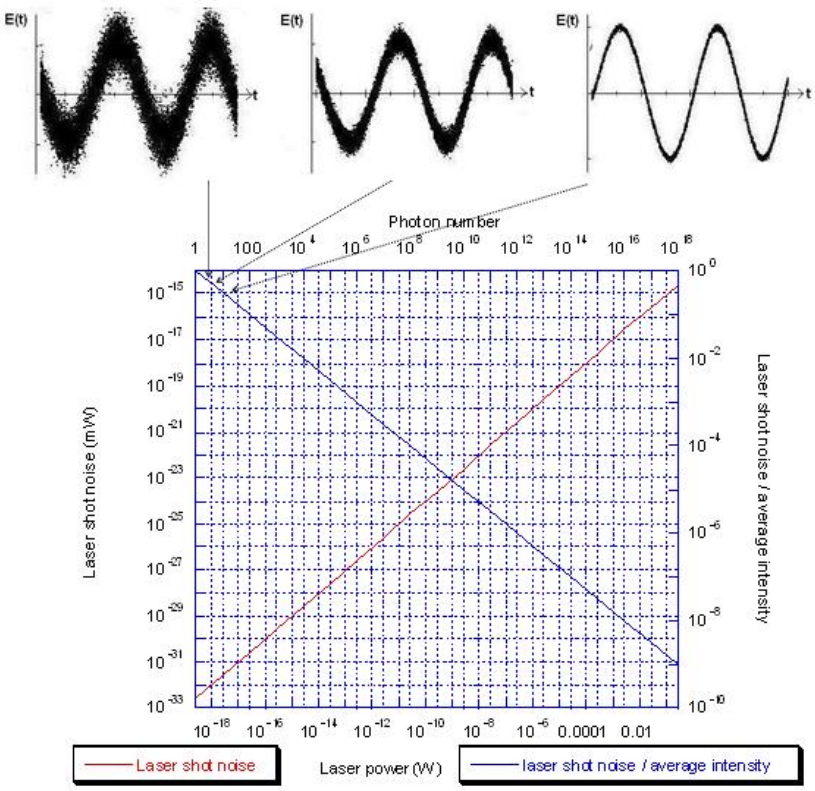

Figure 3.4 Laser shot noise and the optical signal detection capability at the SNL versus laser power or photon number [the inserts illustrate the electric field amplitude fluctuation caused by the laser shot noise with a normalized scale when the photon number is small (<100).]

The shot noise limit (SNL) refers to the experimental condition under which the dominant noise is the laser shot noise. In most laser spectroscopy experiments the largest noise is the laser common mode noise that goes up linearly with N, which means the SNR cannot be improved by increasing the laser power. At the SNL, the SNR can be improved by increasing laser power. The SNL is a desired condition that requires significant effort. Practically the SNL indicates the minimum optical signal we can measure if we know the laser power on the detector. The minimum detectable optical signal normalized to the laser power should be larger than the ratio between the laser shot noise and average intensity. Figure 3.4 shows the optical signal detection capability as the ratio between the laser shot noise and the average intensity depending on the laser power.

Since the photon number is proportional to the laser power, the square root dependence indicates that the laser shot noise is proportional to the square root of the laser power. Since in the usual case signals and most noise in experiments are proportional to the laser power, the square root dependence provides two different strategies of optimizing the SNR in experiments. On the one hand, if the experiment is limited by common mode noise, which proportional to the laser power, the SNR is optimized by reducing the laser power, since the common noise drops faster than the laser shot noise. We can always reach the shot noise limit by attenuating the laser power, even though practically we may be limited by the sensitivity of our detectors. On the other hand, if the experiment is in the shot noise limit, the SNR is optimized by increasing the laser power. In this case the practical limits would be the available laser power or detector damage threshold.

To measure signals smaller than the laser shot noise, specific experimental techniques are required to reduce the effects of noise, which will be discussed in following chapters. It is worthy to note that some experiments may go below the shot noise limit by using a current with sub-Poisson distributions in laser diodes [7, 8, 9].

3.2.2.2 A quantum optics laser shot noise model

Besides the simple pictorial description of shot noise as the fluctuation of photon number caused by rare events, shot noise can be described as fluctuations of the intensity of the electrical field through the quantization of light.

In this section, first a quantum harmonic oscillator model is introduced to define quantum amplitude and phase. Then three different quantum states: number states, coherent states, and squeezed states, are discussed to show the interplay between quantum amplitude and phase fluctuations that gives rise to laser shot noise. Most of the discussion here is adapted from Reference [10].

A Quantum Harmonic Oscillator Model for the Quantization of Light

A quantum harmonic oscillator can model the quantization of light. For a harmonic oscillator, the Hamiltonian is

$$\hat{H} = \frac{\hat{p}}{2m} + \frac{1}{2} m\omega^2 \hat{q}^2 \tag{3-34}$$

where $\hat{q}$ is the position operator and $\hat{p}$ is the momentum operator. $\hat{p}$ and $\hat{q}$ obey the commutation relation.

$$\left[\hat{q}, \hat{p}\right] = i\hbar \tag{3-35}$$

A pair of dimensionless operators, a destruction operator $\hat{a}$ and a creation operator $\hat{a}^\dagger$, are defined as the following.

$$\hat{a} = \sqrt{2m\hbar\omega}(m\omega\hat{q} + i\hat{p}) \tag{3-36}$$

$$\hat{a}^\dagger = \sqrt{2m\hbar\omega}(m\omega\hat{q} - i\hat{p}) \tag{3-37}$$

The commutation relation is

$$\left[\hat{a}, \hat{a}^\dagger\right] = \hat{a}\hat{a}^\dagger - \hat{a}^\dagger\hat{a} = 1 \tag{3-38}$$

The Hamiltonian can be rewritten as

$$\hat{H} = \frac{1}{2}\hbar\omega(\hat{a}\hat{a}^\dagger + \hat{a}^\dagger\hat{a}) = \hbar\omega(\hat{a}^\dagger\hat{a} + \frac{1}{2}) \tag{3-39}$$

Let $\left|n\right\rangle$ be an energy eigenstate with eigenvalue E_n. The eigenvalue equation is

$$\hat{H}\left|n\right\rangle = \hbar\omega(\hat{a}^\dagger\hat{a} + \frac{1}{2})\left|n\right\rangle = E_n\left|n\right\rangle \tag{3-40}$$

Solving the equation we get

$$\hat{a}\left|n\right\rangle = \sqrt{n}\left|n-1\right\rangle \tag{3-41}$$

$$\hat{a}^\dagger\left|n\right\rangle = \sqrt{n+1}\left|n+1\right\rangle \tag{3-42}$$

$$\left|n\right\rangle = \frac{(\hat{a}^\dagger)^n}{\sqrt{n!}}\left|0\right\rangle \tag{3-43}$$

$$E_n = (n + \frac{1}{2})\hbar\omega\,,\ n = 0,1,2,... \tag{3-44}$$

where $\left|0\right\rangle$ is the ground state, and the ground state energy is $\frac{1}{2}\hbar\omega$ rather than 0. It shows that the vacuum field has a nonzero energy, a statement that does not appear in the classical theory. Later discussion will show that the vacuum field also gives rise to noise due to the fluctuation caused by the nonzero energy.

The number operator $\hat{n}$, which corresponds to the number of photons in a quantum state, is defined as

$$\hat{n} = \hat{a}^{\dagger}\hat{a} \tag{3-45}$$

And it gives

$$\hat{n}|n\rangle = n|n\rangle \tag{3-46}$$

Quantization of the electromagnetic field yields an E-field operator of the form

$$\hat{E}(\chi) = \hat{E}^{+}(\chi) + \hat{E}^{-}(\chi) = (\hbar\omega / 2\varepsilon_0 V)^{1/2}(\hat{a}e^{i\chi} + \hat{a}^{\dagger}e^{-i\chi}) \tag{3-47}$$

where

$$\chi = \omega t - kz - \frac{\pi}{2} \tag{3-48}$$

Defining a pair of quadrature operators $\hat{X}$ and $\hat{Y}$ as

$$\hat{X} = (\hat{a} + \hat{a}^{\dagger}) / \sqrt{2} \tag{3-49}$$

$$\hat{Y} = (\hat{a} - \hat{a}^{\dagger}) / \sqrt{2}i \tag{3-50}$$

and with the commutation relation

$$\left[\hat{X}, \hat{Y}\right] = i\hbar, \tag{3-51}$$

we get a dimensionless form of the Heisenberg uncertainty relation

$$(\Delta X)^2 (\Delta Y)^2 \geq \frac{1}{16} \tag{3-52}$$

Using the quadrature operators, with units of $(\hbar\omega / 2\varepsilon_0 V)^{1/2}$ the E field operator can be written as

$$\hat{E}(\chi) = \hat{E}^{+}(\chi) + \hat{E}^{-}(\chi) = \frac{1}{2}(\hat{a}e^{i\chi} + \hat{a}^{\dagger}e^{-i\chi}) = \hat{X}\cos\chi + \hat{Y}\sin\chi \tag{3-53}$$

To evaluate the effects on measuring signals vs. noise, a few parameters are defined here for evaluating the SNR for different states. The coherent signal S is defined as the expectation value of the field operator. The inherent noise is defined as the variance of the electrical field, showing the fluctuation of the field. The SNR is defined as the signal power over the noise power.

$$S = \langle E(\chi) \rangle \tag{3-54}$$

$$N = \left(\Delta E(\chi)\right)^2 \tag{3-55}$$

$$SNR = \frac{S^2}{N} = \frac{\left\langle E(\chi)\right\rangle^2}{\left(\Delta E(\chi)\right)^2} \tag{3-56}$$

By looking into the photon number fluctuation and SNR for the number states, coherent states, and squeezed states, we can compare the noise properties of the different states.

Number State

Quantization of light with a harmonic oscillator model shows that the photon number states form a complete set for a single mode state. Number states, also called Fock states, are the energy eigenstates of the harmonic oscillator discussed in the previous section. Applying the number operator, we get

$$\left\langle n\middle|\hat{n}\middle|n\right\rangle = \left\langle n\middle|\hat{a}^{\dagger}\hat{a}\middle|n\right\rangle = n \tag{3-57}$$

$$\left\langle n\middle|\hat{n}^2\middle|n\right\rangle = \left\langle n\middle|\hat{n}n\middle|n\right\rangle = n^2 \tag{3-58}$$

$$(\Delta n)^2 = 0 \tag{3-59}$$

There is no photon number fluctuation for the number states according to the definition of a number state.

Using the quadrature operators defined earlier, the average and the variance of the operators can be estimated.

$$(\hat{X}^2 + \hat{Y}^2)\left|n\right\rangle = (n + \frac{1}{2})\left|n\right\rangle \tag{3-60}$$

$$\hat{X}^2\left|n\right\rangle = \frac{1}{2}(n + \frac{1}{2})\left|n\right\rangle \tag{3-61}$$

$$\hat{Y}^2\left|n\right\rangle = \frac{1}{2}(n + \frac{1}{2})\left|n\right\rangle \tag{3-62}$$

$$\left\langle n\middle|\hat{X}\middle|n\right\rangle = \left\langle n\middle|\hat{Y}\middle|n\right\rangle = 0 \tag{3-63}$$

$$(\Delta X)^2 = (\Delta Y)^2 = \frac{1}{2}(n + \frac{1}{2}) \tag{3-64}$$

The average field measured by any detector is zero and the intensity fluctuation is nonzero.

$$S = \langle n | \hat{E}(\chi) | n \rangle = 0 \tag{3-65}$$

$$N = (\Delta E(\chi)^2) = \langle n | \hat{E}(\chi)^2 | n \rangle - \langle E(\chi) \rangle^2 = \frac{1}{2}(n + \frac{1}{2}) \tag{3-66}$$

$$SNR = 0 \tag{3-67}$$

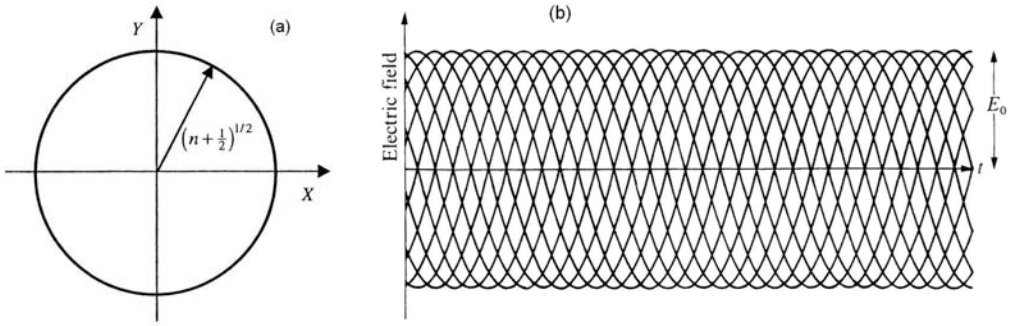

Figure 3.5 A number state (a) illustrated with the quadrature operators (b) illustrated with the amplitude-phase picture (the sin waves with different phases represents the phase is random.) (Figure courtesy of Loudon [10])

Figure 3.5(a) illustrates the electric field of a number state as an arrow with the uncertainty of the quadrature operators, which gives a circle according to Equation 3-60. The average of the field is zero, shown by the position of the center of the circle at the origin.

It is clear that amplitude of the number state is well defined without uncertainty, shown by the constant length of the arrow no matter where it is on the circle. However, the phase, represented by the angle from the real field axis, could be anywhere, which means the phase is undefined with infinite uncertainty. The amplitude-phase picture of number states is illustrated in Figure 3.5(b).

Even though number states show zero amplitude fluctuation, they are not helpful in reducing experimental noise. The number states are theoretical states, and it is very hard to generate them in experiments.

Coherent State

A coherent state is a linear superposition of the number states defined as

$$|\alpha\rangle = \exp(-\frac{1}{2}|\alpha|^2)\sum_{n=0}^{\infty}\frac{\alpha^n}{(n!)^{1/2}}|n\rangle . \tag{3-68}$$

The coherent states are eigenstates of the destruction operator $\hat{a}$, where

$$\hat{a}|\alpha\rangle = \exp(-\frac{1}{2}|\alpha|^2)\sum_{n=0}^{\infty}\frac{\alpha^n}{(n!)^{1/2}}|n-1\rangle = \alpha|\alpha\rangle \text{ and} \tag{3-69}$$

$$\alpha = |\alpha|e^{i\theta} . \tag{3-70}$$

The photon number fluctuation gives the laser shot noise as the square root of the photon number, just as the statistical model shows, where

$$\langle\alpha|\hat{n}|\alpha\rangle = \langle\alpha|\hat{a}^{\dagger}\hat{a}|\alpha\rangle = |\alpha|^2 \tag{3-71}$$

$$\langle\alpha|\hat{n}^2|\alpha\rangle = \langle\alpha|\hat{a}^{\dagger}\hat{a}\hat{a}^{\dagger}\hat{a}|\alpha\rangle = |\alpha|^4 + |\alpha|^2 \tag{3-72}$$

$$(\Delta n)^2 = |\alpha|^2 = \langle n\rangle . \tag{3-73}$$

The average and variance of the quadrature operators are

$$\langle\alpha|\hat{X}|\alpha\rangle = \frac{1}{2}\langle\alpha|\hat{a}^{\dagger} + \hat{a}|\alpha\rangle = \frac{1}{2}(\alpha^* + \alpha) = |\alpha|\cos\theta \tag{3-74}$$

$$\langle\alpha|\hat{Y}|\alpha\rangle = |\alpha|\sin\theta \tag{3-75}$$

$$\langle\alpha|\hat{X}^2|\alpha\rangle = \frac{1}{4}\langle\alpha|\hat{a}^{\dagger}\hat{a}^{\dagger} + 2\hat{a}^{\dagger}\hat{a} + \hat{a}\hat{a} + 1|\alpha\rangle = |\alpha|^2\cos^2\theta + \frac{1}{4} \tag{3-76}$$

$$\langle\alpha|\hat{Y}^2|\alpha\rangle = \frac{1}{4}\langle\alpha|-\hat{a}^{\dagger}\hat{a}^{\dagger} + 2\hat{a}^{\dagger}\hat{a} - \hat{a}\hat{a} + 1|\alpha\rangle = |\alpha|^2\sin^2\theta + \frac{1}{4} \tag{3-77}$$

$$(\Delta X)^2 = (\Delta Y)^2 = \frac{1}{4} \tag{3-78}$$

This shows that coherent states have equal minimum uncertainty for both quadrature operators. Using the definition in Section 3.2.2.2, we can calculate the SNR for coherent states.

$$S = \langle\alpha|\hat{E}(\chi)|\alpha\rangle = |\alpha|\cos(\chi - \theta) \tag{3-79}$$

$$N = (\Delta E(\chi)^2) = \frac{1}{4} \tag{3-80}$$

$$SNR = 4|\alpha|^2\cos^2(\chi - \theta) = 4\langle n\rangle\cos^2(\chi - \theta) \tag{3-81}$$

Figure 3.6(a) illustrates the phase dependence of the electric field according to Equation (3-79). The solid line represents the sinusoidal curve of the mean E-field and the dashed lines represent the fluctuation of the field. This shows that coherent states have equal uncertainty for any given phase, giving the closest analogue to the classical EM field with minimum uncertainty in both amplitude and phase. Therefore coherent states are the best quantum states to represent a coherent single laser mode [11].

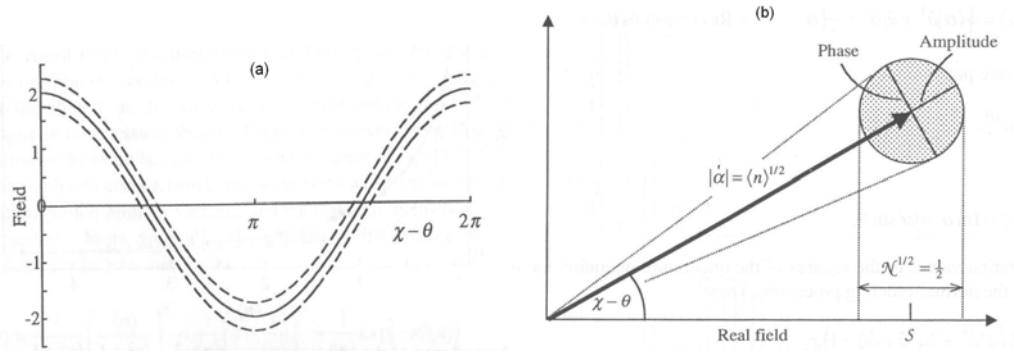

Figure3.6 A coherent state (a) phase dependence of the electrical field (b) quadrature representation (Figure courtesy of Loudon [10])

The uncertainty of the photon number and phase can be illustrated with a quadrature representation, as shown in Figure 2.6(b). The mean amplitude is represented by the arrow of length $|\alpha| = \langle n \rangle^{1/2}$ at the angle $\chi - \theta$. The circular disk of diameter ½ represent the field uncertainty according to the variance of the quadrature operators.

The amplitude uncertainty is estimated by the variance of the amplitude mean, and the phase uncertainty is represented by the angle corresponding to the variance of the phase operator:

$$\Delta n = \left(\langle n \rangle^{1/2} + \frac{1}{4} \right)^2 - \left(\langle n \rangle^{1/2} - \frac{1}{4} \right)^2 = \langle n \rangle^{1/2} \tag{3-82}$$

$$\Delta \varphi = \frac{1/2}{|\alpha|} = \frac{1}{2\langle n \rangle^{1/2}} . \tag{3-83}$$

The uncertainty relation is $\Delta n \Delta\varphi = \frac{1}{2}$. (3-84)

Since

$$|\alpha\rangle = \exp(-\frac{1}{2}|\alpha|^2)\sum_{n=0}^{\infty}\frac{\alpha^n}{(n!)^{1/2}}|n\rangle = \exp(-\frac{1}{2}|\alpha|^2)\sum_{n=0}^{\infty}\frac{(\alpha\hat{a}^\dagger)^n}{n!}|0\rangle = \exp(\alpha\hat{a}^\dagger - \frac{1}{2}|\alpha|^2)|0\rangle$$

(3-85)

it will be convenient to define a coherent-state displacement operator

$$\hat{D}(\alpha) = \exp(\alpha\hat{a}^\dagger - \alpha^*\hat{a}). \quad (3\text{-}86)$$

Squeezed states

Squeezed states are quantum states with reduced noise lower than the SNL in amplitude or phase. This is accomplished by shifting the uncertainty from one parameter space to another. Here, a squeezed coherent state is discussed for illustration.

A single mode quadrature squeezed coherent state is defined as

$$|\alpha,\zeta\rangle = \hat{D}(\alpha)\hat{S}(\alpha)|0\rangle \quad (3\text{-}87)$$

where $\hat{D}(\alpha)$ is the coherent state displacement operator defined in Equation 3-86, and $\hat{S}(\alpha)$ is the squeeze operator

$$\hat{S}(\zeta) = \exp(\frac{1}{2}\zeta^*\hat{a}^2 - \frac{1}{2}\zeta(\hat{a}^\dagger)^2) \quad (3\text{-}88)$$

ζ is the complex squeeze parameter with amplitude and phase defined as

$$\zeta = se^{i\vartheta} \quad (3\text{-}89)$$

Applying these operators we get

$$\hat{S}^\dagger(\zeta)\hat{D}^\dagger(\alpha)\hat{a}\hat{D}(\alpha)\hat{S}(\zeta) = \hat{a}\cosh s - \hat{a}^\dagger e^{i\vartheta}\sinh s + \alpha \quad (3\text{-}90)$$

$$\hat{S}^\dagger(\zeta)\hat{D}^\dagger(\alpha)\hat{a}^\dagger\hat{D}(\alpha)\hat{S}(\zeta) = \hat{a}^\dagger\cosh s - \hat{a}e^{-i\vartheta}\sinh s + \alpha^* \quad (3\text{-}91)$$

$$(\hat{a}\cosh s + \hat{a}^\dagger e^{-i\vartheta}\sinh s)\langle\alpha,\zeta| = (\hat{a}\cosh s + \hat{a}^* e^{-i\vartheta}\sinh s)\langle\alpha,\zeta| \quad (3\text{-}92)$$

The photon number fluctuation can be estimated as

$$\langle\alpha,\zeta|\hat{n}|\alpha,\zeta\rangle = |\alpha|^2 + \sinh^2 s \quad (3\text{-}93)$$

$$(\Delta n)^2 = \alpha^2 \left\{ e^{2s} \sin^2(\theta - \frac{1}{2}\vartheta) + e^{-2s} \cos^2(\theta - \frac{1}{2}\vartheta) \right\} + 2\sinh^2 s(\sinh^2 s + 1) \quad (3\text{-}94)$$

Similarly, the SNR can be evaluated.

$$\langle \alpha, \zeta | \hat{X} | \alpha, \zeta \rangle = \mathrm{Re}\,\alpha = |\alpha| \cos\theta \quad (3\text{-}95)$$

$$\langle \alpha, \zeta | \hat{Y} | \alpha, \zeta \rangle = \mathrm{Im}\,\alpha = |\alpha| \sin\theta \quad (3\text{-}96)$$

$$(\Delta X)^2 = \frac{1}{4} \left\{ e^{2s} \sin^2(\frac{1}{2}\vartheta) + e^{-2s} \cos^2(\frac{1}{2}\vartheta) \right\} \quad (3\text{-}97)$$

$$(\Delta Y)^2 = \frac{1}{4} \left\{ e^{2s} \cos^2(\frac{1}{2}\vartheta) + e^{-2s} \sin^2(\frac{1}{2}\vartheta) \right\} \quad (3\text{-}98)$$

$$S = \langle \alpha | \hat{E}(\chi) | \alpha \rangle = |\alpha| \cos(\chi - \theta) \quad (3\text{-}99)$$

$$N = (\Delta E(\chi)^2) = \frac{1}{4} \left\{ e^{2s} \sin^2(\chi - \frac{1}{2}\vartheta) + e^{-2s} \cos^2(\chi - \frac{1}{2}\vartheta) \right\} \quad (3\text{-}100)$$

$$SNR = \frac{4|\alpha|^2 \cos^2(\chi - \theta)}{e^{2s} \sin^2(\chi - \frac{1}{2}\vartheta) + e^{-2s} \cos^2(\chi - \frac{1}{2}\vartheta)} \quad (3\text{-}101)$$

$$SNR_{\max} = 4e^{2s} |\alpha|^2 \text{ for } \chi = \theta = \frac{1}{2}\vartheta \quad (3\text{-}102)$$

The phase dependence of the field amplitude is shown in Figure 3.7(a). The noise reduction at phase values of 0, π and 2π are achieved at the expense of increased noise at phase values of $\frac{\pi}{2}$ and $\frac{3\pi}{2}$.

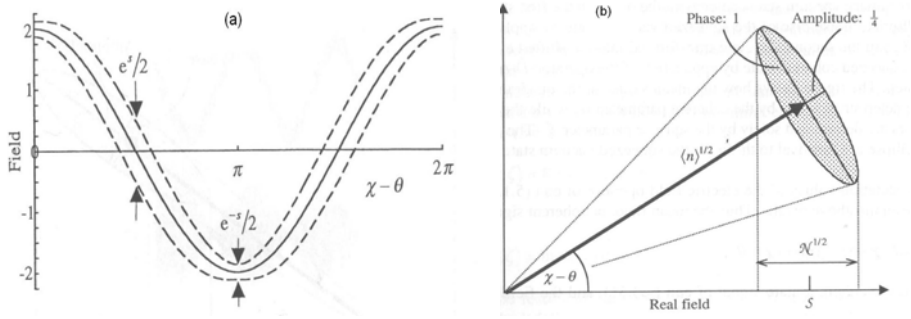

Figure 3.7 A squeezed state (a) phase dependence of the electrical field (b) quadrature representation (Figure courtesy of Loudon [10])

Figure 3.7(b) is the representation of an amplitude squeezed state with $\exp(s) = 2$ using the same notation as Figure 3.6(b). In the same way the photon number and phase uncertainty can be estimated as

$$\Delta n = \left(\langle n \rangle^{1/2} + \frac{1}{4} e^{-s} \right)^2 - \left(\langle n \rangle^{1/2} - \frac{1}{4} e^{-s} \right)^2 = \langle n \rangle^{1/2} e^{-s} \tag{3-103}$$

$$\Delta \varphi = \frac{e^{-s}}{2|\alpha|} = \frac{e^{-s}}{2\langle n \rangle^{1/2}} \tag{3-104}$$

The uncertainty relation remains same as $\Delta n \Delta \varphi = \frac{1}{2}$.

Experiments have been done to measure the phase dependence of squeezed states [12], as shown in Figure 3.8. The experimental results agree well with the theoretical plots in Figure 3.6(a) and 3.7(a).

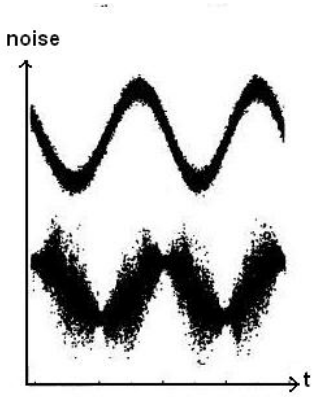

Figure3.8 Experimental measurement of coherent states and amplitude squeezed states (Figure courtesy of Breitenbach et. al. [12])

Squeezed states have been generated and measured with about 8dB below the SNL by using either parametric amplification with nonlinear optical crystals [13, 14] or sub-Poisson photon generation with semiconductor diode lasers [7-9]. Both techniques require complicated and precisely controlled systems. Even the best performance is limited to a few dB. All these limit the practical implementation of using squeezed states to measure weak signals below the SNL. One proposed application of squeezed light is to detect gravitational waves [15], which is still under design.

3.3 Practical noise in laser spectroscopy

Laser spectroscopy uses lasers as the light source, optical components to control light, and various photodetectors to convert optical signals into electrical signals. All these parts may bring noise into laser spectroscopy experiments.

In this section, the actual noise seen in laser spectroscopy from every step is analyzed. First, the optical noise caused by the optical source and components is discussed. Then the electrical noise from photodetection and electrical signal processing is studied. At the end, the total noise in the system is examined.

3.3.1 Optical noise

Optical noise is the noise from the optical components at the experimental setup. In laser spectroscopy, light is generated by lasers that generate coherent optical radiation with a certain frequency, linewidth, and intensity either as a continuous wave (CW) or a repetitive pulse train. Most often light is controlled by optical components or devices through intensity, phase, polarization, and wavelength. Optical noise can be divided into laser noise and propagation noise.

In the previous discussion, we learned that an ideal laser can generate radiation in coherent states at SNL, or squeezed states with sub-Poisson distributions. Actual lasers used in laser spectroscopy are dominated by technical noise due to practical limitations including spontaneous emission, mode hopping and competition, pumping power fluctuation, laser cavity drifting, temperature fluctuation, etc. To reduce laser noise it is preferable to stabilize the environment (including temperature, pumping source, and laser cavity) and have the laser run at a single longitudinal fundamental mode of minimum linewidth. One practical guide is the Schwalow-Townes limit [16], which gives the limited linewidth caused by spontaneous emission.

The amount of noise in different lasers varies over a large range due to the different configurations present. Technical noise of a laser can be characterized and reduced with experimental techniques to be discussed later. Figure 2-9(a) gives the overall noise of a CW dye laser. Figure 2-9(b) shows a comparison of

the ratio between the laser noise and average power from 10Hz to 100KHz, the frequency range for our lock-in amplifiers, of a dye laser and a diode laser. The diode laser is about two orders better than the dye laser. The dye laser approaches the SNL only at frequency above a few MHz, and the diode laser approaches the SNL at frequency above hundreds of Hz.

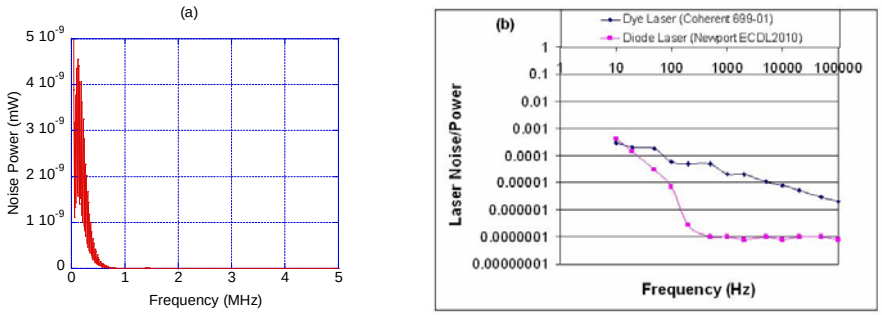

Figure 3.9 Laser noise (a) Laser noise of a CW dye laser (b) the ratio between the laser noise and average power of a dye laser and a diode laser

Practically laser noise can be divided into two categories. One is laser shot noise caused by quantization of field which can not be divided into two identical halve, as we discussed earlier. The other is common mode laser noise caused by the changing environment, which can be divided into two identical halves and be cancelled out with some experimental techniques to be discussed later. Usually the laser noise is the sum of the laser shot noise and common mode laser noise, with the former dominating at high frequency and the later dominating at low frequency.

All the noise discussed above is the static noise when a laser is running under a stable condition without any internal modulation. In many experiments the laser may need by internally modulated or scanned in frequency (or wavelength), amplitude, or phase by changing the laser cavity or gain medium. All these internal modulation or scanning causes significant noise much bigger than the static noise we have discussed. For our spectroscopy study on QDs, we needed to scan the laser over a wavelength range to study the absorption spectrum. The laser scanning noise dominates over other noise. Some experimental technique will be discussed in Chapter 5 to avoid the laser scanning noise.

In laser spectroscopy, laser light goes through optical components and experimental apparatuses before the optical signals are converted into electrical signals. Any mechanical vibration of the optical components or the experimental apparatuses gives mechanical noise in the measurements. Usually mechanical vibration for optical components is not an issue since most optics have properly designed mounts, and the mounts are tighten down on optical tables to minimize any mechanical vibration. Mechanical noise becomes important for experiments where the laser beam propagates through small apertures or suspended samples. For example, in our experiments on semiconductors, samples are mounted on a sample holder suspended in a cryostat, and the laser beam is focused down to a few microns to pass through submicron sized apertures. Mechanical noise needs be avoided for single dot study through the apertures.

Another noise source from beam propagation is the back reflection from optical surfaces and multiple reflections caused by undesired etalon effects. For any uncoated optical surface there is a 4% reflection. Usually the back reflected beams are ignored in experiments. In experiments with laser diodes, the back reflection could cause instability of the laser diode. Optical isolators can be used to reduce the back reflection into the laser diode. Multiple reflections caused by etalon effects could give artificial signals on detectors, which usually appear as interference patterns. The artificial effects can be removed by rotating the optics that are causing the etalon effects by a small angle.

3.3.2 Electrical noise

Electrical noise is the noise related to electronics or optoelectronics. In laser spectroscopy optical signals are converted into electrical signals by photo detectors and processed by electronics. Electrical noise consists of photodetection noise and signal processing noise.

In laser spectroscopy, optical signals are usually converted into electrical signals for convenient processing. Ideal opto-electrical conversion should not bring in noise. Actual opto-electrics devices always bring in extra noise due to

device properties [17]. Here the noise of two commonly used photo detectors: photodiodes and avalanch photodiodes (APD) are discussed.

Photodiodes are the most commonly used phtodetectors that convert light into electrical current. The noise of the photodiode consists of two sources [18]. One is the thermal noise caused by the resistance of the photodiode. The other is the dark current noise. The dark current indicates the amount of current coming out of the photodiode when there is no light. For a good photodiode and large enough signals, the dark current (nA) can be ignored compared with the photo current (μA or mA).

The avalanch photodiode is a photodiode with gain to amplify signals more than noise [18]. In addition to all the characteristics of the photodiode, APDs have one more characteristic, the gain. With a gain factor, the APD amplifies the current generated from the photodiode without the thermal noise, which gives better SNR than using a photodiode and electrical amplifiers. Usually, APDs are used for low light intensity detection rather than high light intensity since the APD has a low saturation threshold with gain. The extra noise caused by the APD can be represented by the excess noise factor, which is small compared to other noise sources for a good APD. Further details can be found in Reference [18].

Electrical signals converted from optical signals may go through electrical signal processing involving amplifiers, filters, and digitizers. Most electrical processing noise is from amplifiers and digitizers.

Since Johnson noise exists in any circuit, any electrical amplifier amplifies Johnson noise when it amplifies signals [19]. The quality of an amplifier is characterized by the Noise Factor or the Noise Figure (NF) defined as 10log(Noise Factor) dB, which tells how much excess noise the amplifier causes in the amplification. An ideal amplifier has a Noise Factor of 1 (NF 0dB). Low noise amplifiers may have Noise Factor of 2 (NF 3dB), which only doubles the noise power after amplification.

Now most signal processing is done digitally. Due to the rounding procedure in any A/D conversion, there is always a small amount of A/D conversion noise depending on the number of bits in the A/D converter. It is one over the maximum

integer represented by the A/D converter. For an 8-bit A/D converter, the error is $\pm\frac{1}{256}$. For a state-of-the-art 14-bit A/D converter, it is $\pm\frac{1}{48896}$, which usually can be ignored.

3.3.3 Total noise

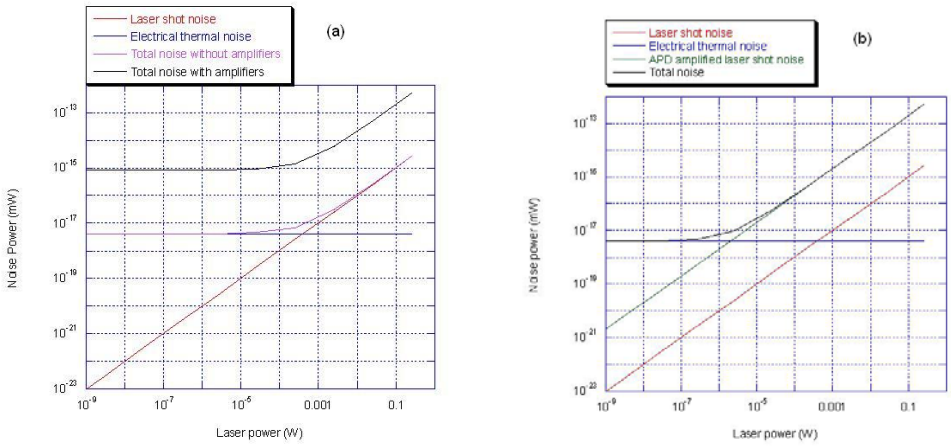

Figure 3.10 Total noise (a) Laser power dependence of the individual and total noise for a photodiode with a 20dB gain and 3dB NF amplifier (b) Laser power dependence of the individual and total noise for an APD with 20dB gain and 3dB NF

The total noise in laser spectroscopy measurements will be the incoherent superposition of the noise power from each source. At the shot noise limit, the total noise will be the sum of the laser shot noise and the electrical thermal noise, amplified by amplifiers. Figure 3.10 gives the laser power dependence of laser shot noise, electrical thermal noise, and total noise for a photodiode with amplifiers and an APD without amplifiers, assuming the amplifiers and the APD have the same 20dB gain and 3dB NF. It shows that in the low laser power regime electrical thermal noise dominates, and in the high laser power regime laser shot noise takes over. For the photodiode with amplifiers, the amplifier amplifies both laser shot noise and electrical thermal noise by 100 times in power, and introduces extra noise by a factor of two. The minimum laser power required to detect laser shot noise due to the existence of thermal noise is about 1mW. The APD only

amplifies the laser shot noise with extra noise, and the thermal noise is not amplified. The minimum laser power required to detect the laser shot noise drops down to about 10μW, which shows the advantage of APDs for low light intensity.

In summary, noise in laser spectroscopy was studied including noise statistics, noise physics of two fundamental noise sources, and actual noise from each component used in laser spectroscopy. The noise statistics section provided a mathematical model to study the properties of noise. The noise physics section explained the electrical thermal noise with statistical physics and the laser shot noise with quantum optics. The actual noise section illustrated the specific sources of noise from lasers, photo detectors, and amplifiers, and the total noise types. Based on an understanding of all these noise sources, experimental techniques to reduce the effects of noise in laser spectroscopy measurements will be discussed in the following chapters.

Bibliography

[1] G. Box, J. Hunter, W. Hunter, Statistics for Experimenters: An Introduction to Design, Data Analysis, and Model Building, Wiley-Interscience, 1978.
[2] M. Weissbluth, Photon-Atom interactions, Academic Press, 1989.
[3] J. Goodman, Statistical optics, John Wiley & Sons, 2000.
[4] J. Johnson, Thermal Agitation of Electricity in Conductors, Phys. Rev. 32, 97 (1928).
[5] H. Nyquist, Thermal Agitation of Electric Charge in Conductors, Phys. Rev. 32, 110 (1928).
[6] R. Henry, Random-Walk Model of Thermal Noise for Students in Elementary Physics, Jour. Amer. Phys. 41, 1361 (1973).
[7] W. H. Richardson, S. Machida, and Y. Yamamoto, Squeezed photon-number noise and sub-Poissonian electrical partition noise in a semiconductor laser, Phys. Rev. Lett. 66, 2867 (1991).
[8] H. Wang, M. Freeman, D. Steel, Squeezed light from injection-locked quantum well lasers, Phys. Rev. Lett. 71, 3951 (1993).
[9] Y. Li, D. Guzun, M. Xiao, Sub-shot-noise-limited optical heterodyne detection using an amplitude-squeezed local oscillator, Phys. Rev. Lett. 82 5225 (1999).
[10] R. Loudon, The quantum theory of light, Oxford University Press, 2000.
[11] M. Scully, M. Zubairy, Quantum optics, Cambridge University Press, 1997.
[12] G. Breitenbach, S. Schiller, J. Mlynek, Measurement of the quantum states of squeezed light, Nature 387, 471 (1997).
[13] G. Breitenbach, T. Muller, S. F. Pereira, et. al., Squeezed vacuum from a monolithic optical parametric oscillator, JOSA B 12, 2304 (1995).
[14] G. Breitenbach, S. Schiller, Homodyne tomography of classical and non-classical light, Jour. Mod. Opt. 44, 2207 (1997).
[15] P. Saulson, Fundamentals of Interferometric Gravitational Wave Detectors, World Scientific, 1994.
[16] A. E. Siegman, Lasers, Academic Press, 1986.
[17] A. Yariv, Quantum electronics, Wiley, 1989.
[18] Photodiode Technical Information, Characteristics and use of SI APD, http://sales.hamamatsu.com/en/support/technical-notes.php
[19] P. Horowitz, W. Hill, The art of electronics, Cambridge University Press, 1989.

Chapter 4

Differential Reflection for Single QD Absorption Measurement

To manipulate quantum dots (QDs) for optically-driven quantum computing (QC), it is fundamental to understand the optical properties of these nanostructures, including emission, absorption, and spin dynamics [1, 2, 3]. The emission spectrum contains information about the energy levels of the QDs. The absorption properties provide information about how to optically drive QDs efficiently. The spin dynamics help to find optimized schemes to manipulate the spin optically for spin based QC. To explore quantum dot based quantum computing (QDQC) all these optical properties needed to be experimentally measured. To measure these optical properties of a single QD, sensitive experimental techniques are crucial. Differential Transmission (DT) is a powerful laser spectroscopy technique to study the absorption and spin dynamics of QDs [4, 5, 6, 7]. DT has been used to read out the quantum state of the QDs for QC [8]. Even current measurements requires averaging over multiple measurements due to low SNR, which limits scaling the DT to real QC systems, DT with ultrafast lasers provides a convenient and accurate way for rapid quantum state tomography [9].

Previous studies on QDQC have used DT to study the nonlinear optical properties of interface fluctuation quantum dots (IFQDs). The transmission geometry works well for neutral QDs or doped QDs, where the substrate can be removed from the sample. However, in order to be able to control the number of electrons in the QD, electric gates must be attached to the substrate. This requires that the GaAs substrate be retained, and prohibits transmission studies as the

energy of the IFQDs is above the GaAs band gap. Study in a reflection geometry is required for electrically gated IFQDs [10].

In this chapter, differential measurements are extended to the reflection geometry. First, the sample structure of the electrically gated IFQDs is introduced. Then phase sensitive bandwidth reduced detection with lock-in amplifiers is presented to show how to measure small signals out of noise by narrowing the bandwidth. Next, the physics of the nonlinear spectroscopic DT signal is reviewed through the density matrix equations and Maxwell-Bloch equations, and homodyne detection with lock-in amplifiers is explained to illustrate how a weak nonlinear optical signal can be measured out of a noisy background. At the end of the chapter, the differential reflection (DR) technique is discussed accounting for the phase shifts on reflection and relating the spectrum to the terms to the solution of the density matrix equations using the third order perturbation theory. Nonlinear absorptions of ensemble and single IFQDs are measured with the DR technique.

4.1 Bandwidth reduced detection with Lockin amplifiers

To study the optical properties of quantum dots, we need to measure both the linear and nonlinear absorption in order to obtain all the fundamental parameters. As shown in experiments, the linear and nonlinear absorption signals, represented as the ratio between the absorbed light and the incident light, are very small, on the order of 10^{-4} for the linear absorption and 10^{-6} for nonlinear absorption [11, 12, 13], which is sometimes comparable with the laser noise (10^{-3} to 10^{-6}) in our experiments as we demonstrated in Chapter 2. Special experimental techniques are required to measure the weak signal from a single quantum dot. In this section first we will discuss how the bandwidth affects the signal-noise-ratio (SNR) and how lock-in amplifiers achieve bandwidth reduced detection.

As we have seen in Chapter 3, electrical thermal noise and laser shot noise are forms of white noise uniformly spread out over all frequencies. The common mode laser noise of the dye laser in our experiment drops, from 10^{-3} at DC down to 10^{-7} near the shot-noise-limit (SNL) at a few MHz. Within a small bandwidth

(100Hz to 0.3Hz) for center frequencies under 100KHz, the total noise is dominated by common mode noise, a few orders of magnitude above the SNL.

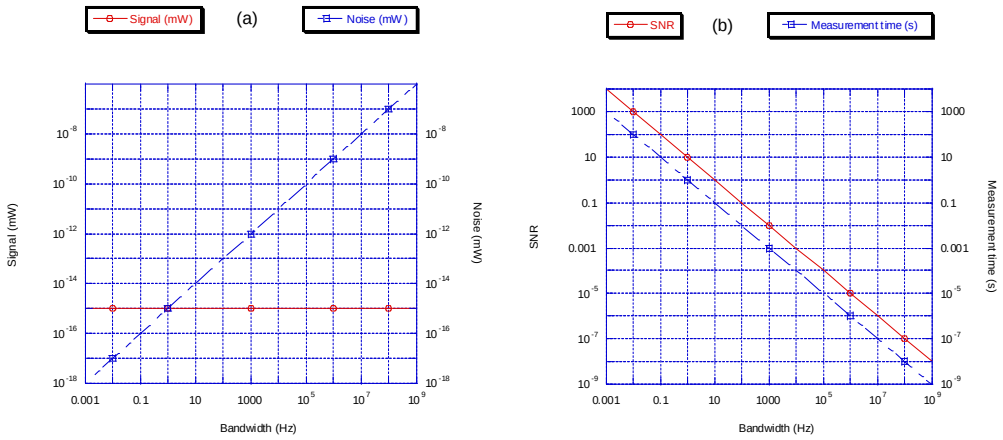

Fig. 4.1 Bandwidth effect on signal, noise and SNR (a) signal and noise versus bandwidth (b) SNR and measurement time versus bandwidth

An important property of noise is that the noise power is integrated over the bandwidth of the measurement. For a flat noise spectrum, the noise power is directly proportional to the measurement bandwidth. However, usually the signal is at a single frequency, and its strength is independent of the measurement bandwidth. By reducing the measurement bandwidth, the noise can be reduced without reducing the signal strength so that the SNR can be improved. Figure 4.1(a) illustrates the effect of bandwidth on the signal, noise, and SNR. It shows that a weak signal comparable to the noise can be measured with a SNR of 10 by reducing the bandwidth from 1Hz to 0.1Hz.

The increase in SNR comes at the cost of measurement bandwidth, thus extending the required measurement time, as shown in Figure 4.1(b). The experimental system needs be stable during the long measurement time so that the random noise can be averaged out while the signal is not affected. In principle, the SNR can be infinitely improved by narrowing the measurement bandwidth. In actual experiments, the bandwidth cannot be made infinitely narrow due to limited system stability.

The simplest way to achieve a reduced bandwidth is to use a narrow bandpass filter at the central frequency. However, it is very hard to make narrow band pass filters for high frequencies compared to low frequency. The best narrow band pass filters are available only at DC. A lock-in amplifier is an instrument that converts AC signals into DC signals with adjustable narrow band pass filters at DC to achieve phase sensitive bandwidth reduced detection.

Figure 4.2 illustrates the functional diagram of a lock-in amplifier. The input first passes through a preamplifier. Then the amplified input mixes with a reference sine wave to convert the input into a high frequency and a low frequency component. After passing through the narrow-band low-pass filter centered at DC, only the signal in phase at the reference frequency survives [14].

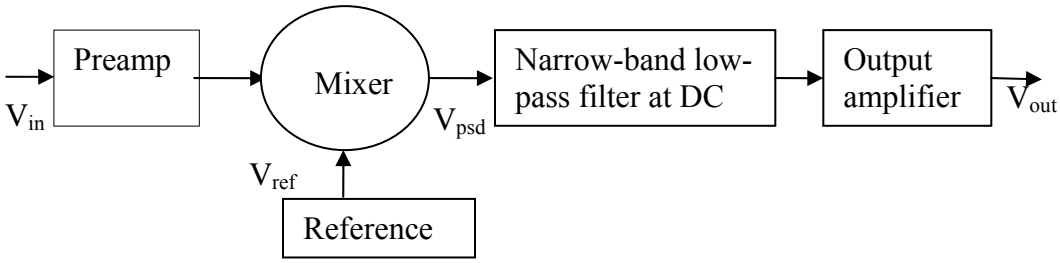

Figure 4.2 A functional diagram of a lock-in amplifier

Assume the input contains a single frequency signal with a constant phase, a broadband noise with random phase, and a DC offset as

$$V_{in} = V_{signal}\sin(\omega_{signal}t + \varphi_{signal}) + V_{noise}\sin(\omega_{noise}t + \varphi_{noise}) + V_{DC} \qquad (4\text{-}1)$$

where V_{signal} is the signal amplitude, ω_{signal} is the signal frequency, φ_{signal} is the constant phase of the signal, V_{noise} is the noise amplitude, ω_{noise} is the noise frequency covering a broad band, φ_{noise} is the random phase of the noise, and V_{DC} is the DC offset.

The reference is a pure sinusoidal wave as $V_{ref}\sin(\omega_{ref}t + \varphi_{ref})$, where V_{ref} is the reference amplitude, ω_{ref} is the frequency of the reference, and φ_{ref} is the phase of the reference. After the preamplifier, the DC offset is filtered out. After the mixer we get

$$V_{psd} = (V_{signal}\sin(\omega_{signal}t + \varphi_{signal}) + V_{noise}\sin(\omega_{noise}t + \varphi_{noise}))V_{ref}\sin(\omega_{ref}t + \varphi_{ref})$$

$$= \frac{1}{2}V_{signal}V_{ref}(\cos[(\omega_{signal} - \omega_{ref})t + (\varphi_{signal} - \varphi_{ref})] + \cos[(\omega_{signal} + \omega_{ref})t + (\varphi_{signal} + \varphi_{ref})])$$

$$+ \frac{1}{2}V_{noise}V_{ref}(\cos[(\omega_{noise} - \omega_{ref})t + (\varphi_{noise} - \varphi_{ref})] + \cos[(\omega_{noise} + \omega_{ref})t + (\varphi_{noise} + \varphi_{ref})])$$

.

After the narrow band low pass filter at DC, only the frequency components near the reference frequency with a frequency difference less than the filter bandwidth will pass. The in phase component will give a maximum signal. Applying the condition $\omega_{in} = \omega_{ref}$ and $\varphi_{in} = \varphi_{ref}$, we get

$$V_{out} = \frac{1}{2}(V_{in} + V_{noise}\cos((\varphi_{noise} - \varphi_{in})))V_{ref}. \quad (4\text{-}2)$$

This shows that the lock-in amplifier only selectively measures AC signals in phase with the reference at the reference frequency within the narrow bandwidth. Noise at other frequencies will be frequency shifted, but remain as AC rather than DC. Noise at the reference frequency varies in phase with respect to the reference phase and gives a varying DC. Then, by using a narrow band filter with a tunable bandwidth, all the noise above a certain frequency threshold can be filtered out. The noise passing through the lock-in amplifier is only the noise at the reference frequency in phase with the reference.

Based on the noise properties we discussed in chapter 3, bandwidth reduced detection with lock-in amplifiers is still subject to the total noise at the reference frequency in the system, which is usually 1/f noise, for two reasons. The first reason is that lock-in amplifiers usually work in a low frequency range (0.001-100KHz), where the 1/f noise is dominates. The second reason is that absorption measurements require multiple measurements of absorption over a range of wavelengths. The 1/f noise affects the periodic measurement when the wavelength is scanned.

4.2 Differential transmission

To take the advantage of bandwidth reduced detection, the DT technique has been developed to measure nonlinear spectroscopic signals [15, 16, 17, 18]. In

this section, the physics of the nonlinear spectroscopic signals and the DT experimental technique employed to measure nonlinear signals are explained. First, solving the density matrix equations gives a theoretical description of the linear and nonlinear polarization of the system. Then a derivation of the Maxwell-Bloch equations shows the relation between the signal electric field and the polarization. Next, the DT technique illustrates how a weak nonlinear signal is measured with a lock-in amplifier.

4.2.1 Spectroscopy signals from material polarization

When studying the optical properties of quantum dots, the quantum dots are excited and the optical properties are probed with laser beams. The electric field of the laser beam creates polarizations in the quantum dots, which give rise to the spectroscopic signals to be measured. Here density matrix theory is used to explain the physics of the polarization and the Maxwell equations are solved to illustrate the spectroscopic signal caused by the polarization.

Density matrix theory [19] describes the material response to excitation by external fields. A simple closed two-level system, as illustrated in Figure 4.3, is used here to illustrate the material response as material polarization under optical excitation from the laser beams.

For a two-level system, the wave function $|\psi\rangle$ is

$$|\psi\rangle = a_1|1\rangle + a_2|2\rangle \tag{4-3}$$

where a_1 and a_2 are the probability amplitudes of states $|1\rangle$ and $|2\rangle$, respectively.

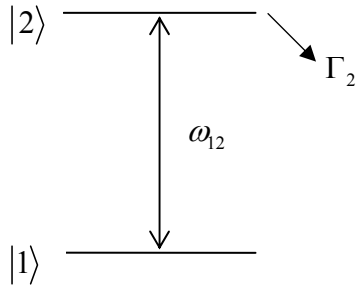

Figure 4.3 A closed two-level system with a transition ω_{12} and population decay rate Γ_2

The Schrödinger equation is

$$i\hbar\dot{\vec{a}} = H\vec{a} \tag{4-4}$$

$$H = \hbar\begin{bmatrix} -\omega_{12} & X_{12} \\ X_{12} & 0 \end{bmatrix} \tag{4-5}$$

$$X_{12} = -\frac{\vec{\mu}_{12}\bullet\vec{E}}{\hbar} = \chi_{12}e^{i\omega_{12}t} + c.c. \tag{4-6}$$

where $\hbar$ is the Plank constant, $\vec{a}$ is the wave function, H is the Hamiltonian, ω_{12} is the frequency of the transition between the two levels, X_{12} is the interaction, $\vec{\mu}_{12}$ is the dipole moment of the transition, and $\vec{E}$ is the electrical field.

The density matrix equations of motion are

$$i\hbar\dot{\rho} = \left[H,\rho\right] + i\hbar\dot{\rho}\big|_{relaxation} \tag{4-7}$$

$$\begin{aligned} \dot{\rho}_{11} &= -iX_{12}\rho_{21} + iX_{12}\rho_{12} + \Gamma_2\rho_{22} \\ \dot{\rho}_{22} &= iX_{12}\rho_{21} - iX_{12}\rho_{12} - \Gamma_2\rho_{22} \\ \dot{\rho}_{12} &= i\omega_{12}\rho_{12} - iX_{12}\left[\rho_{22} - \rho_{11}\right] - \gamma\rho_{12} \end{aligned} \tag{4-8}$$

where γ is the coherence decay rate, and Γ_2 is the population decay rate.

Utilizing the rotating wave approximation and solving the density matrix equations under a cw field $\vec{E} = Ee^{-i(\vec{k}\bullet\vec{R}-\omega t)}$ with a perturbation approach we get

$$\rho_{12}^{(1)} = \frac{i\mu E}{2\hbar}\frac{N_0}{\gamma + i(\omega-\omega_{12})}e^{-i(\vec{k}\bullet\vec{R}-\omega t)} \tag{4-9}$$

$$\rho_{12}^{(3)} = \frac{i\mu^3E^3}{8\hbar^3}\frac{N_0}{\gamma + i(\omega-\omega_{12})}\frac{2\gamma}{\gamma^2 + (\omega-\omega_{12})^2}\frac{2}{\Gamma_2}e^{-i(\vec{k}\bullet\vec{R}-\omega t)}. \tag{4-10}$$

The material polarization induced by the optical excitation is

$$\vec{P} = N\left\langle\mu\right\rangle = NTr(\mu\rho) = N\sum(\mu_{12}\rho_{21} + c.c.). \tag{4-11}$$

From a macroscopic picture, when light interact with materials it causes induced polarization, which can be expressed in terms of material susceptibility.

$$\vec{P} = \sum_i \varepsilon_0\chi^{(1)}\vec{E}_i + \sum_{i,j}\varepsilon_0\chi^{(2)}\vec{E}_i\vec{E}_j + \sum_{i,j,k}\varepsilon_0\chi^{(3)}\vec{E}_i\vec{E}_j\vec{E}_k + \ldots \tag{4-12}$$

where ε_0 is the permittivity of free space, and $\chi^{(n)}$ is the nth order of the susceptibility. The first order susceptibility $\chi^{(1)}$ gives linear absorption and dispersion. The second order susceptibility $\chi^{(2)}$ gives second harmonic generation, sum and difference frequency generation, and optical rectification. The third order susceptibility $\chi^{(3)}$ gives the third harmonic generation, four-wave-mixing, and phase conjugation. For centro-symmetric crystals, all even order polarizations vanish due to crystal symmetry. Higher order polarizations are ignored since they are much weaker than the 1st and 3rd order terms.

For the two-level system, perturbation theory shows that polarizations only appear for odd orders, and the population terms occur for even orders. Based on the calculation of a two-level system with density matrix equations and Maxwell-Bloch equations, the first and the third order nonlinear polarization is

$$\chi^{(1)} = \frac{i|\mu|^2}{2\hbar(\gamma - i\Delta)} = \frac{|\mu|^2 (i\gamma - \Delta)}{2\hbar(\gamma^2 + \Delta^2)} \tag{4-13}$$

$$\chi^{(1)}{}_{real} = \frac{-\Delta|\mu|^2}{2\hbar(\gamma^2 + \Delta^2)} \tag{4-14}$$

$$\chi^{(1)}{}_{imaginary} = \frac{\gamma|\mu|^2}{2\hbar(\gamma^2 + \Delta^2)} \tag{4-15}$$

$$\chi^{(3)} = \frac{2i|\mu|^4}{8\hbar^3(\gamma - i\Delta)} \frac{1}{\Gamma_2} \frac{4\gamma}{\gamma^2 + \Delta^2} = \frac{|\mu|^4 \gamma(i\gamma - \Delta)}{\hbar^3 \Gamma_2 (\gamma^2 + \Delta^2)^2} \tag{4-16}$$

$$\chi^{(3)}{}_{real} = \frac{-|\mu|^4 \gamma\Delta}{\hbar^3 \Gamma_2 (\gamma^2 + \Delta^2)^2} \tag{4-17}$$

$$\chi^{(3)}{}_{imaginary} = \frac{|\mu|^4 \gamma^2}{\hbar^3 \Gamma_2 (\gamma^2 + \Delta^2)^2}. \tag{4-18}$$

where $\Delta = \omega_{12} - \omega$ is the detuning.

The real part of the susceptibility is related to the refractive index, and the imaginary part is related to the absorption. In the case of the linear response the two parts are related through Kronig-Kramer relation. It is worth noticing that the

first order susceptibility is a Lorentzian curve and the third order susceptibility is a Lorentzian squared curve, as plotted in Figure 4.4.

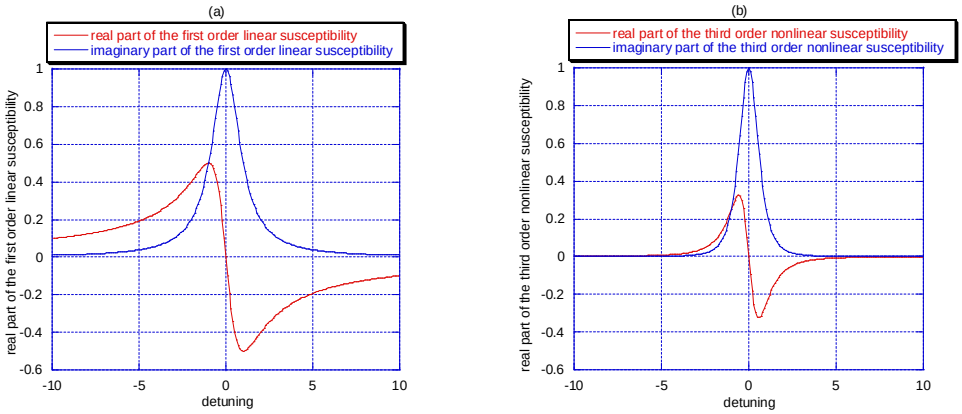

Figure 4.4 Real and imaginary part of the first and third order susceptibilities (a) Real and imaginary part of the first order linear susceptibility (b) Real and imaginary part of the third order linear susceptibility

The density matrix gives the nonlinear susceptibility from material polarization under optical excitation. Using the polarization as the source term in the Maxwell equations we can obtain the signal containing the spectroscopic information of the nonlinear susceptibility.

The Maxwell equations are

$$\nabla \bullet \vec{D} = 0 \tag{4-19}$$

$$\nabla \times \vec{E} = 0 \tag{4-20}$$

$$\nabla \bullet \vec{B} = 0 \tag{4-21}$$

$$\nabla \times \vec{H} = \mu \frac{\partial \vec{D}}{\partial t} \tag{4-22}$$

$$\vec{D} = \varepsilon \vec{E} + \vec{P} \tag{4-23}$$

$$\vec{B} = \mu \vec{H} + \vec{M}\,, \tag{4-24}$$

where $\vec{D}$ is the electric displacement, $\vec{E}$ is the electric field, $\vec{B}$ is the magnetic induction, $\vec{H}$ is the magnetic field, and $\vec{M}$ is the magnetization.

To solve the Maxwell's equation, we take the curl of Equation (4-22) and substitute equation (4-22) in to find

$$\nabla(\nabla\bullet\vec{E})-\nabla^2\vec{E}=-\frac{1}{c^2}\frac{\partial^2\vec{E}}{\partial t^2}-\mu\frac{\partial^2\vec{P}}{\partial t^2}. \tag{4-25}$$

Two approximations are made here to solve the equation. The first, $\nabla\bullet\vec{E}=0$, means that there is no net charge density due to the material polarization. It is valid in our experiments since there is no net charge creation. The second is that the electric field propagation is treated in the plane wave approximation, meaning that the longitudinal field is negligible. This is appropriate in our experiments since all detection is through lens systems at far fields. Applying these approximations yields

$$\frac{\partial^2\vec{E}}{\partial z^2}=\frac{1}{c^2}\frac{\partial^2\vec{E}}{\partial t^2}+\mu\frac{\partial^2\vec{P}}{\partial t^2}. \tag{4-26}$$

Assuming a solution of the form

$$\vec{E}=\tilde{E}e^{ikz}e^{-i\omega t}+c.c. \tag{4-27}$$

$$\vec{P}=\tilde{P}e^{ikz}e^{-i\omega t}+c.c., \tag{4-28}$$

we get the following terms

$$\begin{aligned}
\frac{\partial^2\vec{E}}{\partial z^2}&=\frac{\partial^2}{\partial z^2}\left(\tilde{E}e^{ikz}e^{-i\omega t}\right)=\left(\frac{\partial^2}{\partial z^2}+2ik\frac{\partial}{\partial z}-\omega^2\right)\tilde{E}e^{i(kz-\omega t)}\\
\frac{\partial^2\vec{E}}{\partial t^2}&=\frac{\partial^2}{\partial t^2}\left(\tilde{E}e^{ikz}e^{-i\omega t}\right)=\left(\frac{\partial^2}{\partial t^2}-2ik\frac{\partial}{\partial t}-\omega^2\right)\tilde{E}e^{i(kz-\omega t)}\\
\frac{\partial^2\vec{P}}{\partial t^2}&=\frac{\partial^2}{\partial t^2}\left(\tilde{P}e^{ikz}e^{-i\omega t}\right)=\left(\frac{\partial^2}{\partial t^2}-2ik\frac{\partial}{\partial t}-\omega^2\right)\tilde{P}e^{i(kz-\omega t)}
\end{aligned}. \tag{4-29}$$

For cw measurement, in the slow varying envelop approximation (SVEA), the fast time varying components, $\frac{\partial^2\tilde{E}}{\partial t^2}$ and $\frac{\partial^2\tilde{P}}{\partial t^2}$, and the fast spatially varying components, $\frac{\partial^2\tilde{E}}{\partial z^2}$, can be ignored. Equation (4-24) reduces to

$$(2ik\frac{\partial}{\partial z}-k^2+\frac{\omega^2}{c^2})\tilde{E}+\mu\omega^2\tilde{P}=0. \tag{4-30}$$

Since $k = \frac{\omega}{c}$, we thus get the Maxwell-Bloch Equation

$$\frac{\partial \tilde{E}}{\partial z} = i\frac{k}{2\varepsilon}\tilde{P} \tag{4-31}$$

For an optically thin sample with a thickness of *l*,

$$\tilde{E} = i\frac{kl}{2\varepsilon}\tilde{P} \tag{4-32}$$

The Maxwell-Bloch equation [20] gives a linear relation between the signal electric field and the material polarization. Higher order of polarizations have nonlinear dependences on the electric fields of the exciting light, but the signal electric field is still proportional to the polarization. Since the polarization of a single QD radiates as a dipole, the signal radiates in the dipole radiation pattern, with maximum radiation occurring in the plane perpendicular to the dipole orientation.

4.2.2 Homodyne detection with differential transmission

Usually the nonlinear spectroscopic signals from QDs are very small, especially for a single QD. To detect the small signals, a homodyne scheme that measures the mixing of the signal electric field and a reference electric field from the same laser beam is used. DT is an experimental spectroscopy technique used to measure the optical signal in a pump-probe setup. The simplest version of the DT is a single chopping scheme, as illustrated in Figure 4.6. A pump laser beam and a probe laser beam are incident upon a QD sample from two slightly different angles. The pump beam is intensity modulated with an acousto-optic modulator or a mechanical chopper, and the probe beam is not modulated. For both the pump and the probe beams, most of the light is specularly reflected, a small portion of light interacts with QDs and gets scattered to all directions with spectroscopic signals, and some light propagates through the sample along the original direction. After the sample, the pump and probe beams propagate in different directions. Blocking the pump beam after the sample, the transmitted probe beam and forward scattered pump and probe light are collected by a lens and imaged on a detector. The DT signal is detected at the pump modulation frequency with a

lock-in amplifier. The laser wavelength is scanned for both the pump and the probe to map out the DT signal over a wavelength range.

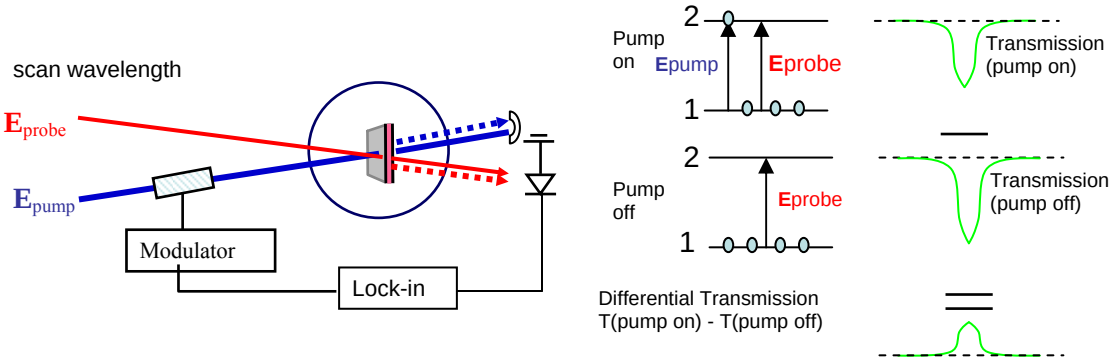

Figure 4.5 DT setup

A simple picture of DT is also illustrated in Figure 4.5. When the pump is off all population is in the ground state, and the probe beam experiences a certain amount of absorption. When the pump is on, some population is pumped to the excited state, and the probe beam experienced slightly less absorption. DT detects the difference of absorption between the pump on and pump off.

The exact DT signal can be obtained by analyzing signals on the detector. When the pump beam is off, the detector measures the transmitted and forward scattered probe beam.

$$I_{DT-pump-off} = \left| E_{transmitted-probe}(f=0) + E_{forward-scattered-probe}(f=0) \right|^2 \qquad (4\text{-}33)$$

where $E_{transmitted-probe}$ is the electric field of the probe beam transmitted through the sample hitting the detector, $E_{forward-scattered-probe}$ is the electric field of the forward scattered probe beam, and f represents frequency. Since the probe beam is not modulated, all pure probe related intensities are at DC $(f=0)$. If the transmitted probe is a few orders of magnitude stronger than the scattered probe, it is impossible to extract the spectroscopic signal from the huge background of the transmitted probe unless additional experimental techniques are used.

When the pump beam is on, the detector detects the electric field of the transmitted probe and the electric field of the forward scattered signal caused by both pump and probe.

$$I_{DT-pump-on} = \left| E_{transmitted-probe}(f=0) + E_{forward-scattered-probe}(f=0) + E_{forward-scattered-pump}(f \neq 0) \right|^2 \tag{4-34}$$

where $E_{forward-scattered-pump}$ is the electric field of the forward scattered signal caused by the pump beam. Since the pump beam is modulated and no transmitted pump beam hits the detector, the scattered pump is separated from the scattered probe by frequency. The weak scattered pump is at the pump beam modulation frequencies or its higher order harmonics. All pure probe beam effects, including the strong transmitted probe and the weak scattered probe, remains as a DC background. By using narrow band phase-sensitive detection with a lock-in amplifier to detect signals at the modulation frequency, the small spectroscopic signal in the scattered pump can be measured out of a large DC background caused by the transmitted probe with homodyne detection.

The DT signal on the detector is.

$$I_{DT} = 2\,\mathrm{Re}(E_{transmitted-probe}{}^{*} E_{forward-scattered-pump}) \tag{4-35}$$

$$E_{transmitted-probe} = t\vec{E}_{probe} e^{i\phi_{transmission}}, \tag{4-36}$$

where t is the transmission coefficient, and $\phi_{transmission}$ is the phase of the transmitted beam, which is same for the transmitted probe and forward scattered pump since their propagation paths are the same.

From Equation (4-12) and (4-32), we get

$$E_{forward-scattered-pump} = i\frac{kl}{2\varepsilon}\left(\varepsilon_0 \chi^{(1)} \vec{E}_{pump} + \sum_{i,j,k} \varepsilon_0 \chi^{(3)} \vec{E}_i \vec{E}_j \vec{E}_k + \ldots \right) e^{i\phi_{transmission}}, \tag{4-37}$$

where i,j,k could be either the pump or the probe and at least one of them should be the pump. At the pump beam modulation frequency the dominant terms are the third order polarization without any other background.

$$E_{forward-scattered-pump}(f) = i\frac{kl}{2\varepsilon}\varepsilon_0 \chi^{(3)} \vec{E}_{pump} \vec{E}_{pump}{}^{*} \vec{E}_{probe}{}^{*} e^{i\phi_{transmission}} \tag{4-38}$$

$$I_{DT}(f) = 2\,\mathrm{Re}\left(i\frac{kl}{2\varepsilon}\varepsilon_0\chi^{(3)}\vec{E}_{pump}\vec{E}_{pump}{}^{*}\vec{E}_{probe}t\vec{E}_{probe}{}^{*} \right) = \frac{\varepsilon_0 klt}{\varepsilon}\mathrm{Im}\left(\chi^{(3)}\right) I_{pump}I_{probe} \tag{4-39}$$

This shows that the DT only measures the imaginary part of the 3rd order nonlinear susceptibility. The key is that the transmitted probe experiences the exact same optical path as the forward scattered signal caused by the polarization in the transmission geometry. Transmission always measures the absorption, which is related to the imaginary part of the susceptibility.

Single chopping is a good choice when the pump and probe beams can be separated in space or by polarization so that the detector only detects the probe beam. For single dot spectroscopy with small apertures, it is hard to separate the pump and the probe beams on the detector. Double chopping with both the pump and the probe modulated at two different frequencies measures DT at the difference frequency. The high sensitivity of the DT comes from optical modulation. Most noise in experiments, like air flow, mechanical vibration, and laser noise, is distributed in the low frequency regime. By choosing the proper optical modulation frequency, usually a few MHz, noise at other frequencies can be inhibited to measure small signals. With DT, the linear absorption of a single dot has been measured with non-resonant excitation [11], and the nonlinear absorption of a single dot has been studied with resonant excitation [15].

Ensemble and single dot nonlinear spectroscopic signals have been measured with DT earlier in our labortary, as shown in Figure 4.6. Photoluminescence (PL) is also shown as a reference. In ensemble studies with large apertures with diameters on the order of tens of microns, a large number of QDs give an inhomogeneously broadened spectrum in both PL and DT that overlaps in energy. There are mainly two 2meV wide peaks separated by about 8meV appearing in both the PL and DT scans, corresponding to the monolayer fluctuation in IFQDs. The relative strengths of the two monolayers are different for the two scans. The lower energy monolayer gives strong PL and weak DT, the higher energy monolayer shows weak PL and strong DT.

In single dot studies through sub-micron size small apertures, discrete states of single QDs can be resolved as narrow peaks at difference frequencies in both photoluminescence and nonlinear absorption. Most states show PL and DT at the same frequency. A few states shown in PL are not observed in DT, and some states appear in DT are not observed in PL. The left inset shows a DT state with fine energy resolution, which is well fit to a Lorentzian squared as the theory predicts.

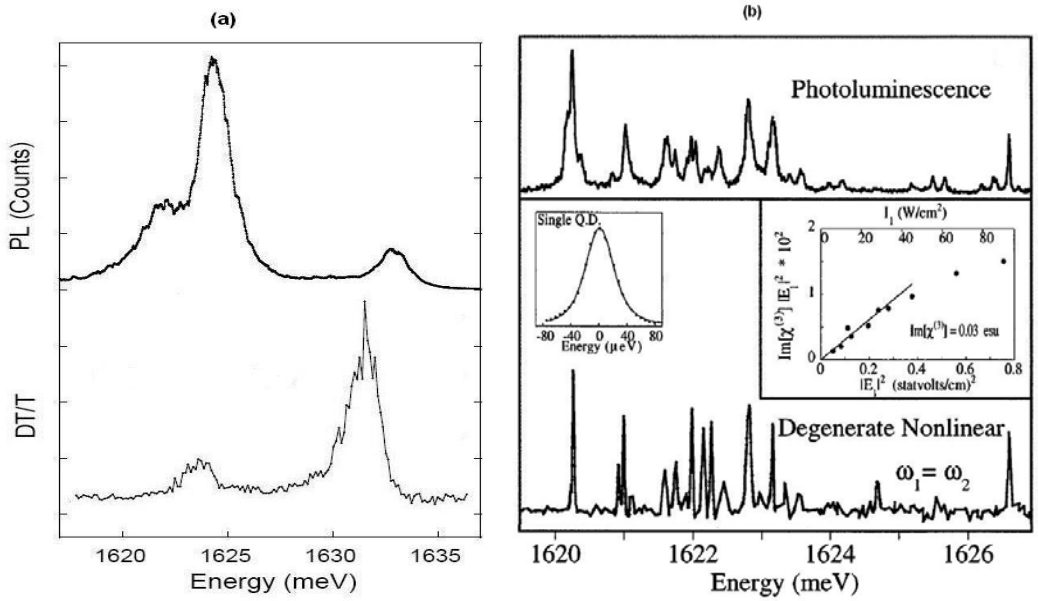

Figure 4.6 DT scans for an ensemble of IFQDs and single IFQDs (a) The PL and DT/T of an ensemble QDs measured with a 25um diameter aperture (b) The PL spectrum through a 0.5 um aperture at low resolution and degenerate nonlinear spectrum (Right inset) The power dependence of the DT signal. (Left inset) A Lorentzian squared fit to a high resolution degenerate nonlinear response. (Figure Bonadeo[21])

4.3 Differential reflection

Differential Reflection (DR) is a modification of DT that extends the capability of nonlinear laser spectroscopy to the reflection geometry, enabling measurement of both the real and the imaginary parts of the nonlinear susceptibility. In this section, first the theory of DR is explained and then some simulation results are

presented. At the end of this section DR measurements on quantum dots are presented.

4.3.1 Theory of the differential reflection

A different approach to solving the problem is to use the reflected light rather than the transmitted light. Both reflected and transmitted light carry the optical information of the QD. DT detects the homodyne signal by collecting the forward transmitted light. Similarly, the homodyne signal can also be obtained by detecting the backward reflected or scattered light with a beam splitter, as illustrated in Figure 4.7 in a double chopping scheme. We call this differential reflection. DR measures the nonlinear susceptibility using the reflected probe beam and back scattered signal. The only difference between DT and DR is the phase difference caused by a round trip of light propagation from the sample surface to a distance *d* below the surface, as shown in Figure 4.7.

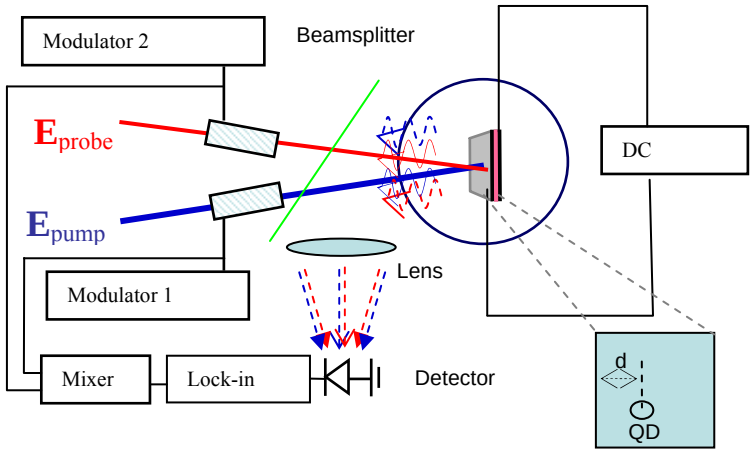

Figure 4.7 Differential Reflection setup

The detector collects all the light hitting the detector, which includes the reflected probe and back scattered light of both the pump and the probe. In writing the intensity of light hitting the detector, we have

$$I_{DR} = \left| E_{reflected-probe}(f=0) + E_{backward-scattered-probe}(f=0) + E_{backward-scattered-pump}(f\neq 0) \right|^2 \quad (4\text{-}40)$$

where $E_{reflected-probe}$ is the electric filed of the reflected probe, $E_{backward-scattered-probe}$ is the electric field of the back scattered probe, and $E_{backward-scattered-pump}$ is the electric field of the back scattered pump. Only $E_{backward-scattered-pump}$ is modulated and the other two are DC.

As we have analyzed for DT, the signal we are interested in is the homodyne detected reflected probe beam and the scattered pump.

$$I_{DR} = 2\,\mathrm{Re}(E_{reflected-probe}{}^{*} E_{backward-scattered-pump}). \tag{4-41}$$

The reflected probe is mainly from the reflection at the top surface of the QD sample, which is different from the backward scattered pump at the QD by a reflection coefficient and a phase shift caused by propagating a distance 2d. This yields

$$\vec{E}_{reflected-probe} = r\vec{E}_{probe} \tag{4-42}$$

$$E_{backward-scattered-pump} = i\frac{kl}{2\varepsilon}\left(\varepsilon_0\chi^{(1)}\vec{E}_{pump} + \sum_{i,j,k}\varepsilon_0\chi^{(3)}\vec{E}_i\vec{E}_j\vec{E}_k + \ldots\right)e^{i\phi_{reflection}} \tag{4-43}$$

$$\phi_{reflection} = 2\pi\frac{2d}{\lambda} \tag{4-44}$$

where r is the reflection coefficient, and ϕ is the phase shift.

$$E_{backward-scattered-pump}(f) = i\frac{kl}{2\varepsilon}\varepsilon_0\chi^{(3)}\vec{E}_{pump}\vec{E}_{pump}{}^{*}\vec{E}_{probe}{}^{*}e^{i\phi_{reflection}} \tag{4-45}$$

Employing the same phase-sensitive narrow band detection scheme using a lock-in amplifier, DR measures the nonlinear susceptibility at the pump modulation frequency:

$$I_{DR}(f) = 2\,\mathrm{Re}\left(i\frac{kl}{2\varepsilon}\varepsilon_0\chi^{(3)}\vec{E}_{pump}\vec{E}_{pump}{}^{*}\vec{E}_{probe}\vec{E}_{reflected-probe}{}^{*}\right). \tag{4-46}$$

Using equation (4-42) we get

$$I_{DR}(f) = 2\,\mathrm{Re}\left(i\frac{kl}{2\varepsilon}\varepsilon_0\chi^{(3)}\vec{E}_{pump}\vec{E}_{pump}{}^{*}\vec{E}_{probe}{}^{*}r\vec{E}_{probe}e^{i\phi_{reflection}}\right) = \frac{kl\varepsilon_0 r}{\varepsilon}\mathrm{Im}\left(-\chi^{(3)}e^{i\phi_{reflection}}\right)I_{pump}I_{probe} \tag{4-47}$$

Separating the real and imaginary parts, we get

$$I_{DR}(f) = -\frac{kl\varepsilon_0 r}{\varepsilon}\left(\chi^{(3)}{}_{real}\sin\phi_{reflection} + \chi^{(3)}{}_{imaginary}\cos\phi_{reflection}\right)I_{pump}I_{probe}. \tag{4-48}$$

This shows that DR measures a combination of the real and imaginary parts of the nonlinear susceptibility depending on the phase difference between the reflected probe and the probe at the QD.

From Section 4.2.1 we know that the real and imaginary part of the third order nonlinear susceptibility have different line shapes. The real part is derivative-like and the imaginary part is a Lorentzian squared. Depending on the phase difference in the reflection geometry, the DR signal has a combination of the derivative and Lorentzian square shape. To show the effect of the phase difference $\phi_{reflection}$ on the DR signal, a few simulations are performed for different phases, as illustrated in Figure 4.8. When $\phi_{reflection} = k\pi$ (k is an integer), DR measures only the imaginary part of the third order nonlinear susceptibility, just as DT does. When $\phi_{reflection} = k\pi + \frac{\pi}{2}$, DR measures only the real part of the third order nonlinear susceptibility, which is not capable in DT. When $k\pi < \phi_{reflection} < k\pi + \frac{\pi}{2}$, DR measures a combination of the real and imaginary parts of the nonlinear susceptibility.

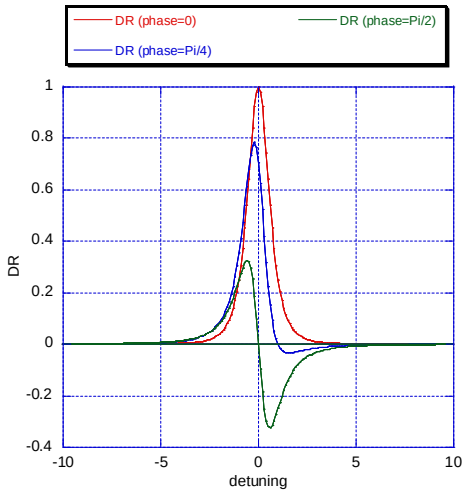

Figure 4.8 Simulation of DR lineshape under a few different phases. (DR gives a Lorentzian squared lineshape when the phase is 0, a derivative lineshape when the phase is $\frac{\pi}{2}$, a superposition of both when the phase is between 0 and $\frac{\pi}{2}$)

Similar results were obtained in the reflection geometry for the first order linear susceptibility of a single QD [22]. With certain phases a combination of real and imaginary parts of the linear susceptibility was measured.

4.3.2 QD absorption measured by differential reflection

With the above setup, DR for an ensemble of QDs and for single QDs from a biased IFQD sample is performed. For the sample studied, n is 3.5, d is 55nm, and λ is 760nm, yielding a phase of approximately π. In our case the DR measures only the imaginary part of the complex susceptibility as DT does.

Ensemble DR over a voltage range 0 to -2V is shown in Figure 4.9, along with the corresponding PL of the same ensemble QDs. Figure 4.9 (a) and (b) are 3D pseudocolor PL and DR absorption maps interpolated from measured data to show the peak energy shift over bias voltage. Figure 4.9 (c) is a plot of the paired measured PL (solid blue line) and DR absorption (dotted red line) data over same energy range under a few different bias voltages. For each bias voltage, PL is measured under non resonant excitation to obtain the photoluminescence over PL energy by a spectrometer. The corresponding absorption of the same ensemble IFQDs is measured with DR under resonant excitation by scanning the laser energy. PL and DR at different bias voltages are vertically shifted for visual clarity. The DR absorption data are global-fitted to Gaussian curves (green dashed curves) with same width and different peak positions. Two black vertical dashed lines are guides to show the PL peaks shift over energy when the bias voltage changes. A purple vertically dashed line is to show the DR peaks shift.

The voltage dependent PL map is dominated by an ensemble IFQDs with PL energy peaked around 1628meV at the voltage range 0 to -1V, shifted from 1631meV at -1.2V to 1630meV at -2V. Since this bias voltage dependence is the same as exciton-trion transitions previously reported [10, 23], and the 3meV energy difference is comparable to the trion binding energy in IFQDs, we assign the PL peak around 1632meV within the voltage range of 0 to -1V as trion (X-), and the PL peak shifted from 1635meV to 1633meV in the voltage range of -1.2V

to -2V as exciton (X). For the ensemble QDs, since the inhomogeneous broadening (2meV) is comparable with the trion binding energy (3meV), excitons and trions from different QDs may overlap in energy. Our assignment only means that from 0 to -1V trions are dominant and form -1.2V to -2V excitons are dominant.

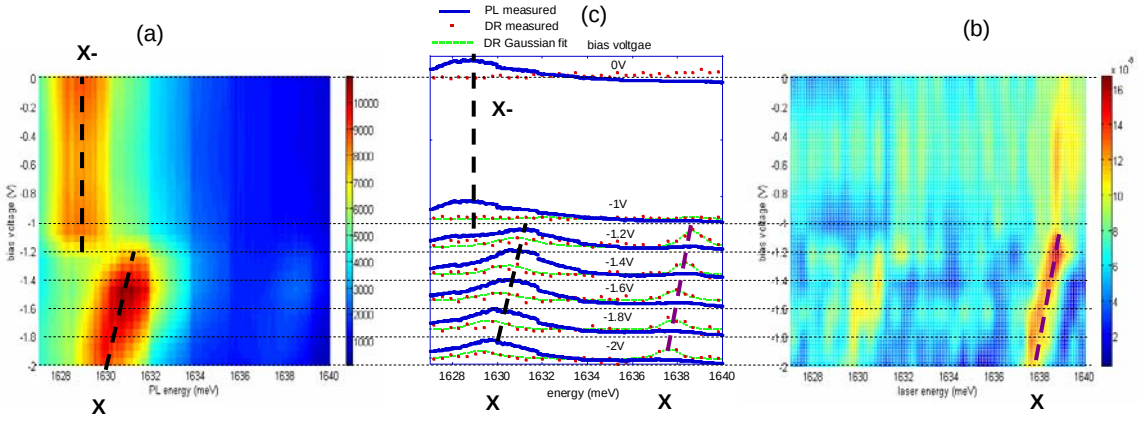

Figure 4.9 Ensemble IFQDs voltage dependent PL and DR absorption map (a) pseudocolor voltage dependent PL map interpolated from measured data (b) pseudocolor voltage dependent absorption map measured with DR interpolated from measured data (c) Measured voltage dependent PL (blue solid lines) and DR (red dotted lines) plots over energy at different bias voltages vertically shifted for clarity (green dashed lines are Gaussian fits.). Two black vertical dashed lines are guides to show the PL peaks shift over energy when the bias voltage changes. A purple vertically dashed line is to show the DR peaks shift.

The voltage dependent DR absorption map is dominated by an ensemble IFQDs with absorption energy peak shifted from 1639meV at -1.2V to 1638meV at -2V. The energy difference between the ensemble PL peak and the DR absorption peak is about 8meV, which is same as the energy difference between the high and low energy monolayers ensemble neutral IFQDs shown in Figure 4.6 (a). We think the strong PL peak is from the lower energy monolayer, which has a strong PL and weak absorption, the strong DR absorption peak is from the higher energy monolayer, which has a weak PL and strong absorption. The same

correlation has been observed in other ensemble IFQDs, as shown in Figure 4.6 (a). Even the lower energy monolayer absorption and the higher energy monolayer PL are too weak to see, the vertically shifted plots in Figure 4.9 (c) show that the PL spectra align with the DR absorption spectra in energy.

With a sub-micron-sized small aperture, DR of a single QD state from the same biased IFQD sample is studied, as shown in Figure 4.10. According to the voltage dependence, most likely this state is an exciton rather than trion. When the bias voltage changes from -0.4V to -0.8V, the absorption peak shifts from 1634.5meV to 1634.2meV. The data were globally fitted to Lorentzian squared curves with same width. The fitted linewidth is $194 \pm 16 \mu eV$, about 2 to 3 times broader than single IFQDs seen in Figure 4.6, which may indicate that the state is a micro-ensemble rather than a single QD. Since the study was to verify the feasibility of DR technique, the data were taken with a coarse wavelength scan without averaging. With a frequency stabilized low noise laser and averaging, the data quality can be improved.

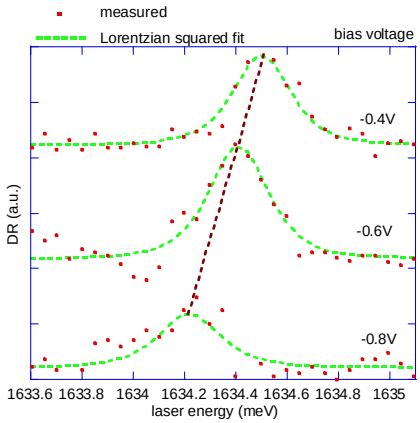

Figure 4.10 Voltage dependent absorption measured with DR (red dotted lines) with Lorentzian squared fit (green dashed lines) of a single or micro ensemble IFQDs. A dashed vertical purple line is a guide to show the absorption peak shifts when the bias voltage changes.

We studied a few biased samples to search for sufficiently strong trion states that absorb light. We did identify some trion states in PL, but they did not exhibit

absorptions. Thus we did not find a suitable trion state with DR for further study. The reason could be that the states shown in PL do not absorb light due to the upper energy state being filled. Further study for the bias voltage dependence of single QD DR will be carried in Chapter 5.

In summary, DR with bandwidth reduced detection was employed to perform nonlinear spectroscopy of QDs. Phase sensitive detection with lock-in amplifiers can improve the SNR by reducing the bandwidth in the measurement. Solutions from the density matrix equations provided lineshapes for the linear and nonlinear susceptibilities. Maxwell-Bloch equation gave the spectroscopic signal from the material polarization caused by optical excitation. Using a homodyne phase sensitive detection with lock-in amplifiers, DT measures the nonlinear absorption caused by imaginary part of the nonlinear susceptibility of QDs. By extending DT to the reflection geometry, DR measures a superposition of the real and imaginary parts of the nonlinear susceptibility of QDs depending on the phase caused by the distance between the QDs and the sample surface. DR of a biased IFQD sample is studied with both ensemble and single QDs. DR from ensemble IFQDs shows an inhomogeneous broadened Gaussian lineshape with voltage dependent. DR of a single IFQD or micro ensemble IFQDs gives a voltage dependent Lorenzian squared lineshape. Search for single trions with strong absorption by DR was not successful due to sample issues.

Bibliography

1 D. Gammon, E. S. Snow, B. V. Shanabrook, D. S. Katzer, D. Park, Homogeneous Linewidths in the Optical Spectrum of a Single Gallium Arsenide Quantum Dot, Science 273, 87 (1996).
2 P. Chen, C. Piermarocchi, L. J. Sham, Control of Exciton Dynamics in Nanodots for Quantum Operations, Phys. Rev. Lett. 87, 067401 (2001).
3 Xiaoqin Li, D. G. Steel, D. Gammon, L. Sham, Optical Excitation in Quantum Dots for Information Processing, Optics and Photonics News, 15, 38 (2004).
4 G. Chen, N. H. Bonadeo, D. G. Steel, D. Gammon, D. S. Katzer, D. Park, L. J. Sham, Optically Induced Entanglement of Excitons in a Single Quantum Dot, Science 289, 1906 (2000).
5 T. H. Stievater, X. Li, D. G. Steel, D. Gammon, D. S. Katzer, D. Park, C. Piermarocchi, L. J. Sham, Rabi oscillations of excitons in single quantum dots, Phys. Rev. Lett. 87, 133603 (2001).
6 A. S. Lenihan, M.V.G. Dutt, D. G. Steel, S. Ghosh, P. K. Bhattacharya, Raman Coherence Beats from Entangled Polarization Eigenstates in InAs Quantum Dots, Phys. Rev. Lett., 88, 223601 (2002).
7 M.V.G. Dutt, J. Cheng; B. Li; X. Xu; X. Li; P. R. Berman, D. G. Steel, A. S. Bracker, D. Gammon, S. E. Economou, R. Liu, L. J. Sham, Stimulated and Spontaneous Optical Generation of Electron Spin Coherence in Charged GaAs Quantum Dots, Phys. Rev. Lett., 94, 227403 (2005).
8 X. Li, Y. Wu, D. Steel, D. Gammon, T. H. Stievater, D. S. Katzer, D. Park, C. Piermarocchi, L. J. Sham, An All-Optical Quantum Gate in a Semiconductor Quantum Dot, Science 301, 809 (2003).
9 Y. Wu, X. Li, L. M. Duan, D. G. Steel, D. Gammon, Density Matrix Tomography through Sequential Coherent Optical Rotations of an Exciton Qubit in a Single Quantu m Dot, Phys. Rev. Lett. 96, 087402 (2006).
10 A. S. Bracker, E. A. Stinaff, D. Gammon, M. E. Ware, J. G. Tischler, A. Shabaev, Al. L. Efros, D. Park, D. Gershoni, V. L. Korenev, and I. A. Merkulov, Optical Pumping of the Electronic and Nuclear Spin of Single Charge-Tunable Quantum Dots, Phys. Rev. Lett. 94, 047402 (2005).
11 N. H. Bonadeo, A. S. Lenihan, G. Chen, J. R. Guest, D. G. Steel, D. Gammon, D. S. Katzer, D. Park, Single quantum dot states measured by optical modulation spectroscopy, Appl. Phys. Lett., 75, 2933 (1999).
12 T. H. Stievater, X. Li, J. R. Guest, D. G. Steel, D. Gammon, D. S. Katzer, D. Park, Wavelength modulation spectroscopy of single quantum dots, Appl. Phys. Lett., 80, 1876 (2002).
13 J. R. Guest, T. H. Stievater, X. Li, J. Cheng, D. G. Steel, D. Gammon, D. S. Katzer, D. Park, C. Ell, A. Thranhardt, G. Khitrova, H. M. Gibbs, Measurement of optical absorption by a single quantum dot exciton, Phys. Rev. B, 65, 241310 (2002).
14 MODEL SR830 DSP Lock-In Amplifier, Stanford Research Systems, 2005.

15 N. H. Bonadeo, G. Chen, D. Gammon, D. S. Katzer, D. Park, D. G. Steel, Nonlinear Nano-Optics: Probing One Exciton at a Time, Phys. Rev. Lett. 81, 2759 (1998).
16 T. H. Stievater, X. Li, D. G. Steel, D. Gammon, D. S. Katzer, D. Park, Transient nonlinear spectroscopy of excitons and biexcitons in single quantum dots, Phys. Rev. B, 65, 205319 (2002).
17 Y. Wu, X. Li, L. M. Duan, D. G. Steel, D. Gammon, Density Matrix Tomography through Sequential Coherent Optical Rotations of an Exciton Qubit in a Single Quantum Dot, Phys. Rev. Lett. 96, 087402 (2006).
18 X. Li, Y. Wu, X. Xu, D. G. Steel, D. Gammon, Transient nonlinear optical spectroscopy studies involving biexciton coherence in single quantum dots, Phys. Rev. B 73, 153304 (2006).
19 M. Scully, M. S. Zubairy, Quantum Optics, Cambridge University Press, 1997.
20 P. Berman, Notes for Quantum Optics, University of Michigan course pack, 2006
21 N. Bonadeo, PhD Thesis, University of Michigan, 1999.
22 B. Alén, A. Högele, M. Kroner, S. Seidl, K. Karrai, R. J. Warburton, A. Badolato, G. Medeiros-Ribeiro, P. M. Petroff, Absorptive and dispersive optical responses of excitons in a single quantum dot, Appl. Phys. Lett. 89, 123124 (2006).
23 R. J. Warburton, C. SchÃ¤flein, D. Haft, F. Bickel, A. Lorke, K. Karrai, J. M. Garcia, W. Schoenfeld, P. M. Petroff, Optical emission from a charge-tunable quantum ring, Nature 405, 926 (2000).

Chapter 5

Voltage Modulation for Single QD Absorption Measurement

In Chapter 4 we used the differential reflection (DR) technique to measure the voltage dependent nonlinear absorption of biased interface fluctuation quantum dots (IFQDs) as a function of wavelength. The voltage-wavelength absorption map of excitons or trions in a single QD is important for manipulating QDs for QC [1-5]. Combined with a voltage dependent PL map of the same QD, excitons and trions can be identified by features including signal strength, voltage range and energy seperation. However, it is not trivial to obtain this voltage dependent absorption map for single QDs due to their small absorption strengths. For IFQDs with relatively large absorption strengths, DT/DR measures the nonlinear absorption of single IFQDs with limited signal-noise-ratio (SNR). When QD based QC moved to using SAQDs, which have comparatively smaller absorption strengths, DT/DR did not give enough SNR. More sensitive absorption measurement techniques needed to be developed.

The main challenge in measuring small absorption signals is to reduce the background noise of a strongly transmitted laser beam. Some noise reduction techniques have been developed to measure the linear absorption of single QDs, but the SNR is still limited by 1/f noise in the low frequency range. For the biased QD samples, an AC bias voltage can be applied. Due to the quantum confined Stark effect (QCSE), the absorption of a single QD can be electrically modulated with this bias voltage. A differential technique, which we called voltage

modulation (VM), can achieve background free measurement of the small linear absorption of a single QD approaching the shot noise limit (SNL).

In this chapter, VM is studied in the context of measuring the linear absorption of single biased IFQDs. First, the challenge and noise reduction techniques for measuring linear absorption of single QDs are introduced. Then, the Stark effect (SE) is explained in both classical and quantum mechanical pictures. Next, the QCSE in IFQDs is studied with a simple linear model and experimental measurements. At the end of the chapter the VM technique is discussed with a combination of theory, simulation, and experiments.

5.1 Noise reduction techniques for single QD absorption measurement

Usually, absorption is measured by comparing the intensity of a laser beam transmitted through a sample with the intensity of the incident laser beam. By scanning the wavelength, an absorption spectrum can be mapped out as a ratio of the absorbed light to the incident light over a wavelength range. Given all the kinds of noise in laser spectroscopy, the transmitted laser intensity is not a stable constant, but gives a strong background with random noise. Since this method measures absorption as the change on top of a noisy background (the transmitted laser beam), it only works for materials with relatively large absorption strengths compared with the noise in the transmitted laser beam, which is usually on the order of 10^{-2} to 10^{-3}. For a single QD with relatively small absorption strengths on the order of 10^{-3} or 10^{-4}, which is comparable or lower than the noise, a simple direct absorption measurement technique does not work due to the large noisy background. Even bandwidth reduced measurement techniques using laser intensity modulation as discussed in Chapter 4 may not work since the noise is at the same frequency as the signal. A few noise reduction techniques have been developed to extract the small absorption signal from a huge noisy background, including non resonant excitation DT, the noise eating technique, wavelength modulation, and voltage modulation.

With a non resonant excitation, the linear absorption dominates over nonlinear absorption. With the advantage of optical modulation and differential detection,

the linear absorption of single IFQDs has been measured with non resonant excitation DT [6]. However, this technique does not work for resonant excitation and the SNR is limited due to the limited efficiency of non resonant excitation.

The noise eating technique uses active feedback to control an intensity modulator to reduce common mode laser noise. Commercial noise eating devices are available, but the performance is limited due to the speed of the electronics, usually below MHz, and the precision of the feedback control. By using a low noise diode laser and a noise eater, linear absorption of a single IFQD has been measured [7].

Wavelength modulation is a differential detection technique used to reduce laser common mode noise by modulating the laser wavelength. It has been used to measure linear absorption of single QDs with a high SNR [8]. However, it requires laser wavelength modulation capability, which usually requires low modulation frequencies and may cause extra noise.

Voltage modulation is a differential detection technique used to reduce laser common mode noise by modulating the absorption of QDs through the QCSE. It has been used to measure linear absorption of SAQDs with a high SNR and fast measurement speed [9]. It will be discussed in detail later in this chapter. For a biased QD sample, VM provides an easy way to achieve a sensitive differential measurement of the small absorption strength from single QDs out of a noisy background.

5.2 Stark effect and quantum confined Stark effect

The Stark effect (SE) and quantum confined Stark effect (QCSE) are the underlying physics that allows VM to measure linear absorption with high SNR. In this section, first the SE is introduced with both classical and quantum mechanical pictures. Then the QCSE in IFQDs is studied with a simple linear model by experiments and numerical simulations.

5.2.1 Stark effect in atoms

The SE [10], the energy shifting or splitting of optical transitions under an external electric field, has been well studied for atoms and molecules. The SE has been widely used in Stark spectroscopy and laser spectroscopy. There are two types of SE, DC and AC [11]. Since the frequency of the applied voltage is much slower than the optical oscillation frequency, the SE studied here is a DC SE.

A simple classical picture for the SE is an energy shift of an electric dipole caused by an external electric field [12]. Dipole transitions in hydrogen atoms provide good examples. There are two different scenarios depending on whether the dipole is intrinsic or is externally induced by the applied electric field. When there is an initial electric dipole, for example, the 2s-2p dipole transition in a hydrogen atom, the effect of the external electric field on the dipole itself is small compared with the initial dipole and is negligible, as shown in Figure 5.1(a). The energy shift caused by the external electric field is proportional to the external electric field, which gives a linear SE as

$$\Delta U = -\vec{\mu} \bullet \vec{E} \tag{5-1}$$

where $\vec{\mu}$ is the dipole moment, and $\vec{E}$ is the external electric field.

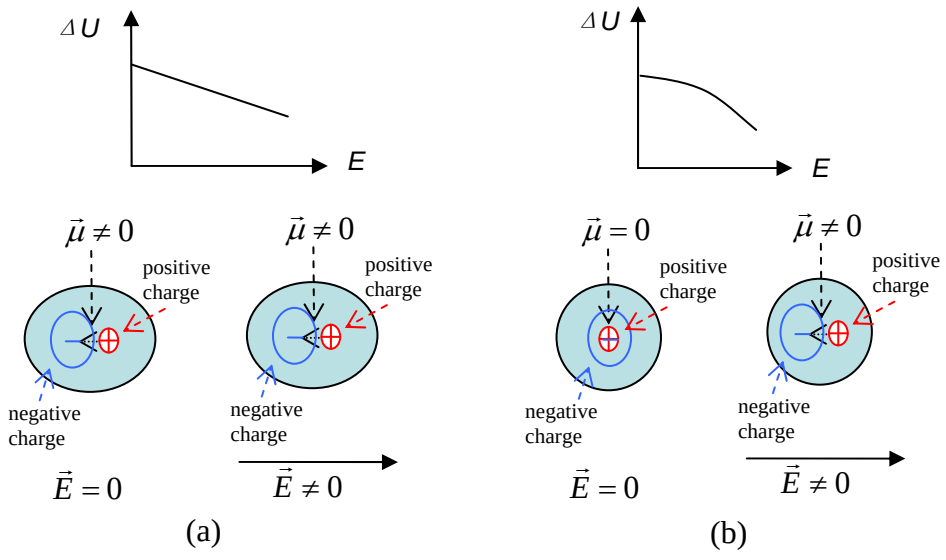

Figure 5.1 A classical picture of SE (a) linear SE (the initial dipole is not affected by the external electric field) (b) quadratic Stark effect (the external electric field induces a dipole)

When there is no initial dipole, the external electric field causes an induced electric dipole and to the lowest order of electric field gives a quadratic energy shift, as shown in Figure 5.1(b). Without any external electric field there is no initial electric dipole, for example the 1s state of the hydrogen atom. Under an external electric field, the positive charge and the negative charge get separated since they experience forces towards opposite directions. The external electric field produces an induced dipole with a direction opposite to the external electric field. The induced dipole interacts with the external electric field giving a quadratic Stark effect.

With a classical picture of a charge on a spring, the induced dipole moment can be estimated as:

$$m\omega^2 z_{eq} = eE \tag{5-2}$$

$$z_{eq} = \frac{eE}{m\omega^2} \tag{5-3}$$

$$\vec{D}_{induced} = \frac{e^2\vec{E}}{m\omega^2} \tag{5-4}$$

where m is the mass of the dipole, ω is the dipole oscillation frequency, z_{eq} is the equilibrium position, e is the charge of the dipole, and $\vec{D}_{induced}$ is the induced dipole moment.

The total energy is

$$\Delta U = \frac{1}{2}m\omega^2 {z_{eq}}^2 - \vec{D}\bullet\vec{E} = -\frac{1}{2}\frac{e^2}{m\omega^2}E^2 \tag{5-5}$$

The SE has been studied in quantum mechanics with a perturbation approach [12]. Usually the energy shift by the external electric field is much smaller compared to the transition energy so that the problem can be treated with perturbation theory.

The unperturbed system is

$$H_0\left|\phi_n^{(0)}\right\rangle = U_n^{(0)}\left|\phi_n^{(0)}\right\rangle \tag{5-6}$$

where H_0 is the Hamiltonian, $\left|\phi_n^{(0)}\right\rangle$ are the eigenstates, and $U_n^{(0)}$ are the eigenenergies for the unperturbed system.

With the external electric field as a weak perturbation the new Hamiltonian is

$$H = H_0 + V_{\text{int}} \tag{5-7}$$

$$V_{\text{int}} = -\vec{\mu}\bullet\vec{E} = -e\vec{r}\bullet\vec{E} \tag{5-8}$$

For hydrogen atoms, the solution to the first order perturbation is

$$U_{1s}{}^{(1)} = \langle\phi_{1s}|V_{\text{int}}|\phi_{1s}\rangle = e\vec{E}\bullet\langle\phi_{1s}|\vec{r}|\phi_{1s}\rangle = 0\,. \tag{5-9}$$

Any inversion symmetric wave function will give zero for first order energy shifts. The second order needs to be considered.

$$U_{1s}{}^{(2)} = \sum_{n',l',m'\neq 0,0,0} \frac{\left|\langle n',l',m'|V_{\text{int}}|\phi_{1s}\rangle\right|^2}{E_{1s}-E_{n'l'}} = \sum_{n',l',m'\neq 0,0,0} \frac{\left|\langle n',l',m'|\vec{D}|\phi_{1s}\rangle\bullet\vec{E}\right|^2}{E_{1s}-E_{n'l'}} = -\frac{9}{4}a_0{}^3E^2 \tag{5-10}$$

The induced dipole can be calculated for the 1s state.

$$\vec{D} = -e\langle\vec{r}\rangle = -e\left\langle\tilde{\phi}_{1s}\left|\hat{\vec{d}}\right|\tilde{\phi}_{1s}\right\rangle \tag{5-11}$$

$$\left|\tilde{\phi}_{1s}\right\rangle = \left|\phi_{1s}{}^{(0)}\right\rangle + \left|\phi_{1s}{}^{(1)}\right\rangle \tag{5-12}$$

$$\left|\phi_{1s}{}^{(1)}\right\rangle = eE\sum_{n'\neq 0}\frac{|n'00\rangle\langle n'10|\hat{z}|100\rangle}{E_{1s}-E_{n'p}} \tag{5-13}$$

To the lowest order, we get,

$$\left\langle\hat{\vec{D}}\right\rangle = 2e^2\sum_{n'\neq 0}\frac{\langle 100|\hat{z}|n'10\rangle\langle n'10|\hat{z}|100\rangle}{E_{n'p}-E_{1s}}E \tag{5-14}$$

For a degenerate system, for example, 2s and 2p states, the above simple nondegenerate perturbation theory cannot be used since the perturbation couples states to all orders. The Hamiltonian matrix needs to be rediagonized.

The matrix elements are

$$\langle 2l'm_l'|\hat{H}|2lm_l\rangle\,. \tag{5-15}$$

Due to the selection rules $l' = l \pm 1$ and $m_l' = m_l$, the non-vanishing matrix element is

$$\Delta U = \langle\phi_{2p0}|V_{\text{int}}|\phi_{2s}\rangle = e\vec{E}\bullet\langle\phi_{2p}|\hat{z}|\phi_{2s}\rangle = e\vec{E}\bullet\langle 210|\hat{z}|200\rangle = -3eEa_0\,. \tag{5-16}$$

The matrix is

$$\hat{H}_1 = \begin{pmatrix} 0 & \Delta U & 0 & 0 \\ \Delta U & 0 & 0 & 0 \\ 0 & 0 & 0 & 0 \\ 0 & 0 & 0 & 0 \end{pmatrix} \tag{5-17}$$

Rediagonizing the matrix we get

$$\hat{H}_1' = \begin{pmatrix} -\Delta U & 0 & 0 & 0 \\ 0 & \Delta U & 0 & 0 \\ 0 & 0 & 0 & 0 \\ 0 & 0 & 0 & 0 \end{pmatrix}. \tag{5-18}$$

$$\begin{aligned} |\lambda_+\rangle &= \frac{1}{\sqrt{2}}(|200\rangle + |210\rangle) \\ |\lambda_-\rangle &= \frac{1}{\sqrt{2}}(|200\rangle - |210\rangle) \end{aligned} \tag{5-19}$$

$$\begin{aligned} U_- &= U_2^{(0)} - \Delta U = -\frac{e^2}{8a_0} - 3eEa_0 \\ U_+ &= U_2^{(0)} + \Delta U = -\frac{e^2}{8a_0} + 3eEa_0 \end{aligned} \tag{5-20}$$

The quantum description gives similar results as the classical picture for the linear and quadratic Stark effects, which have been experimentally observed in the hydrogen atom.

5.2.2 Quantum confined Stark effect in QDs

QDs, as artificial atoms, have similar properties as atoms. Similarly to atoms, optical transitions of excitons and trions in QDs are affected by external electric fields through the QCSE. In Chapter 4 we have seen the voltage dependence of PL and DR for both ensembles of and single QDs, which is known as the QCSE in semiconductor heterostructures. In this section the theory and experimental measurement of QCSE in IFQDs will be discussed.

The QCSE is the Stark effect of bound excitons in semiconductor heterostructures, enhanced by the quantum confinement caused by materials with different bandgaps [13-15]. Due to the strong quantum confinement, a weak external electric field will pull the electron-hole pairs of the exciton toward

opposite directions but will still allow them to remain bound. With a small voltage change the transition energy changes dramatically. The QCSE in quantum wells (QWs) has been well studied and widely applied in optical modulators for optical communication with high efficiency, low voltage, and fast speed [13, 16]. QCSE has also been studied in QDs [17-19]. ZnCd QDs show a strong quadratic QCSE at room temperature, and excitons/trions in SAQDs show a linear QCSE.

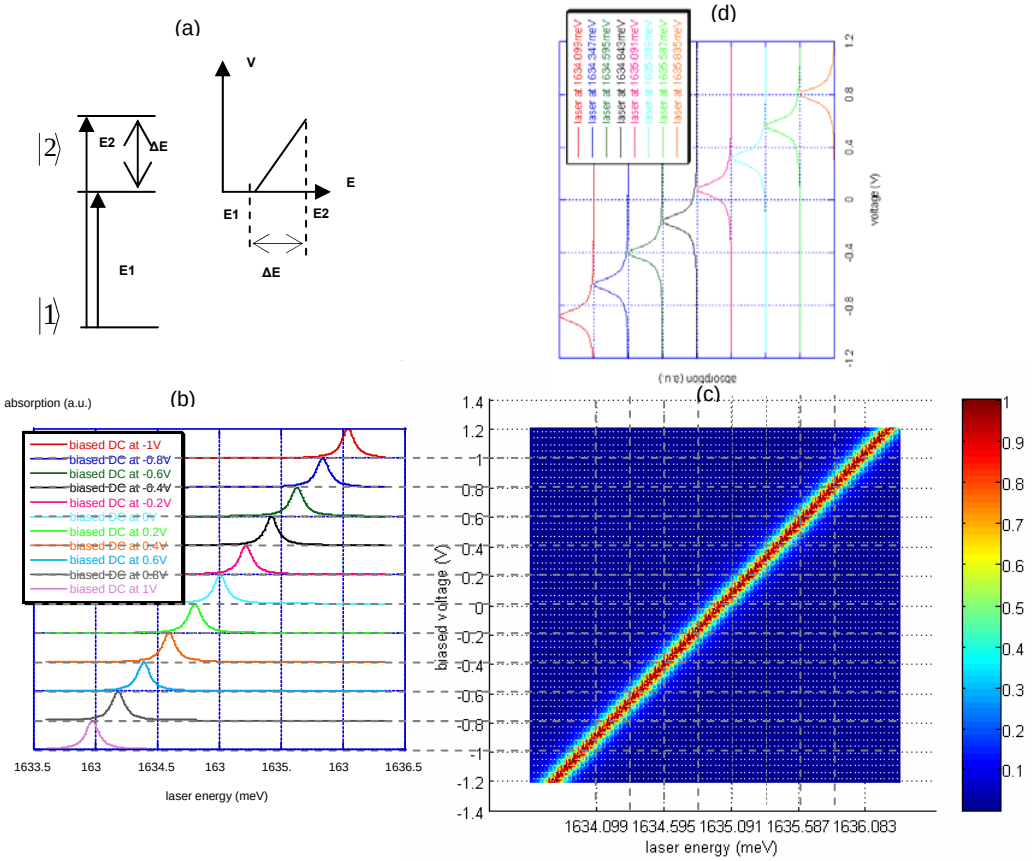

Figure 5.2 Simulation of QCSE of a single QD with a Lorentzian line shape (a) a linear QCSE model (b) voltage dependent absorption over laser energy (c) voltage-energy absorption map (d) laser energy dependent absorption over voltage

The simplest model is a linear QCSE model, which assumes the energy shift is linear in the external electric field while the absorption lineshape and strength are not affected by the external electric field. The SE coefficient is defined as the

ratio between the energy shift and the bias voltage. From the two-level model discussed in Chapter 4 we learned that the linear absorption of excitons/trions in QDs has a Lorentzian shape. With a simple Lorentzian line shape model, Figure 5.2 illustrates the QCSE of a single QD with a simple linear shift. Figure 5.2(a) illustrates that the energy of the dipole transition shifts linearly with the applied voltage, causing a linear shift of the peak of the Lorentzian shaped absorption under the applied voltage. The QCSE provides a voltage dependent absorption map over laser energy for a single QD, illustrated by multiple absorption lines artificially shifted vertically for clarity as shown in Figure 5.2(b), and a three dimensional pseudocolor map of the voltage-energy absorption map $\alpha(V,\lambda)$ as shown in Figure 5.2(c). It is worth pointing out that the voltage dependent absorption map can also be viewed as a laser energy dependent absorption map over voltage as shown in Figure 5.2(d), which indicates that the same information can be obtained equivalently by measuring absorption over voltage at different wavelengths. This is exactly the basis for the VM technique to be discussed later in this chapter.

This simple linear QCSE model is based on ideal QDs with strong quantum confinement. It works well under the perturbation approximation for strongly confined QDs in a small voltage range where the external electric field is much weaker than the quantum confinement, as shown in Figure 4.10. This model does not work well when the perturbation assumption is not valid, which appeared in some IFQDs to be discussed next. However, a more complicated QCSE can be numerically modeled based on this linear QCSE model with varying SE coefficients, as we will see in the following discussion. The linear QCSE was experimentally observed in Figure 4.10 for both ensembles of and single QDs. For ensembles of QDs in the low and high energy monolayer, the QCSE is linear and the coefficient is similar for both layers. A linear QCSE has also been observed in single SAQDs [9].

However, the QCSE can be more complicated than this simple linear model. Figure 5.3(a) shows the nonlinear absorption measured with DR for another single QD under different bias voltages. Compared with the simple model in Figure 5.2,

there are a few complications. First, the SE coefficient is not a constant and it changes at different voltage ranges. Second, the strength of the DR changes at different biased voltages. The DR signal is strong in the voltage range -0.6V to +0.6V, and it gets weak in the voltage range -0.6V to -0.8V and 0.6V to 0.8V. It disappears in the voltage -0.8V to -1V and 0.8V to 1V. Third, the line shape of the DR signal changes with bias voltage. It is symmetric and narrow in the voltage -0.4V to 0.6V. It gets asymmetric and the width broadens in the voltage -0.6V to -1V.

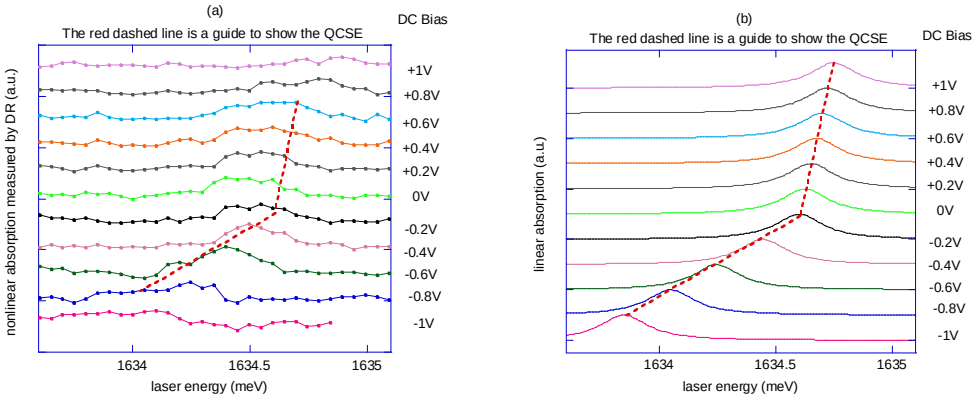

Figure 5.3 Quantum confined Stark effect in a single IFQD (a) nonlinear absorption measured by DR (b) simulated linear absorption

These complications could be caused by a few sources. One problem is that the quantum confinement in IFQDs may be weak enough for electrons confined in QDs to tunnel out of the QDs under a certain applied bias range. We have observed that leakage current in these samples increases with a high bias voltage. Another problem is that a local electric field with bias dependence may exist in the sample. Due to the sample structure and strain there may be a different local electric field at each QD, which means the actual electric field on a QD is the combination of the local electric field and the applied electric field from the bias voltage. The local electric field may change under different bias voltages. It has been observed that the bias voltage range and SE coefficients of the QCSE vary for different QDs on same sample.

To understand the physics, this complicated QCSE is simulated numerically using a linear SE model with strong and weak QCSE regimes, as shown as voltage dependent linear absorption curves in Figure 5.3(b). In the voltage range from -1V to -0.2V, there is a strong QCSE with a large SE coefficient of about 1meV/V. In the voltage range from -0.2V to 1V, there is a weak QCSE with a small SE coefficient of about 0.125meV/V. The underlying physics for the strong and weak SE could be a quadratic QCSE or a bias voltage dependent local field effect, which need further study. This phenomenological model will be used later to qualitatively explain the measured VM signals. More complications like line shape broadening and absorption strength change caused by the bias voltage are not considered. Using a high resolution laser wavelength scan and small steps in voltage, a more precise voltage-energy absorption map can be obtained experimentally. However, due to the extra noise and time caused by the laser wavelength scan, this approach to obtain the absorption map is slow and would not work for SAQDs with much weaker absorption strength. Next, we will show how VM overcomes these difficulties to obtain the same absorption map faster and with much higher SNR.

5.3 Voltage modulation

With the QCSE demonstrated in DR measurements, background-free measurements of the linear absorption of a single IFQD are achieved through VM. In this section, first the physics of VM is explained to illustrate how the background is cancelled to improve SNR. Then the linear absorption of a single IFQD is measured with the VM technique and the results are compared with the DR measurements.

5.3.1 Theory of voltage modulation

The experimental setup and the physics of VM are illustrated in Figure 5.4. Figure 5.4(a) shows the experimental setup. Reflection geometry is used since our biased IFQD sample does not allow the laser beam at the QD absorption wavelength to be transmitted. One laser beam is focused onto a small aperture and

interacts with QDs. Backscattered light is collected by a beam splitter and focused onto a photo detector. The voltage applied on the sample is DC with a small square wave AC component. The differential absorption is measured by a lock-in amplifier at the voltage modulation frequency. The AC voltage is fixed and the DC voltage is scanned over a range to map out the absorption as a function of voltage. The laser wavelength is fixed in each voltage scan and the voltage-energy absorption map is obtained by scanning the voltage at different laser wavelengths.

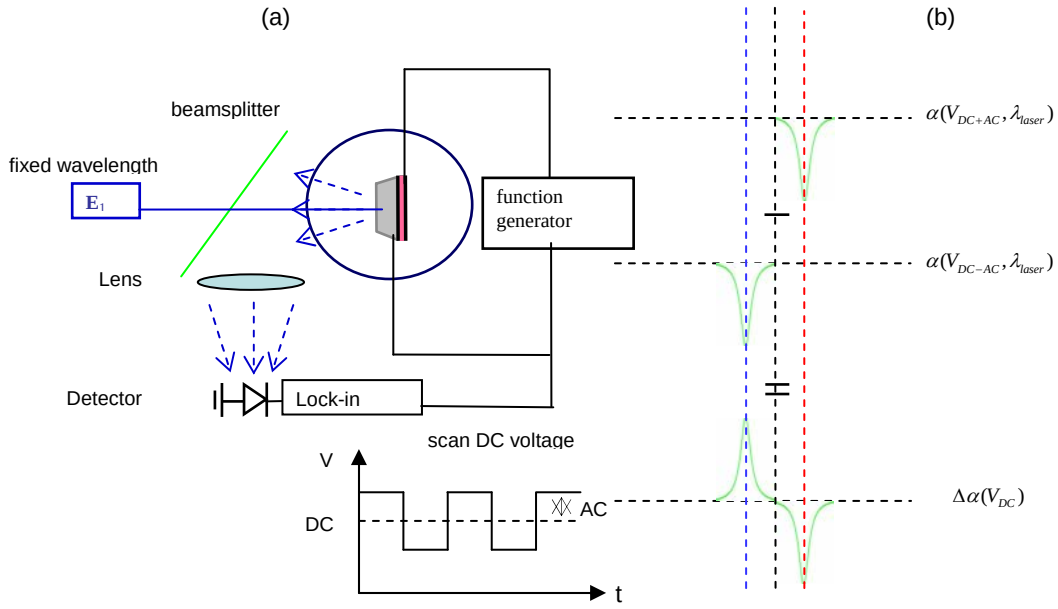

Figure 5.4 Voltage modulation (a) experimental setup and (b) VM physics

Figure 5.4(b) illustrates the physics of the VM technique. With a voltage-energy absorption map, the Lorentzian shaped absorption peaks appear at different wavelengths depending on the bias voltage. With a square wave modulation, the bias voltage on the sample is switched between DC+AC and DC-AC at the voltage modulation frequency for each DC voltage. Due to the QCSE, the absorption curve is modulated by the bias voltage, which means the absorption peak jumps at the voltage modulation frequency. The lock-in amplifier picks up the differential absorption (VM signal) $\Delta\alpha(V_{DC})$, featuring a peak, center zero, and dip. The peak of the VM signal occurs at the DC voltage where

$\alpha(V_{DC+AC}, \lambda_{laser})$ reaches the maximum. The dip of the VM signal occurs at the DC voltage where $\alpha(V_{DC-AC}, \lambda_{laser})$ reaches the maximum. The center zero corresponds to the DC voltage where $\alpha(V_{DC+AC}, \lambda_{laser})$ and $\alpha(V_{DC-AC}, \lambda_{laser})$ are equal.

The exact VM signal can be obtained by analyzing the signal on the photo detector. For each DC voltage, the intensity of the transmitted laser beam on the detector corresponding to the two modulation voltages can be represented as

$$I(V_{DC+AC}) = I_0\left[1-\alpha(V_{DC+AC}, \lambda_{laser})\right], \tag{5-21}$$

$$I(V_{DC-AC}) = I_0\left[1-\alpha(V_{DC-AC}, \lambda_{laser})\right]. \tag{5-22}$$

The absorption change caused by the voltage modulation is

$$\Delta\alpha(V_{DC}) = \alpha(V_{DC+AC}, \lambda_{laser}) - \alpha(V_{DC-AC}, \lambda_{laser}). \tag{5-23}$$

The time domain signal measured by the detector is

$$I(t) = I_0\left[1-\alpha(V_{DC-AC}, \lambda_{laser}) + \Delta\alpha(V_{DC})\bullet square(f_0 t)\right]. \tag{5-24}$$

The Fourier series of the square wave is the odd orders of harmonics with the first order dominant.

$$square(f_0 t) = \frac{4}{\pi}\sum_{n=1,3,\ldots}^{\infty}\frac{1}{n}\sin(2\pi n f_0 t) \tag{5-25}$$

We get

$$I(t) = I_0\left[1-\alpha(V_{DC-AC}, \lambda_{laser}) + \Delta\alpha(V_{DC})\bullet\frac{4}{\pi}\sum_{n=1,3,\ldots}^{\infty}\frac{1}{n}\sin(2\pi n f_0 t)\right]. \tag{5-26}$$

In the frequency domain, the background transmitted beam will be at DC, and the absorption change caused by the VM will appear at the voltage modulation frequency.

$$I(f = f_0) = \frac{4}{\pi} I_0 \Delta\alpha(V_{DC})\sin(2\pi f_0 t) \tag{5-27}$$

With a lock-in amplifier at the voltage modulation frequency, the linear absorption signal can be separated from the noisy background transmitted beam for a background free detection. All the background noise except the laser noise at

the modulation frequency is automatically cancelled out with the differential technique.

Depending on the amplitude of the AC voltage compared with the voltage corresponding to the absorption line width, VM may give a derivative line shape or recover the original absorption line shape. Here we assume a simple Lorentzian line shape for a QD based on Equation (4-15), so that the absorption peaks at the voltages DC+AC and DC-AC are

$$\alpha(V_{DC+AC}, \lambda_{laser}) = \alpha_0 \frac{\gamma}{\gamma^2 + (\Delta + \delta)^2} \tag{5-28}$$

$$\alpha(V_{DC-AC}, \lambda_{laser}) = \alpha_0 \frac{\gamma}{\gamma^2 + (\Delta - \delta)^2} \tag{5-29}$$

$$\Delta = \lambda_{laser} - \beta V_{DC} \tag{5-30}$$

where α_0 is the absorption of the QD, γ is the coherence decay rate, Δ is the detuning corresponding to the DC voltage, δ is the detuning corresponding to the AC amplitude, λ_{laser} is the laser wavelength, β is the SE coefficient, and V_{DC} is the DC voltage.

The difference of the two absorptions gives the VM signal as

$$\Delta\alpha(V_{DC}) = \alpha_0 \left(\frac{\gamma}{\gamma^2 + (\Delta + \delta)^2} - \frac{\gamma}{\gamma^2 + (\Delta - \delta)^2} \right). \tag{5-31}$$

For small AC amplitude, $\delta \ll \Delta$, the differential absorption is simplified as

$$\Delta\alpha(V_{DC}) = \alpha_0 \frac{4\gamma\Delta\delta}{(\gamma^2 + \Delta^2)^2}. \tag{5-32}$$

VM may give a derivative line shape or recover the original absorption line shape, depending on the AC amplitude. Figure 5.5 shows the simulation of the AC amplitude dependence of the VM signal. Figure 5.5(a) is a pseudocolor map showing the VM signal when the AC amplitude changes from 0 to 0.4V, and Figure 5.5(b) is a vertically shifted plot of the VM signal when the AC amplitude is 0.05V, 0.1V, 0.2V, and 0.3V. When the AC amplitude increases, the peak position shifts linearly in the AC amplitude. With a small AC voltage, 0.05V, corresponding to an energy shift smaller than the absorption line width, VM gives a derivative line shape due to the overlap of the two absorption peaks

$\alpha(V_{DC+AC}, \lambda_{laser})$ and $\alpha(V_{DC-AC}, \lambda_{laser})$. With a large AC voltage, 0.3V, corresponding to an energy shift larger than the absorption line width, VM recovers the original absorption line shape due to the complete separation of the two absorption peaks. Ideally, large AC VM is preferred, but small AC VM is more frequently used for two practical reasons. One reason is that small AC VM avoids interacting with other nearby states. Usually it is very hard to find only one clean state without any other states close in energy even in a small aperture. Large AC VM may give a strange line shape which requires extra effort to explain. Small AC VM provides a smaller but symmetric signal which is easier to explain. Another reason to avoid large AC VM is that a large AC voltage may affect the absorption line shape and strength, which complicates the data interpretation.

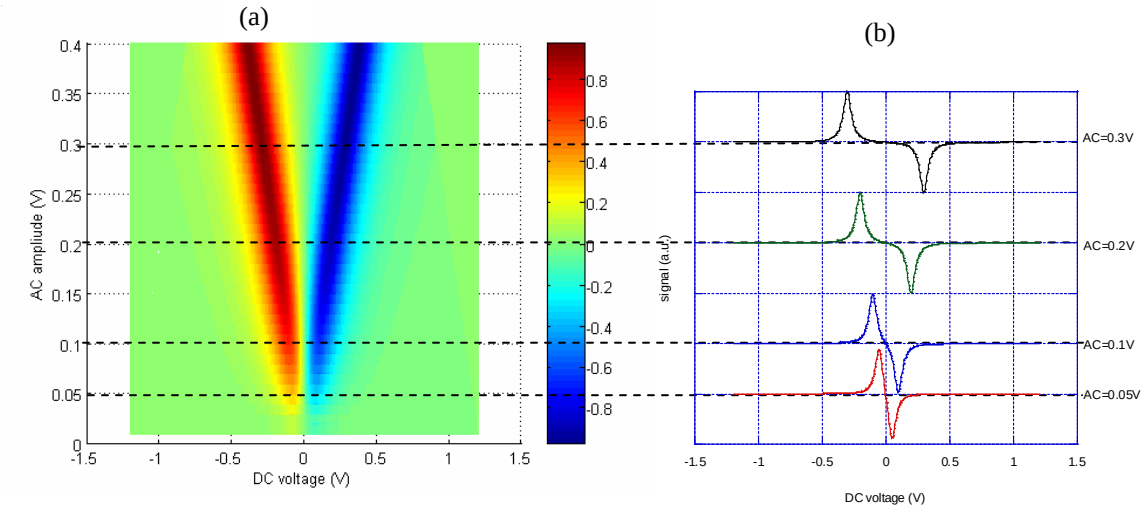

Figure 5.5 Simulation of the AC amplitude dependence of the VM signal (a) pseudocolor map for AC amplitude between 0 and 0.4V (b) vertically shifted VM signal for AC amplitude of 0.05V, 0.1V, 0.2V, and 0.3V

For a fixed AC modulation, when the laser energy changes, the VM signal remains the same shape and shifts in DC voltage, as shown in Figure 5.6 by simulation. With a small AC amplitude, Figure 5.6(a) illustrates the laser energy dependence of the VM signal in the laser energy range 1634.3-1634.9meV with a three dimensional pseudocolor map, and Figure 5.6(b) shows the derivative VM

signal at three different laser energies. When the laser energy moves to a higher energy, the derivative VM signal retains the same line shape, but shifts to a higher voltage, agreeing with the QCSE shown in Figure 5.2. The best laser energy for VM is the wavelength corresponding to the center of the voltage range where the linear QCSE approximation is effective.

It is worth pointing out that the voltage-energy VM map contains the same information as the voltage–energy absorption map. The voltage-energy absorption map can be constructed from a voltage-energy VM map. The VM technique is important for SAQDs with small absorption strengths which are hard to measure by DT/DR, but easier to measure with VM. With a small AC voltage VM, the relative absorption map can be recovered. With a large AC voltage VM, the absolute absorption map can be easily recovered from the VM map. This is important when the absorption is too small to measure except with VM.

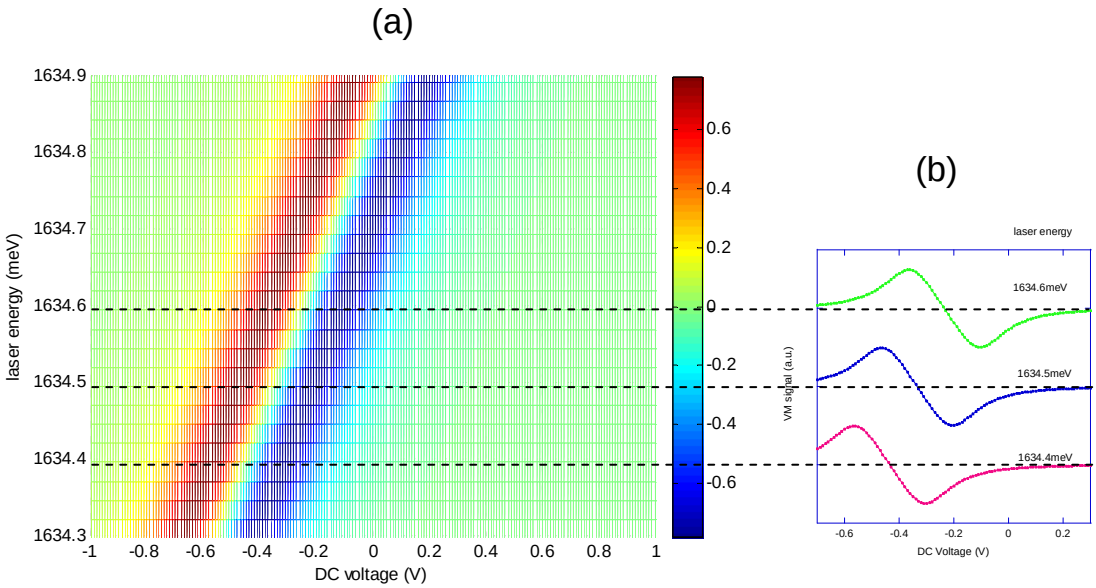

Figure 5.6 Simulation of laser energy dependence of the VM signal (a) pseudocolor map for the laser energy range 1634.2-1635.1meV (b) vertically shifted VM signal for laser energies of 1634.4, 1634.5, and 1634.6meV

5.3.2 QD absorption measured by voltage modulation

With the QCSE we observed in Figure 5.4, we measured the VM signal of the same QD at three different laser energies, shown in Figure 5.7(a). At the laser

energies 1634.4meV and 1634.5meV, the VM signal has a derivative line shape, but the dip has a smaller width and height than the peak. At the laser energy 1634.6meV, the peak shifts to a higher voltage with same width and height, but the dip vanishes. The peak of the measured VM signal has same laser energy dependence as Figure 5.6, with the VM signal peak moving to a higher voltage when the laser energy increases. However, the data indicates that the dip gets inhibited when the laser energy increases. This is different from the simple linear QCSE VM signal in Figure 5.6, but it agrees with the complications of the QCSE of the QD as shown in Figure 5.4(a), which shows a strong QCSE in the voltage range -1V to -0.4V and a weak QCSE in the voltage range -0.4V to 0.6V with a turning point around the bias voltage -0.4V and laser energy 1634.6meV. At the laser energies 1634.4meV and 1634.5meV, which are below the turning point, strong QCSE dominates, which gives a derivative line shape showing a peak and a dip, with the dip slightly inhibited due to the effect of weak QCSE. At the laser energy 1634.6meV, which is at the turning point, the peak is in the strong QCSE regime, and the dip falls into the weak QCSE regime. As a result the peak is strong but the dip is strongly inhibited.

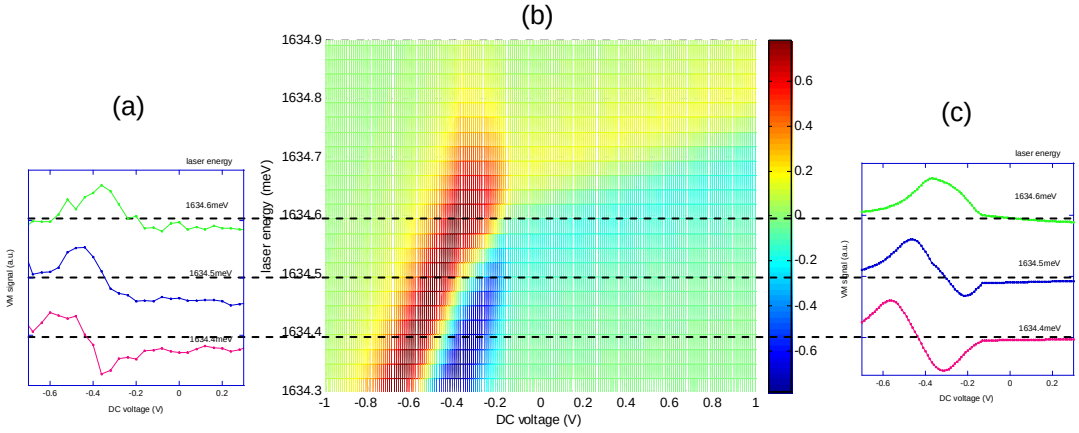

Figure 5.7 VM signal laser energy dependence by measurement and simulation with AC amplitude of 0.3V. (a) measured VM signal at three laser energies (b) simulated pseudocolor map of VM in the laser energy range (c) simulated VM signal at the same laser energies

To support the above qualitative explanation, we calculated the VM signal quantitatively with the simulated voltage-energy absorption map shown in Figure 5.3(b), which takes into account a strong QCSE in the voltage range -1V to -0.2V and a weak QCSE in the -0.2V to 1V voltage range. The simulated VM signals for the laser energy range 1643.3meV to 1643.9meV are shown as a pseudocolor map in Figure 5.7(b), and the VM signals at the three specific laser energies 1643.4, 1634.5 and 1634.6meV are shown in Figure 5.7(c). The pseudocolor map shows that strong QCSE gives a strong VM signal in the regime below and to the left of (-0.2V, 1634.68meV) and that weak QCSE gives a weak VM signal in the regime above and to the right of (-0.2V, 1634.68meV). The peak of the large VM signal goes beyond the QCSE turning laser energy of 1634.6meV, maintaining the same height and width. The dip of the large VM signal vanishes by reducing in depth and width when the laser energy approaches the QCSE turning point. The three separate VM signals from simulation show reasonable agreement with the measured VM signals. Some discrepancy between the simulation and the measurement could be caused by more complex aspects of the QCSE, such as effects of the bias voltage on the lineshape and signal strength, which are not considered in the simulation.

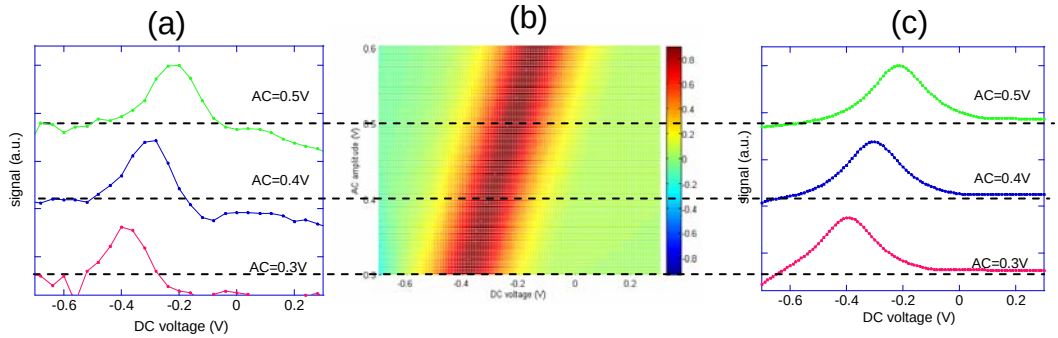

Figure 5.8 VM signal AC amplitude dependence by measurement and simulation with the laser energy at 1634.22meV. (a) Measured VM signal at three AC amplitudes. (b) Simulated pseudocolor map of VM in the AC amplitude range. (c) Simulated VM signal at the same AC amplitudes

For the same QD, VM signals at three different AC amplitudes of 0.3V, 0.4V and 0.5V are measured for laser energy at 1634.22meV, as shown in Figure 5.8(a). Only the dip of the VM signal, measured as a peak due to a 180 degree phase offset on the lockin amplifier, is measured due to the limited voltage range in which the strong QCSE exits. For the same reason, only VM signals in the AC voltage range of 0.3V to 0.5V are obtained, corresponding to large AC VM since the energy shift caused by the AC voltage is larger than the energy corresponding to the absorption linewidth. As expected, when the AC amplitude increases, the VM signal remains a Lorentzian shape and shifts linearly to the more positive DC voltage side. With the same simulated voltage-energy absorption map shown in Figure 5.3(b), the AC amplitude dependence of the VM signal is calculated, shown in Figure 5.8(b) as a pseudocolor map, and in Figure 5.8(c) as vertically shifted plots for the same AC amplitudes as in Figure 5.8(a). The simulated results gave the same AC amplitude dependence as the measurement, except that the measured VM signals showed a non zero background due complications from the QCSE in the QD as we discussed in Section 5.2.2.

Here we simulated a voltage-laser wavelength dependent absorption map to calculate the VM map. With a measured voltage-laser wavelength dependent VM map, we can construct the absorption map by calculation. For SAQDs with weak absorptions, VM provides an efficient way to obtain a voltage-energy absorption map that is hard to obtain with other techniques.

5.3.3 Advantages of voltage modulation

Modulating the bias voltage on a QD sample through the QCSE provides a new dimension of control in laser spectroscopy for QDs. Using this new capability, VM measures the linear absorption of single QDs with less noise and higher speed. The ratio between the signal and DC voltage on the detector for the single QD VM signal is about 2×10^{-4}, which is comparable with the ratio between the size of a IFQD (estimated to be 40nm) and the aperture (estimated to be 2μm). In this section, VM is compared with its variations and other techniques to illustrate its advantages and disadvantages.

Due to the correspondence between the bias voltage and the energy of the state, there are two ways to obtain the voltage-energy VM map. One way is to scan the voltage, another is to scan laser wavelength. The voltage-energy VM map can be obtained equally by either a voltage scan over a wavelength range or a laser wavelength scan over a voltage range.

Ideally it is preferred to scan laser wavelength rather than voltage because there could be complicated QCSE-related effects as we saw in Figure 5.5. Although the laser wavelength scan has the advantage of direct mapping, the laser wavelength scan capability may be limited by available lasers, resolution, and stability. VM requires a wavelength-stable CW laser with a narrow line width compared with the absorption line of the QDs, which is in the order of GHz. Usually narrow linewidth tunable lasers with fine resolution wavelength scanning capabilities are hard to obtain or very expensive compared with those without wavelength scanning capabilities. Even for the narrow line width lasers with fine resolution wavelength scanning capabilities, the mode hop free wavelength scanning range is very limited. There is always more laser noise when the laser wavelength is scanned compared to wavelength stabilized operation since scanning the laser wavelength involves altering the laser cavity.

The voltage scan has the disadvantage of indirectly mapping the absorption, but the advantages of ease of use and speed. The voltage scan is always available for biased samples. Since the voltage can be tuned with high resolution, it is easy to obtain high resolution absorption spectra. Also voltage scans can be very fast since the voltage can be ramped quickly over a large range without worrying about slow laser cavity response time or a small mode hope free wavelength scanning range, which limits the speed of wavelength scans.

VM and WM use similar differential techniques, but there are still a few significant differences between VM and WM. WM requires the capability of modulating laser wavelength, preferably at high frequency to account for 1/f noise. Modulation of the laser frequency is usually slow (<KHz) because mode hop free wavelength tuning requires precise laser cavity changes. Also, laser wavelength tuning adds noise compared to fixed wavelength operation. Actually, low noise

lasers with external reference cavities require that the laser wavelength be fixed and the reference cavity be only slowly tuned. Finally, lasers with wavelength modulation capabilities are much less common and more expensive than those without wavelength modulation capabilities. The WM modulation has the advantage of reliable wavelength information, and the disadvantage of low SNR and expense.

VM only requires a low noise wavelength tunable laser, which is cheaper and less noisy than a wavelength modulated one. VM can go to much higher modulation frequencies to get better SNR. VM also can achieve much finer resolution than WM due to the greater availability of high precision voltage control over high precision wavelength control. VM has the advantage of high SNR, cheaper lasers and the disadvantage of more complicated data interpretation.

As discussed in Chapter 4, laser intensity modulation has the advantage of shifting measurement frequency to a high frequency to reduce noise, but a good portion of the dominate 1/f noise near DC is also carried to the high frequency. DT/DR is always limited by the 1/f noise near DC and it can not reach SNL due to this fundamental limitation, which is why fast measurement at a time scale comparable to the bandwidth helps to reduce the common mode noise in DT/DR. Compared with DT/DR, VM has the advantage of shifting measurement frequency to a high frequency without being affected by the dominant 1/f noise near DC, which enables VM to reach SNL. VM gives much higher SNR than DT/DR.

The VM gives larger signal strength than DR due to that its modulation scheme is more efficient than DT/DR. In VM the majority (>90%) of the signal is at the modulation frequency. In DR, only a small portion (about 1/8) is at the difference frequency.

The absorption of QDs can be studied by either VM or DT/DR. For biased QDs samples, the voltage-energy absorption map of a single QD can be constructed either through DR or VM. In the laser spectroscopy studies of QDs, signal strength and SNR become important due to the weak absorption of SAQD. Comparing VM and DR signals in IFQDs, the absorption measured with VM

gives a bigger signal and higher SNR than the nonlinear absorption signal measured with DR. Similar results have been obtained with SAQDs. The high SNR gained by VM enabled further study on SAQDs demonstrating optical pumping, the Mollow triplet and the Autler-Townes splitting, which would have been impossible with DT/DR [20, 21].

In summary, measurement of the linear absorption of a single QD is challenging due to the fact that the signal exists at the same frequency as a noisy background. Noise reduced techniques were studied to measure the single QD absorption with high SNR by shifting the small signal away from the noisy background through VM. The physics and setup of VM were discussed to illustrate its advantages and disadvantages. VM achieves linear absorption of single IFQDs that agrees with the nonlinear absorption measured with DR, but with a higher acquisition speed and SNR.

Bibliography

[1] R. J. Warburton, C. SchÃ¤flein, D. Haft, F. Bickel, A. Lorke, K. Karrai, J. M. Garcia, W. Schoenfeld, P. M. Petroff, Optical emission from a charge-tunable quantum ring, Nature 405, 926 (2000).

[2] A. Högele, S. Seidl, M. Kroner, K. Karrai, R. J. Warburton, B. D. Gerardot, P. M. Petroff, Voltage-Controlled Optics of a Quantum Dot, Phys. Rev. Lett. 93, 217401 (2004).

[3] A. S. Bracker, E. A. Stinaff, D. Gammon, M. E. Ware, J. G. Tischler, A. Shabaev, Al. L. Efros, D. Park, D. Gershoni, V. L. Korenev, I. A. Merkulov, Optical Pumping of the Electronic and Nuclear Spin of Single Charge-Tunable Quantum Dots, Phys. Rev. Lett. 94, 047402 (2005).

[4] M. Atatüre, J. Dreiser, A. Badolato, A. Högele, K. Karrai, A. Imamoglu, Quantum-Dot Spin-State Preparation with Near-Unity Fidelity, Science 312, 551 (2006).

[5] M. Atature, J. Dreiser, A. Badolato, A. Imamoglu, Observation of Faraday rotation from a single confined spin, Nature Physics 3, 101 (2007)

[6] N. H. Bonadeo, A. S. Lenihan, G. Chen, J. R. Guest, D. G. Steel, D. Gammon, D. S. Katzer, D. Park, Single quantum dot states measured by optical modulation spectroscopy, Appl. Phys. Lett., 75, 2933 (1999).

[7] J. R. Guest, T. H. Stievater, X. Li, J. Cheng, D. G. Steel, D. Gammon, D. S. Katzer, D. Park, C. Ell, A. Thranhardt, G. Khitrova, H. M. Gibbs, Measurement of optical absorption by a single quantum dot exciton, Phys. Rev. B, 65, 241310 (2002).

[8] T. H. Stievater, X. Li, J. R. Guest, D. G. Steel, D. Gammon, D. S. Katzer, D. Park, Wavelength modulation spectroscopy of single quantum dots, Appl. Phys. Lett., 80, 1876 (2002).

[9] B. Alén, F. Bickel, K. Karrai, R. J. Warburton, P. M. Petroff, Stark-shift modulation absorption spectroscopy of single quantum dots, Appl. Phys. Lett. 83, 2235 (2003).

[10] J. Stark, Observations of the effect of the electric field on spectral lines I. Transverse effect, Annalen der Physik, 43, 965 (1914).

[11] S. H. Autler and C. H. Townes, Stark Effect in Rapidly Varying Fields, Phys. Rev. 100, 703 (1955).

[12] R. Robinett, Quantum Mechanics, Oxford University Press, 1997.

[13] D. A. B. Miller, D. S. Chemla, T. C. Damen, A. C. Gossard, W. Wiegmann, T. H. Wood, and C. A. Burrus, Band-Edge Electroabsorption in Quantum Well Structures: The Quantum-Confined Stark Effect, Phys. Rev. Lett. 53, 2173 (1984).

[14] D. Alderighi, M. Zamfirescu, A. Vinattieri, M. Gurioli, S. Sanguinetti, M. Povolotskyi, J. Gleize, A. D. Carlo, P. Lugli, and R. Nötzel, Dynamical nonlinearity in strained InGaAs (311)A sidewall quantum wires, Appl. Phys. Lett. 84, 786 (2004).

[15] R. M. Macfarlane, Optical Stark spectroscopy of solids, Journal of Luminescence, 125, 156 (2007).

[16] Y. Kuo, Y. K. Lee, Y. Ge, S. Ren, J. E. Roth, T. I. Kamins, D. A. B. Miller, J. S. Harris, Strong quantum-confined Stark effect in germanium quantum-well structures on silicon, Nature 437, 1334 (2005).
[17] S. A. Empedocles, M. G. Bawendi, Quantum-Confined Stark Effect in Single CdSe Nanocrystallite Quantum Dots, Science 278, 2114 (1997).
[18] J. Seufert, M. Obert, M. Scheibner, N. A. Gippius, G. Bacher, A. Forchel, T. Passow, K. Leonardi, D. Hommel, Stark effect and polarizability in a single CdSe/ZnSe quantum dot, Appl. Phys. Lett. 79, 1033 (2001).
[19] M.S. Skolnick, D. J. Mowbray, Self-assembled semiconductor quantum dots: Fundamental physics and device applications, Annual Review of Materials Research, 34, 181 (2004).
[20] X. Xu,, Y. Wu, B. Sun, Q. Huang, J. Cheng, D. G. Steel, A. S. Bracker, D. Gammon, C. Emary, L. J. Sham, Fast Spin State Initialization in a Singly Charged InAs-GaAs Quantum Dot by Optical Cooling, Phys. Rev. Lett. 99, 097401 (2007).
[21] X. Xu, B. Sun, P. R. Berman, D. G. Steel, A. S. Bracker, D. Gammon, L. J. Sham, Coherent Optical Spectroscopy of a Strongly Driven Quantum Dot, Science, 317, 929 (2007).

Chapter 6

Spin Noise

The various kinds of noise discussed in Chapter 3 always exist in laser spectroscopy experiments. Usually, such noise can cause random fluctuations of physical variables, which may add difficulty to the signal measurement process. It is often desirable to minimize the random fluctuating noise to improve signal measurements. However, noise is not always useless. Sometimes the noise, if carefully measured, can provide useful information about a given physical system. For example, Johnson noise, the thermal noise of electronics has been measured to monitor the temperature [1]. Another example is that of spin noise [2,3,4], which yields physical properties of spin systems, as discussed in this chapter.

The chapter starts with an introduction of spin with a focus on its quantum properties. Then the physics of spin noise is explored to understand its physical origin and properties. After that, spin noise measurement techniques and the physics behind the measurement are explained. At the end of this chapter, experimental measurements of the spin noise at different magnetic fields are presented and discussed.

6.1 Properties of spin

Spin is an intrinsic quantum property of elementary particles that build up all matter, and it is a fundamental measurable quantity independent of all other properties like charge and mass. Spin has been studied for various applications

like magnetic resonance imaging (MRI) [5], quantum computing [6,7], and spintronics [8,9].

The definition of classical spin comes from the physical rotation of a particle. Therefore, it is tempting to apply this idea to the quantum spin of elementary particles, where the spin is caused by the rotation of a charged particle. But the spin of a subatomic particle is not from the rotation of the charge in the particle. For example, if the spin of an electron were from the fast rotation of the electron, then the speed of the rotation would be faster than the speed of light, which contradicts the theory of relativity. To understand the properties related to the spin, it has to be assumed that spin is an intrinsic property independent of any other properties of subatomic particles.

Spin is a quantum character rather than a classical one. In the limit of $\hbar \to 0$, the quantity of spin vanishes. Spin is measured through its projection along a certain direction. Along any direction, the measured spin angular momentum is quantized with discrete values. For example, an electron spin angular momentum can be only $\pm\frac{1}{2}\hbar$, and is thus called a spin $\frac{1}{2}$ system. Photon spin can be $\pm 1\hbar$, and a spin 1 system. Spin may be represented as a spin vector with three spin angular momentum along the x, y, z directions. But unlike a classical angular momentum vector, different spin angular momentum cannot be measured simultaneously due to the uncertainty principle. For example, if the spin angular momentum along the z direction is measured precisely, then the spin angular momentum along the x, y directions measured at the same time will have some uncertainty.

For a spin $\frac{1}{2}$ system the eigenstates of the spin are the spin up state with the spin angular momentum of $+\frac{1}{2}\hbar$ and the spin down state with the spin angular momentum of $-\frac{1}{2}\hbar$. The two eigenstates are degenerate in energy when there is no magnetic field. At thermal equilibrium without any magnetic field, the spin is

in an equal mixture of the spin up and down state leading to an overall average spin component measured to be 0.

Usually it is convenient to use the Pauli matrices to describe the three spin angular momentum projected onto the three spatial coordinates.

$$\sigma_x = \begin{bmatrix} 0 & 1 \\ 1 & 0 \end{bmatrix}, \sigma_y = \begin{bmatrix} 0 & -i \\ i & 0 \end{bmatrix}, \sigma_z = \begin{bmatrix} 1 & 0 \\ 0 & -1 \end{bmatrix}$$

Spin states may change due to the interaction between the spin and other particles in the environment, like nuclei or phonons [10,11,12,13, 14]. The interaction causes a spin to relax between its two eigenstates. Studying spin relaxation will help us understand the interaction between the spin and the environment.

The spin of a particle is robust against Coulomb interactions with its surrounding enviroments, which enables a spin state to maintain its coherence for a long time and makes the spin a good candidate for quantum computing [6,7]. The main form of interaction between the spin and its environment is magnetic in nature.

As mentioned earlier, without any magnetic field the two spin states are degenerate in energy. Since there is no preferred orientation direction, the spin polarization is random in space. When an external magnetic field is applied, the spin will align or precess along the external magnetic field depending on the initial spin state. The spin will align parallel or anti-parallel to the external magnetic field. The spin not parallel or anti-parallel to the external magnetic field will precess with a certain frequency, called the Larmor frequency ω_L, defined as

$$\omega_L \equiv g\mu_B B \tag{6-1}$$

where g is a factor describing the strength of the interaction between the particle and the magnetic field, μ_B is the Bohr magneton, and B is the magnetic field.

The precession of a single spin in an external magnetic field, as illustrated in Figure 6.1, can be modeled with an equation of motion as the following.

$$\frac{d\vec{s}}{dt} = g\mu\vec{B} \times \vec{s} \tag{6-2}$$

where $\vec{s}$ is the spin vector.

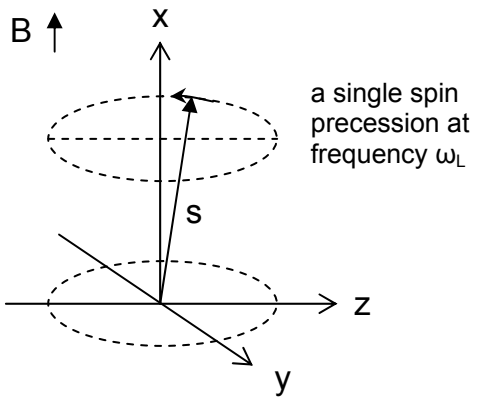

Figure 6.1 Spin precession in a magnetic field

For a static magnetic field along the x direction, the solution is the rotation of the spin components in the y-z plane.

$$s_y(t) = s_y(0)e^{i\omega_L t}$$
$$s_z(t) = s_z(0)e^{i\omega_L t} \tag{6-3}$$

where s_y and s_z are the spin components along the y and the z directions, $s_y(0)$ and $s_z(0)$ are the initial values of the spin components s_y and s_z.

The Fourier Transform of the time evolution of the spin component s_z gives a single frequency in the frequency domain.

$$S_z(\omega) = \frac{\hbar^2}{2}\delta(\omega - \omega_L) \tag{6-4}$$

6.2 Spin noise physics

With an understanding of the quantum properties of spin, the physics of spin noise can be explored. As discussed in Chapter 2, noise is usually represented as some random fluctuation in measurements, and it is always associated with uncertainty in experiments. In general the uncertainty can be classified into two categories. One category is the external noise from the classical fluctuation of the environment, e.g. thermal fluctuation or mechanical vibration. The external noise

can be reduced or even cancelled in measurements once the physical process is understood and better techniques are available. For example, the thermal noise can be reduced by stabilizing the temperature. Common mode noise in laser power fluctuation can be cancelled through balanced detection. The other category of noise is the intrinsic fluctuation of the quantum systems, illustrating the fundamental uncertainty of quantum mechanics. The internal quantum noise cannot be cancelled or removed in measurements until new quantum states, like squeezed states, are used. For instance, the laser shot noise cannot be reduced by balanced detection. By studying the properties of the quantum noise, the underlying physics can be explored.

Spin noise comes from the intrinsic quantum fluctuation of spin states [15], which has been measured in nuclei [16], electrons in atoms [2,3], and electrons in semiconductors [4]. The fundamental statistical model is the Poisson distribution for rare events statistics, as discussed in Chapter 2. For a random variable with N as its expectation value, the fluctuation, or standard variance, is $\sqrt{N}$. Similarly, a system with N spins shows a $\sqrt{N}$ intrinsic quantum fluctuation.

Assume there are N electrons in a certain volume. Without any magnetic field the electron spins are randomly oriented in space. The $\sqrt{N}$ spin fluctuation is averaged out over the volume due to the random orientation of the N spins in the volume.

When an external magnetic field B is applied, all electron spins precess along the external magnetic field at the same Larmor frequency. If there is no spin flip and spin relaxation, there will be no net spin precessing due to the equal probability of the two spin eigenstates. When a spin flips, it causes a net spin precessing along the external magnetic field. The net precessing spin produces a rotating-magnetic field in the plane perpendicular to the external magnetic field at the Larmor frequency. By measuring the rotating spin-induced magnetic field, the spin noise of the electrons can be measured.

With a total of N spins, there will be $\sqrt{N}$ spin flips. Each spin flip produces a small rotating magnetic field in the plane perpendicular to the external magnetic

field. The total effect, which is not averaged out due to the quantum property of the spin noise as shown in the laser shot noise, is amplified by a factor of $\sqrt{N}$. If there is no spin relaxation, all rotating magnetic fields will be at the same Larmor frequency. When spin relaxation occurs, the rotating frequency will be broadened in the spectrum by the spin relaxation rate, which is similar to the line width in atomic transitions caused by the population decay.

A simple spin relaxation model can explain the line shape anticipated in the spin noise measurement [17].

$$\frac{d\vec{s}}{dt} = -\frac{\vec{s}}{T_2} + g\mu\vec{B}\times\vec{s} \tag{6-5}$$

where T_2 is the spin relaxation time.

For a static magnetic field the solution is a damped oscillation of the spin components.

$$\begin{aligned} s_y(t) &= s_y(0)e^{-\frac{t}{T_2}+i\omega_L t} \\ s_z(t) &= s_z(0)e^{-\frac{t}{T_2}+i\omega_L t} \end{aligned} \tag{6-6}$$

Through a Fourier Transform, the damped oscillation gives a Lorentzian shape with the center frequency at the Larmor frequency and the width determined by the spin relaxation time T_2 .

$$S_z(\omega) = \frac{\hbar^2}{2}\left(\frac{T_2}{1+T_2^2(\omega-\omega_L)^2} + \frac{T_2}{1+T_2^2(\omega+\omega_L)^2}\right) \tag{6-7}$$

Useful information can be obtained from the spin noise measurement. With a precise measurement of the magnetic field and the Larmor frequency, the g factor can be extracted. More importantly, the spin relaxation time can be obtained from the width of the spin noise signal.

6.3 Physics of the spin noise measurement

The spin noise measurement is based on polarization dependent optical absorption and the Faraday rotation effect. A detailed explanation of the physics of optical absorption, the refractive index, and the Faraday rotation effect will

help us understand the experimental technique used for the spin noise measurement. In this section, first a simple classical Lorentz model is used to explain the origin of absorption and the refractive index. Then using the same model and including the effect of an external magnetic field, the physics of the Faraday rotation is discussed.

6.3.1 Absorption and refractive index of a two-level system

With a simple classical Lorentzian model [18], the optical absorption (and refractive index) of dielectric materials can be modeled with a Lorentzian (and derivative) line shape. When a plane wave of monochromatic light propagates through a dielectric material, electrons bound in the atoms oscillate with the electrical field induced by the light, causing material polarization.

The equation of motion for the polarization is

$$\frac{d^2\vec{P}}{dt^2} + \Delta\omega_a \frac{d\vec{P}}{dt} + {\omega_a}^2 \vec{P} = \frac{Ne^2}{m}\vec{E}(t)$$
$$\vec{E}(t) = \hat{\varepsilon} E_0 e^{i\omega t} \tag{6-8}$$

where $\vec{P}$ is the polarization, $\Delta\omega_a$ is the transition line width, ω_a is the transition frequency, N is the total number of electrons, $\vec{E}(t)$ is the electric field due to the light, and $\hat{\varepsilon}$ is the polarization vector.

The polarization can be obtained by solving the equation in the frequency domain.

$$\vec{P}(t) = \hat{\varepsilon} P_0 e^{i\omega t}$$
$$P_0 = \left[\frac{Ne^2}{m} \frac{1}{({\omega_a}^2 - \omega^2) + i\Delta\omega_a} \right] E_0 \tag{6-9}$$

The material susceptibility is

$$\chi(\omega) \equiv \frac{\vec{P}(t)}{\varepsilon_0 \vec{E}(t)} = \frac{Ne^2}{\varepsilon m} \frac{1}{({\omega_a}^2 - \omega^2) + i\Delta\omega_a} \tag{6-10}$$

In vacuum Maxwell equations yield a plane wave solution. Light propagates at the same speed, independent of the wavelength.

$$\nabla^2 \vec{E} - \frac{1}{c_0^{\,2}} \frac{\partial^2 \vec{E}}{\partial t^2} = 0 \tag{6-11}$$

$$\vec{E}(t) = \hat{\varepsilon} E_0 e^{-i(\vec{k} \bullet \vec{r} - \omega t)}$$

$$k \equiv \frac{\omega}{c_0} \tag{6-12}$$

In a dielectric material, light still propagates as a plane wave. However, light at different wavelengths propagate at different speeds, due to the wavelength dependent material susceptibility. By solving Maxwell's equation for a plane wave propagating in the dielectric material, the material's absorption and the refractive index can be estimated.

$$\nabla^2 \vec{E} - \frac{1}{c_0^{\,2}} \frac{\partial^2 \vec{E}}{\partial t^2} = \frac{1}{c_0^{\,2}} \frac{\partial^2}{\partial t^2} (\chi \vec{E}) \tag{6-13}$$

$$\vec{E}(t) = \hat{\varepsilon} E_0 e^{-i(\vec{k} \bullet \vec{r} - \omega t)}$$

$$k^2 \equiv \frac{\omega^2}{c^2} = \frac{\omega^2}{c_0^{\,2}} (1 + \chi) \tag{6-14}$$

$$n^2 \equiv \frac{c_0^{\,2}}{c^2} = 1 + \chi_{real} = 1 + \frac{Ne^2}{\varepsilon m} \frac{(\omega_a^{\,2} - \omega^2)}{(\omega_a^{\,2} - \omega^2)^2 - \Delta\omega_a^{\,2}}$$

Usually the transition line width is much smaller than the transition frequency, which means $\Delta\omega_a \ll \omega_a$ and $\omega \approx \omega_a$.

$$\omega_a^{\,2} - \omega^2 = (\omega_a + \omega)(\omega_a - \omega) \approx 2\omega_a(\omega_a - \omega) \tag{6-15}$$

$$\chi(\omega) \approx \frac{Ne^2}{2\varepsilon m \omega_a} \frac{1}{(\omega_a - \omega) + i\frac{\Delta\omega_a}{2\omega_a}}$$

$$\chi = \chi_{real} + i\chi_{imaginary} = \chi_0 \left[\frac{\Delta x}{1 + (\Delta x)^2} + i \frac{1}{1 + (\Delta x)^2} \right] \tag{6-16}$$

$$\chi_0 = \frac{Ne^2 \Delta\omega_a}{4\varepsilon m \omega_a^{\,2}}, \Delta x = \frac{\omega_a - \omega}{\frac{\Delta\omega_a}{2\omega_a}}$$

The real part yields the dispersion shown in the refractive index, and the imaginary part is responsible for the absorption, as plotted in Figure 6.2. It clearly shows that the absorption has a Lorentzian line shape, and the refractive index has a derivative line shape.

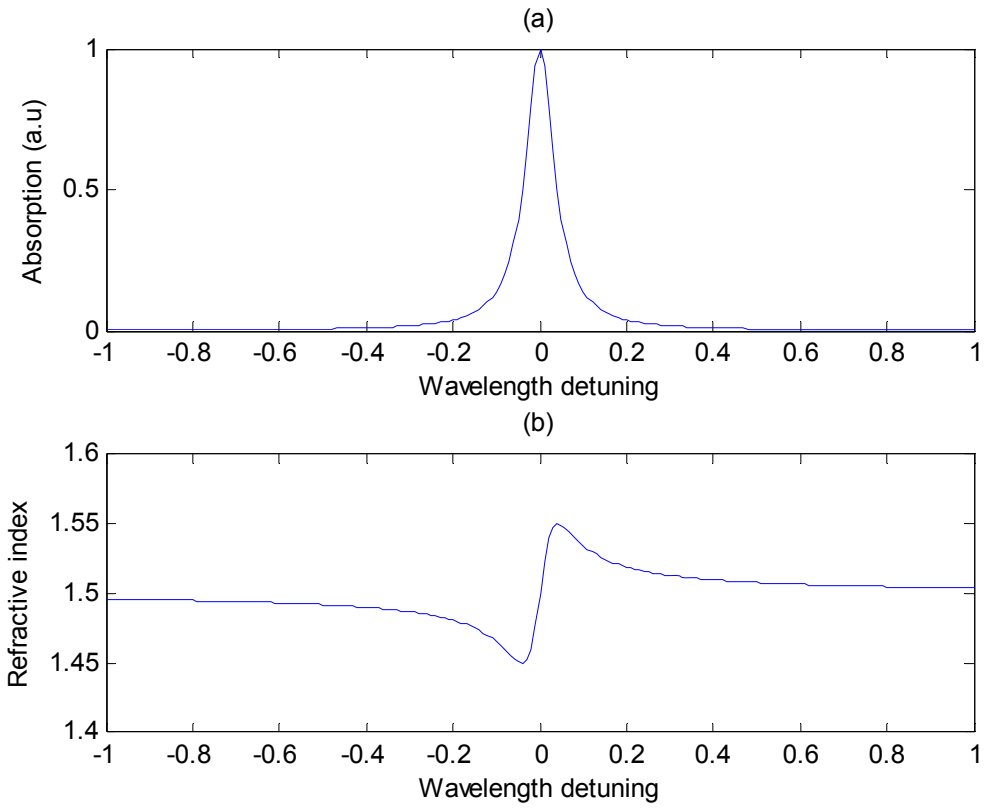

Figure 6.2 (a) Lorentzian shape absorption (b) derivative shape refractive index

The selection rule of a transition is defined by angular momentum conservation during the atomic transition. In semiconductors the transition from the ground state to the first excited state is the generation of an electron-hole pair. For electrons with spin up or down states in semiconductors, the optical transitions have a selection rule $\Delta l = 1$. This selection rule requires circularly polarized light with $\sigma+$ or $\sigma-$. Without a magnetic field, the two transitions are degenerate with same Lorentzian absorption and derivative refractive index at the same frequency, as illustrated in Figure 6.3.

With a simple classical Lorentzian model, the two transitions with orthogonal polarization are degenerate at the same frequency with identical Lorentzian-shaped absorption and derivative refractive index.

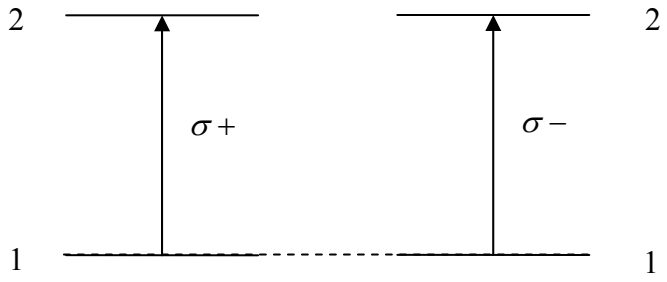

Figure 6.3 Two degenerate transitions with orthogonal circular polarizations

6.3.2 Faraday rotation effect

Faraday rotation is the effect by which the polarization of a linearly polarized beam is rotated by an angle θ when the beam passes through a dielectric material with a magnetic field oriented along the light propagation direction, as illustrated in Figure 6.4.

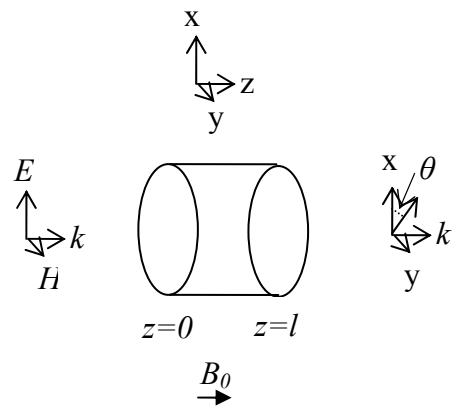

Figure 6.4 Faraday rotation effect

The magnetic field induces a small change in the refractive index, which is different for left and right circularly polarized light, creating a circular birefringence. This circular birefringence causes the Faraday rotation by an angle $\theta \propto \frac{\Delta n}{\lambda} Bl$, where Δn is the difference in the refractive indices for left and right circularly polarized light, λ is the wavelength, B is the strength of the magnetic field, and l is the length of the dielectric material.

This model can be understood by the effects of the magnetic fields on the motion of electrons in the dielectric materials. With circularly polarized light going through the dielectric material, the bounded electrons in the dielectric material experience a circular electrical field and rotate in circles in the plane perpendicular to the light propagation direction. Under a magnetic field, the rotating electrons are subjected to the Lorentz force, which may point towards or away from the center of the electron rotation, depending on whether the circularly polarization is the left or right. So the electron rotation will be affected differently for the left and the right circularly polarized light, which gives the Faraday rotation.

The Faraday rotation effect can be explained with the same classical Lorentzian model used to explain the absorption and the refractive index by adding the effect of the magnetic field on the electrons [19].

The equation of motion is

$$\frac{d^2\vec{P}}{dt^2}+\Delta\omega_a\frac{d\vec{P}}{dt}+{\omega_a}^2\vec{P}=-\frac{Ne^2}{m}\left(\vec{E}(t)+\frac{1}{Ne}\frac{d\vec{P}}{dt}\times\vec{B}\right) \qquad (6\text{-}17)$$
$$\vec{E}(t)=\hat{\varepsilon}E_0e^{i\omega t}$$

For the experimental geometry, B is along the z direction and the motion of the electrons is in the x-y plane. The equation reduces to the following two equations.

$$\begin{aligned}\frac{d^2\vec{P}_x}{dt^2}+\Delta\omega_a\frac{d\vec{P}_x}{dt}+\frac{e}{m}B_z\frac{d\vec{P}_y}{dt}+{\omega_a}^2\vec{P}_x&=-\frac{Ne^2}{m}\vec{E}_x(t)\\ \frac{d^2\vec{P}_y}{dt^2}+\Delta\omega_a\frac{d\vec{P}_y}{dt}-\frac{e}{m}B_z\frac{d\vec{P}_x}{dt}+{\omega_a}^2\vec{P}_y&=-\frac{Ne^2}{m}\vec{E}_y(t)\end{aligned} \qquad (6\text{-}18)$$

These two equations can be represented with an equation of circular motion.

$$\frac{d^2\vec{P}_\pm}{dt^2}+\Delta\omega_a\frac{d\vec{P}_\pm}{dt}\mp\frac{e}{m}iB_z\frac{d\vec{P}_\pm}{dt}+{\omega_a}^2\vec{P}_\pm=-\frac{Ne^2}{m}\vec{E}_\pm(t) \qquad (6\text{-}19)$$
$$\vec{P}_\pm=\vec{P}_x\pm i\vec{P}_y,\vec{E}_\pm=\vec{E}_x\pm i\vec{E}_y$$

If we assume

$$\begin{aligned}\overline{P}_x&=\hat{\varepsilon}P_0e^{i\omega t},\overline{P}_y=0\\ \overline{P}_\pm&=P_0e^{i(\omega t-k_\pm z)}\end{aligned} \qquad (6\text{-}20)$$

thus

$$P_{\pm} = \left[\frac{Ne^2}{m} \frac{1}{(\omega_a{}^2 - \omega^2 \pm \frac{e}{m} B_z \omega) + i\Delta\omega_a} \right] E_{\pm} \tag{6-21}$$

Define

$$\omega_b = \frac{e}{2m} B_z \tag{6-22}$$

Since $\omega_b \ll \omega_a$, and $\omega_b \ll \omega$, $\omega\omega_b$ can be replaced by $\omega_a\omega_b$.

$$\omega_a{}^2 - \omega^2 \pm 2\omega_b\omega \approx \omega_a{}^2 - \omega^2 \pm 2\omega_a\omega = (\omega_a \pm \omega_b)^2 - \omega^2 \tag{6-23}$$

$$n_{\pm}{}^2 \approx 1 + \frac{Ne^2}{\varepsilon m} \frac{(\omega_a \pm \omega_b)^2 - \omega^2}{((\omega_a \pm \omega_b)^2 - \omega^2)^2 + \Delta\omega_a{}^2} \tag{6-24}$$

$$\theta = \frac{\pi L}{\lambda}(n_+ - n_-) = \frac{\omega L}{c}(n_+ - n_-) \approx \frac{\omega L}{cn} \frac{Ne^2}{\varepsilon m} \frac{2\omega_a\omega_b(\omega_a{}^2 + \omega_b{}^2 - \omega^2)}{(\omega_a{}^2 + \omega_b{}^2 - \omega^2)^2 - 4\omega_a{}^2\omega_b{}^2} \tag{6-25}$$

It is shown that for material with a simple Lorentzian-shaped absorption, the refractive index has a derivative line shape with the maximum (minimum) at the wavelength with the fastest absorption change, as shown in Figure 6.2. When a magnetic field is applied, the energy of one transition ($\sigma+$) goes down by ω_b, and the other ($\sigma-$) goes up by ω_b (Zeeman Effect). The two transitions become non-degenerate, shown in Figure 6.5.

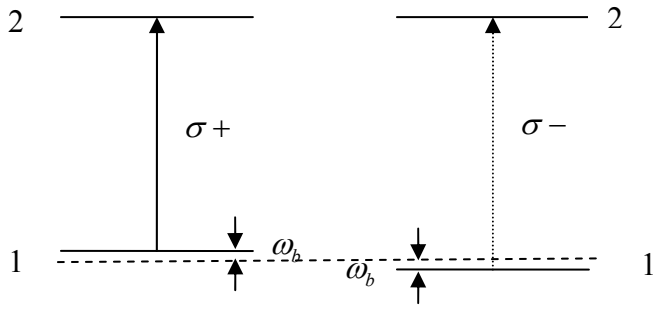

Figure 6.5 Non-degeneracy due to the energy shift caused by a magnetic field

Correspondingly, the absorption curves are shifted by ω_b in two opposite directions for the spin up and the spin down states, while the line shape remains

unchanged. So the original Lorentzian absorption curve is split into two identical Lorentzian curves separated by $2\omega_b$, corresponding to the two orthogonal circular polarizations, as illustrated in Figure 6.6(a).

The change of the absorption affects the refractive index. The refractive index of the two orthogonal circular polarizations can be obtained from the two shifted Lorentzian absorption curves, illustrated in Figure 6.6(b). The difference between the two refractive indices for the two orthogonal circular polarizations can be estimated from the subtraction of the two derivative curves, plotted in Figure 6.6(c). The laser wavelength dependence of the Faraday rotation can be estimated from Figure 6.6(c).

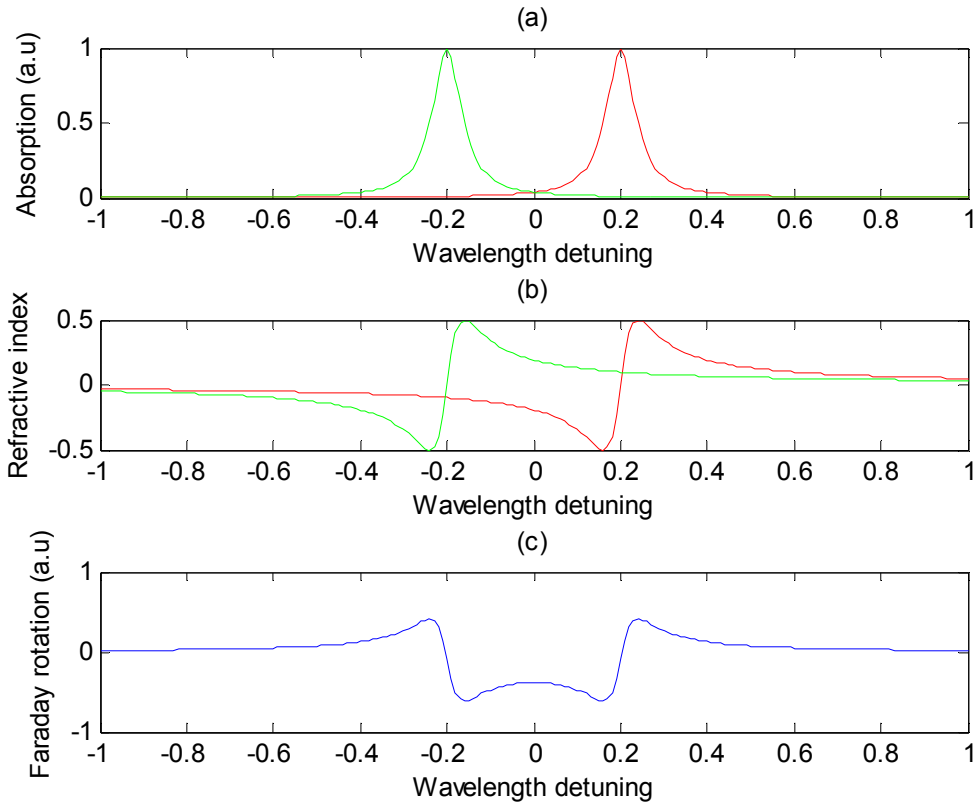

Figure 6.6 (a) Absorption, (b) refractive index of the two orthogonal circular polarized light, (c) Faraday rotation

The maximum positive Faraday rotation, which corresponds to the maximum positive signal, is obtained at the peaks of refractive index, which are the steepest

places of the absorption. There are two zero-crossing near the resonance, one for the left and one for the right. The maximum negative Faraday rotation, which corresponds to the maximum negative signal, appears at the peaks of the negative dips of the shifted derivative refractive-index curves. Actually, the maximum negative Faraday rotation gives the biggest signal in experiments since the absolute value determines the signal strength. At the absorption resonance there is still some Faraday rotation, but it is not the maximum. The amount of rotation drops quickly when the wavelength moves away from the wavelength corresponding to the positive maximum signal, with the rate at which the refractive index drops.

It is understandable that the maximum signal appears at the wavelength where the absorption changes most rapidly, rather than the peak of the absorption, since the Faraday Effect is caused by the change of the absorption, not the absorption itself. Since most materials with Lorentzian absorption shapes have the most rapid change of absorption at a wavelength away from resonance, often in the transparency region with very weak absorption. This gives the advantage of measuring spin dynamics without disturbing the measured system. On the other hand, when the wavelength is too far away from the resonance, where absorption is too weak to get enough change of absorption, the Faraday rotation will be too small to be measured. So there is a working wavelength range for spin noise studies.

The above analysis assumes a simple symmetric Lorentzian absorption line shape, which works well for atoms, but not for the bulk semiconductors. GaAs shows strong absorption above the exciton absorption peak (818nm or 1.515eV) with an absorption coefficient of $1.2\times10^{4}/cm$, and weak absorption in the transparency region (>844nm or below 1.47eV) with an absorption coefficient less than $10/cm$. Between the weak absorption (<1.47eV or 844nm) and the strong absorption (>1.515eV or 818nm) there is a transition region called the Urbach tail, where the absorption coefficient goes up exponentially [18]. Our experiments are conducted in the Urbach tail region. Further discussion about the wavelength dependence of the spin noise will appear in later chapters.

6.4 Spin noise measurement on n-GaAs

Spin noise measurements are challenging mainly due to the weak signal strength, which is usually below other noise sources like laser shot noise or electrical thermal noise, which always exist in experiments. The balanced detection scheme discussed in Chapter 2 is utilized to get to the shot noise limit, and a background subtraction technique is used to obtain the weak spin noise signal which is below laser shot noise and electrical thermal noise. These techniques have been used in measuring the spin noise of atoms [3, 21] and n-GaAs [4].

6.4.1 Spin noise measurement technique

As discussed earlier, spin noise gives a rotating spin component in the plane perpendicular to the external magnetic field. The rotating spin component causes an oscillating magnetic field along the z direction, as illustrated in Figure 6.7. Through the Faraday rotation effect, the oscillating magnetic field gives an oscillating Faraday rotation angle, which can be measured with high sensitivity down to micro radians by using high quality polarization optics and the balanced detection technique.

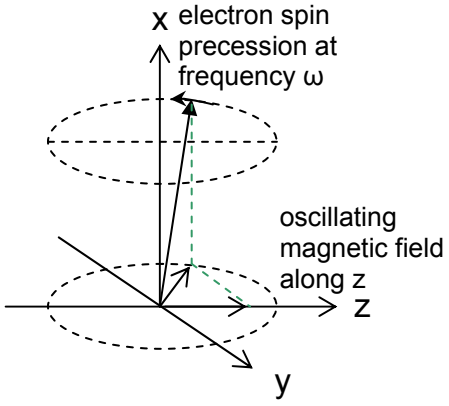

Figure 6.7 Oscillating magnetic field generated from the electron spin precessing

The experimental setup is illustrated in Figure 6.8.

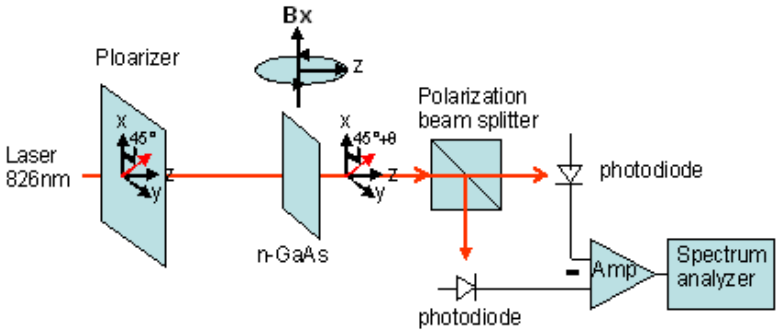

Figure 6.8 Spin noise measurement setup

A laser beam is tuned to 826nm, with the energy below the GaAs bandgap (816nm or 1.515eV), where most of the laser power is absorbed and some laser power is transmitted. The laser beam goes through a polarizer along the 45 degree direction in the x-y plane before it hits a sample in a cryostat. The sample is a 350μm thick n-doped GaAs substrate with a doping density of $1.8\times10^{16}/cm^3$ at 8K. Lenses are used to focus the laser beam on the sample and the detectors. The transmitted laser beam passes through a polarization beam splitter and is detected by a balanced detector. A weak magnetic field along the x direction causes the electron spin to precess, which produces an oscillating magnetic field along the z direction. Birefringence due to the oscillating magnetic field provided by the Faraday rotation effect is detected by a balanced detector and a spectrum analyzer.

6.4.2 Magnetic field dependence of spin noise of n-GaAs

With the above experimental setup, the spin noise of GaAs was measured at different magnetic fields, as shown in Figure 6.9. It is clear that the spin noise spectrum appears at different frequencies at different magnetic fields. As explained before, the spin noise spectrum can be fitted with a Lorentzian curve, as shown in the inset of Figure 6.9. From the curve fitting, important parameters including peak frequency and spectrum width can be extracted. The magnetic field dependence of these parameters is plotted in Figure 6.10. As expected, it is shown that the shift of the peak frequency, the Larmor frequency, depends

linearly on the magnetic field strength, while the spectral width and the amplitude remain constant independent of the magnetic field strength.

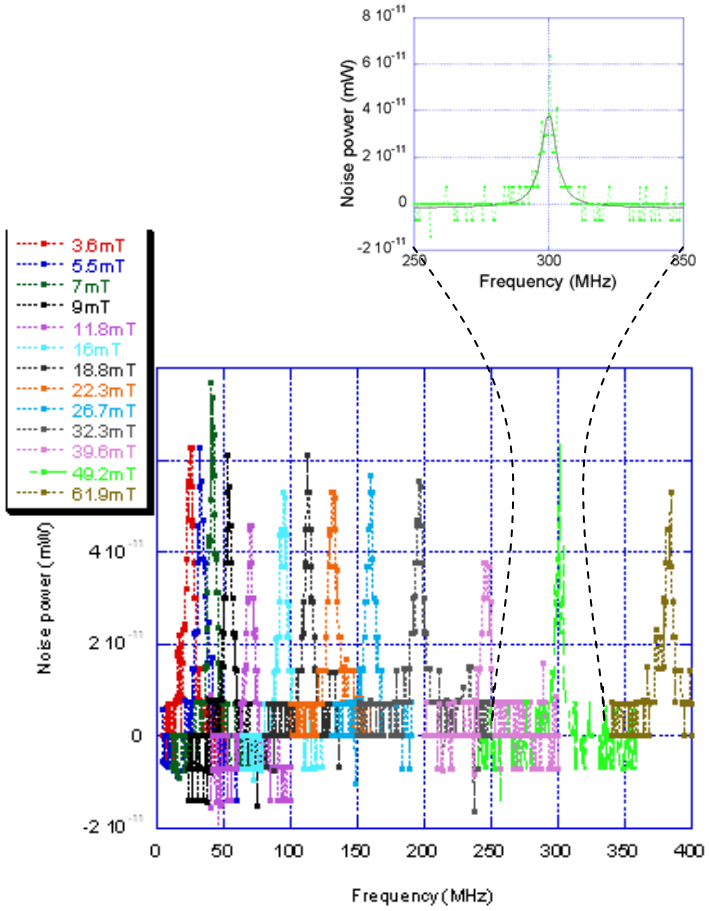

Figure 6.9 Magnetic field dependence of the spin noise (the inset is a Lorentzian fit for the spin noise spectrum measured at 49.2mT.)

As discussed in the section 6.2, information about the electron spin can be obtained from the spin noise spectrum. The electron g factor can be extracted from the slope of the linear dependence of the Lamar frequency on the magnetic field. With a linear fit to the data, the slope gives a g factor magnitude about 0.45. From the spectral width, the electron spin relaxation time can be estimated. With

the number in Figure 6.10, the spectrum width is 7MHz, which yields a spin relaxation time of about 45ns. These numbers agree with the ones measured with other methods [22,23].

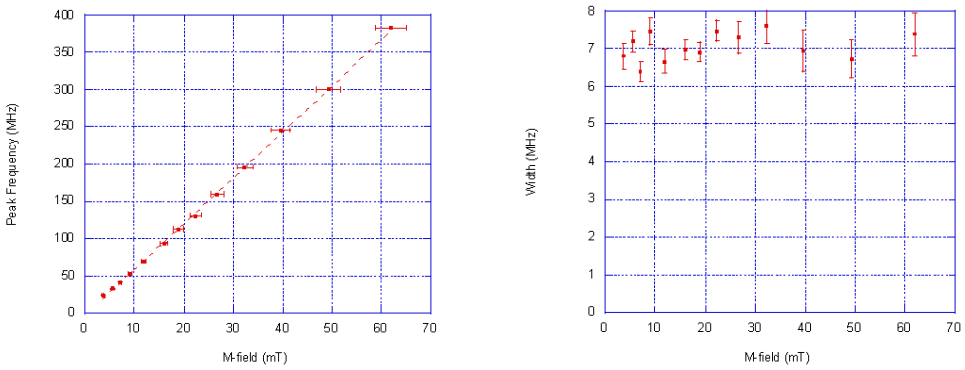

Figure 6.10 Peak frequency and the spectrum width of the spin noise vs. magnetic field (the dashed line is a linear fit.)

Spin noise provides a new method of studying the spin in atoms and semiconductors. Compared with other methods which measure the spin relaxation time through the Hanle effect and time resolved Faraday rotation, spin noise is measured with the laser tuned to the transparent regime away from resonance, while all other techniques use resonant excitation. One advantage of the spin is that the measured system is not disturbed in below-resonant excitation. For GaAs, spin noise was measured below the band gap energy with the laser tuned to the Ulbach tail region where absorption is weak and is caused by impurities and defects. Hanle effect measurements use above band gap excitation, and time-resolved Faraday rotation measurements use near-band gap excitation. Both techniques create carriers and the measured system is disturbed.

Another advantage of spin noise is that the spin relaxation time can be measured over a large wavelength range from below to above resonance. For semiconductors, it enables spin relaxation time measurement from below-band gap to above band gap. This will help in studying the spin relaxation time of doped, photo-generated, and electrically injected electrons. Most previous experiments have been focused on the spin relaxation time of photon-generated

electrons. With spin noise, the difference between the spin relaxation time of different electrons can be studied.

In summary, the quantum properties of spin were discussed and the physical origin of the spin noise was explored. Based on a classical Lorentzian model, the optical absorption, refractive index, and the Faraday rotation effect were explained to illustrate the spin noise measurement. The spin noise measured at different external magnetic fields provided the g factor and the spin relaxation time for the doped electron in n-GaAs.

Bibliography

[1] J. B. Johnson, Thermal agitation of electricity in conductors, Nature 119, 50 (1927).
[2] T. Mitsui, Spontaneous noise spectroscopy of an atomic magnetic resonance, Phys. Rev. Lett. 84, 5292 (2000).
[3] S. A. Crooker, D. G. Rickel, A. V. Balatsky, et al., Spectroscopy of spontaneous spin noise as a probe of spin dynamics and magnetic resonance, Nature 431, 49 (2004).
[4] M. Oestreich, M. Romer, R. J. Haug, et al., Spin noise spectroscopy in GaAs, Phys. Rev. Lett. 95, 216603 (2005).
[5] C. T. W. Moonen, P. C. M. Vanziji, J. A. Frank, et al., Functional magnetic-resonance-imaging in medicine and physiology, Science 250, 53 (1990).
[6] C. Piermarocchi, P. Chen, L. J. Sham, D. G. Steel, Optical RKKY Interaction between charged semiconductor quantum dots", Phys. Rev. Lett. 89, 167402 (2002).
[7] J. R. Petta, A. C. Johnson, J. M. Taylor, E. A. Laird, A. Yacoby, M. D. Lukin, C. M. Marcus, M. P. Hanson, A. C. Gossard, Coherent manipulation of coupled electron spins in semiconductor quantum dots, Science 309, 2180 (2005).
[8] M. Kroutvar, Y. Ducommun, D. He, J. J. Finley, Optically programmable quantum dots, Science 432, 81 (2004).
[9] J. M. Kikkawa, I. P. Smorchkova, N. Samarth, et al., Room-temperature spin memory in two-dimensional electron gases, Science 277, 1284 (1997).
[10] Pil Hun Song and K. W. Kim, Spin relaxation of conduction electrons in bulk III-V semiconductors, Phys. Rev. B 66, 035207 (2002).
[11] R. I. Dzhioev, V. L. Korenev, I.A. Merkulov, et al., Manipulation of the Spin Memory of Electrons in n-GaAs, Phys. Rev. Lett. 88, 256801 (2002).
[12] P. I. Tamborenea,1,2 M. A. Kuroda,1 and F. L. Bottesi1, Spin relaxation in n-doped GaAs due to impurity and electron-electron Elliot-Yafet scattering, Phys. Rev. B 68, 245205 (2003).
[13] J. S. Colton1, T. A. Kennedy, A. S. Bracker, and D. Gammon, Spin Lifetime Measurements in MBE-Grown GaAs Epilayers, phys. stat. sol. (b) 233, 445 (2002).
[14] S. Krishnamurthya, M. Schilfgaarde, N. Newman, Spin lifetimes of electrons injected into GaAs and GaN, Apl. Phys. Lett. 83, 1761 (2003).
[15] F. Bloch, Nuclear induction. Phys. Rev. 70, 460–474 (1946).
[16] T. Sleator, E. L. Hahn, C. Hilbert, J. Clarke, Nuclear-spin noise. Phys. Rev. Lett. 55, 1742–1745 (1985).
[17] M. Braun, J. Konig, Faraday-rotation fluctuation spectroscopy with static and oscillating magnetic fields, Phys. Rev. B 75, 085310 (2007).
[18] A. E. Siegman, Lasers, Academic Press, 1986.
[19] B. D. Guenther, Modern Optics, John Wiley & Sons, 2001.
[20] M. D. Sturge, Optical absorption of Gallium Arsenide between 0.6 and 2.75eV, Phys. Rev. 127, 768 (1962).

[21] B. Mihaila, S. A. Crooker, D. G. Rickel, et al., Quantitative study of spin noise spectroscopy in a classical gas of K-41 atoms, Phys. Rev. A 74, 043819 (2006).
[22] J. M. Kikkawa, D. D. Awschalom, Resonant spin amplification in n-type GaAs, Phys. Rev. Lett. 80, 4313 (1998).
[23] R. I. Dzhioev et al., Low-temperature spin relaxation in n-type GaAs, Phys. Rev. B 66, 245204 (2002).

Chapter 7

Optical and Thermal Effects on Spin Noise Measurement of n-GaAs

In Chapter 6 the spin noise of doped electrons in n-GaAs was measured under different magnetic fields. The slope of the Larmor frequency as a function of magnetic field gives the electron g factor, and the spin noise spectrum width represents the electron spin relaxation time. Due to the high sensitivity of spin noise measurement and its property of not disturbing the system under study, it can be a powerful tool to study the spin dynamics in atoms and semiconductors [1-5]. To obtain a comprehensive understanding of the spin noise technique, it is important to understand how optical and local environment parameters affect spin noise spectra.

It is important to understand optical effects to provide a comprehensive understanding of the spin noise measurement. Spin noise spectra shows a strong dependence on laser energy and intensity. Even though the spin noise technique has the advantage of not substantially disturbing the system under study by detuning from the resonance, it is desirable to know to what degree the system is disturbed in the spin noise measurement and how to minimize the disturbance. Usually spin noise measurement is difficult due to the low signal level, and it is important to optimize experimental parameters to improve spin noise signal effectively. Also local environmental effects on the spin noise measurement need to be understood to use the spin noise technique properly. As a sensitive experimental technique, spin noise measurement is capable of measuring small changes on the g factor and spin relation time due to local change like temperature,

external electric field, and extra optical excitations. Multiple effects may mix in a single spin noise measurement. It is necessary to isolate individual environmental effects to extract correct information from the spin noise measurement.

In this chapter we will study the optical and thermal effects on spin noise measurement of n-GaAs. First, the signal strength of the spin noise is analyzed based on a Lorentzian model with saturation behavior. Then optical effects including both the laser energy and laser intensity on spin noise are studied. Next, the temperature effect on the spin noise is discussed. At the end of the chapter the spin relaxation mechanisms in n-GaAs are discussed to explain the optical excitation induced spin relaxation observed in our experiments.

7.1 A two level system with Lorentzian line shape and saturation

The signal strength of the spin noise measurement is defined as the integrated power under the Lorentzian shaped spin noise spectrum. The spin noise power we measure, represented by a spin noise voltage V_{sn}, is determined by two factors. One factor is the change of refractive index caused by electron spin relaxation in the measured system. This can be seen as a Faraday rotation angle, which may depend on laser energy or intensity as discussed in Chapter 6. The other factor is the laser power on the detector from the laser beam transmitted through the sample, which is a carrier to convert the refractive index change into an oscillating electrical signal we can measure through photodetectors. The laser power on the detector is independent of the refractive index change and its effect on the spin noise voltage can be removed by normalization. The spin noise voltage V_{sn} is

$$V_{sn} = RR_i P\theta(\lambda, I) \tag{7-1}$$

where R is the equivalent resistance of the photo detector circuit, R_i is the responsivity of the photo detector, P is the laser power on the photo detector, and $\theta(\lambda, I)$ is the Faraday rotation angle due to spin relaxation.

When we change experimental parameters, both the Faraday rotation angle and the transmitted laser power change. To obtain the refractive index change

caused by the spin relaxation, the spin noise power is normalized to a fixed reference level so that the transmitted laser power on the detector does not affect the normalized spin noise power $V_{snn}(\lambda, I)$

$$V_{snn}(\lambda, I) = RR_i\theta(\lambda, I) \tag{7-2}$$

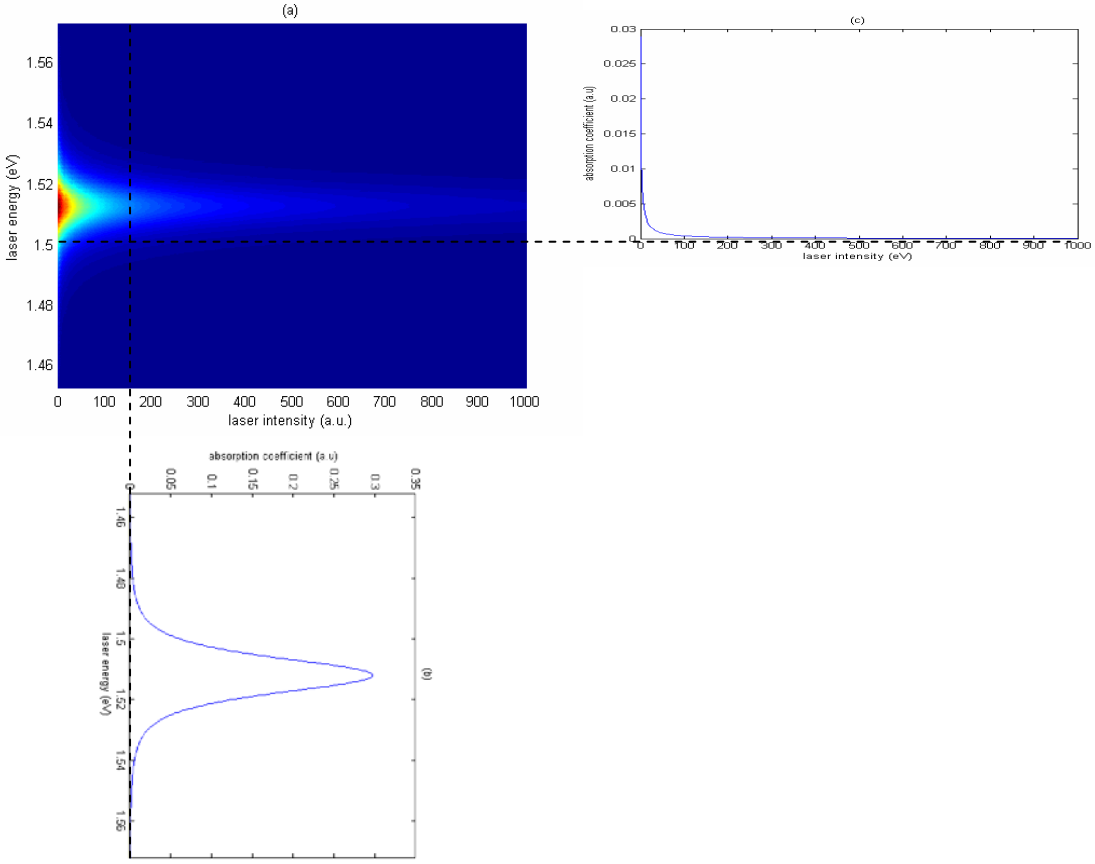

Figure 7.1 Absorption of a two level system with Lorentzian line shape and saturation behavior (a) pseudo colormap of the laser energy and intensity dependent absorption coefficient (b) a vertical cross section plot of the absorption coefficient along laser energy showing the Lorentzian line shape (c) a horizontal cross section plot of the absorption coefficient along laser intensity showing saturation

With a two-level model with a Lorentzian line shape and saturation behavior, the absorption coefficient $\alpha(\lambda, I)$ gives a laser energy and intensity dependence,

$$\alpha(\lambda, I) = \frac{1}{1+\left(\frac{\Delta}{\gamma}\right)^2} \frac{\alpha_0}{1+\frac{I}{I_{sat}}} \tag{7-3}$$

where Δ is the detuning, γ is the width of the Lorentzian curve, α_0 is the absorption coefficient at zero laser intensity, and I_{sat} is the saturation intensity at which the absorption drops by half. Figure 7.1 illustrates the laser energy and intensity dependent absorption.

In Chapter 6 the spin noise signal strength is discussed with a Lorentzian absorption model for atomic systems without considering the saturation effect. Here we add two more assumptions to simplify equations to illustrate the effect of the laser beam on the refractive index change. First, we assume that the energy splitting ω_b in the Faraday effect is much smaller than the laser detuning Δ. In our spin noise measurement with GaAs, the energy splitting ω_b is below 2μeV, while the laser detuning Δ is at least 5meV. Second, we assume that the laser intensity affects population in the two level system, which further changes the absorption and refractive index. This can be seen by solving the density matrix for a simple two level system and observing the dependence of the real and imaginary parts of the polarization on laser intensity. The normalized spin noise signal strength can be simplified as

$$V_{snn}(\lambda, I) = RR_i\theta(\lambda, I) = RR_i \frac{\omega L}{cn} \frac{e^2}{\varepsilon m} \frac{1}{\Delta(\lambda)} \frac{N_0}{1+\frac{I}{I_{sat}}}, \tag{7-4}$$

where ω the angular frequency of the laser, L is the thickness of the sample, c is the speed of light, n is the refractive index, e is the charge of an electron, ε is the dielectric constant, m is the mass of an electron, and $\Delta(\lambda)$ is the detuning. Figure 7.2 shows the laser energy and intensity dependent spin noise power. It shows that the spin noise power reaches maximum on resonance with low laser intensity, and the spin noise power drops rapidly when the laser energy is detuned away from the resonance and when the laser intensity is increased.

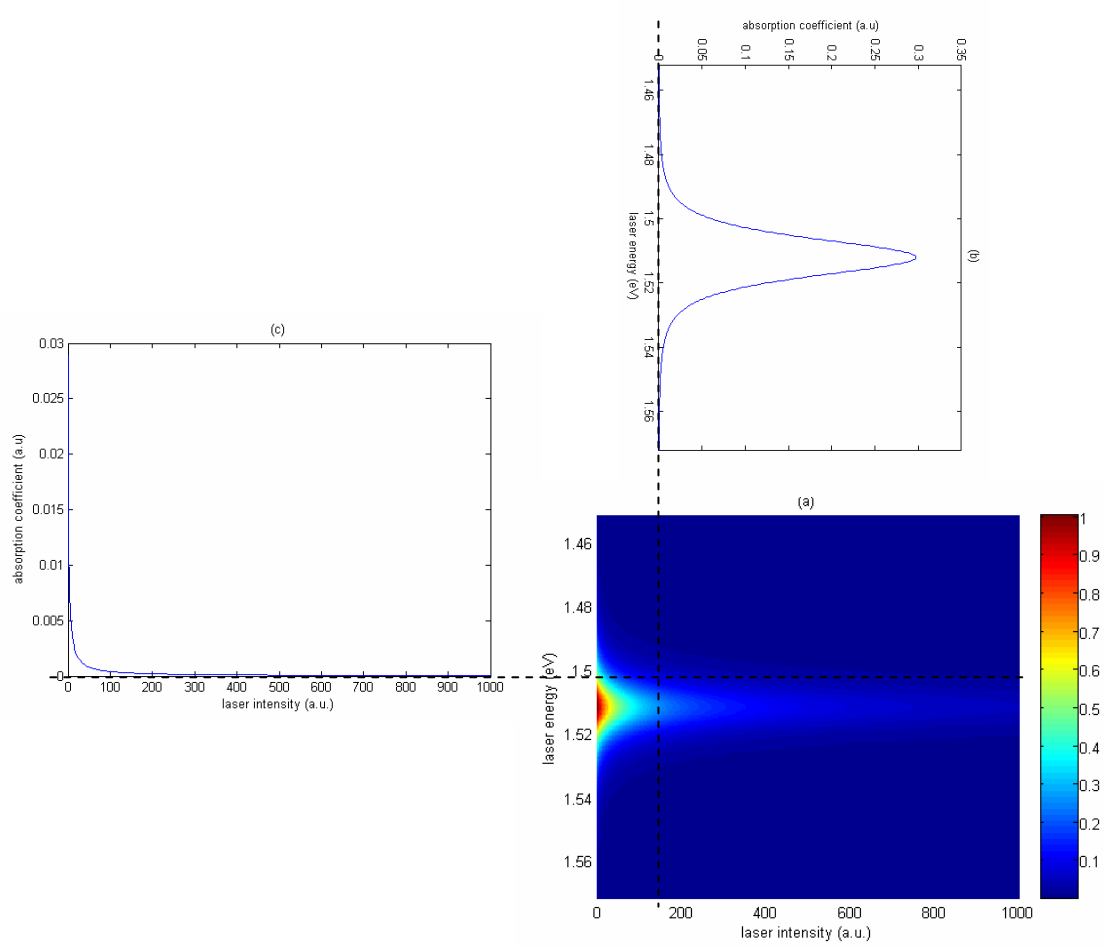

Figure 7.2 Spin noise power of n-GaAs (a) pseudo colormap of the laser energy and intensity dependent spin noise power (b) a vertical cross section plot of the spin noise power along laser energy (c) a horizontal cross section plot of the spin noise power along laser intensity

7.2 Optical effects on the spin noise in n-GaAs

To understand the effect of the laser beam on the spin noise measurement, we change the laser energy and laser intensity to study how these parameters affect the spin noise width and power. For each experimental condition, we measure the optical transmission through the sample, $T(\lambda, I)$, as a ratio between the transmitted laser power and the input laser power with corrections for surface reflections. Then an absorption coefficient $\alpha(\lambda, I)$ is calculated from the transmission with the formula

$$T(\lambda, I) = \frac{P_{out}(\lambda, I)}{P_{in}} \tag{7-5}$$

$$\alpha(\lambda, I) = -\frac{1}{L}\ln T \tag{7-6}$$

where $P_{out}(\lambda, I)$ is the laser power transmitted through the sample with a dependence on laser energy and intensity, P_{in} is the normalized input laser power getting into the sample by taking into account the surface reflection due to refractive index mismatch, and L is the sample thickness. Spin noise width and power are extracted from Lorentzian curve fitting parameters of the measured spin noise spectra, and the spin relaxation time is inferred from the spin noise width.

7.2.1 Laser energy dependence of the spin noise in n-GaAs

Laser energy dependence of the spin noise is studied with a fixed laser intensity of about 169μW/μm^2 at 9.5K, over the laser energy range 1.465eV to 1.505eV, which is the laser energy range where the spin noise of the sample is large enough to be measured. When the laser energy goes above 1.505eV, the transmission is too low to measure the spin noise, due to strong absorption close to the GaAs band gap 1.519eV for the sample thickness of 0.35mm. When the laser energy goes below 1.465eV, the spin noise also becomes too weak to measure, due to the off resonance detuning effect.

Figure 7.3 (a) shows the measured laser energy dependent transmission and the absorption coefficient of the n-GaAs sample between 1.465eV to 1.505eV. The measurement errors are from the uncertainty of the optical power meter. The transmission is high and the absorption coefficient is small between 1.465eV and 1.49eV, far away from the GaAs band gap, defined as a transparency regime where absorption is weak due to the off resonance effect. From 1.49eV to 1.505eV, close to the GaAs band gap, the transmission drops and the absorption coefficient increases rapidly.

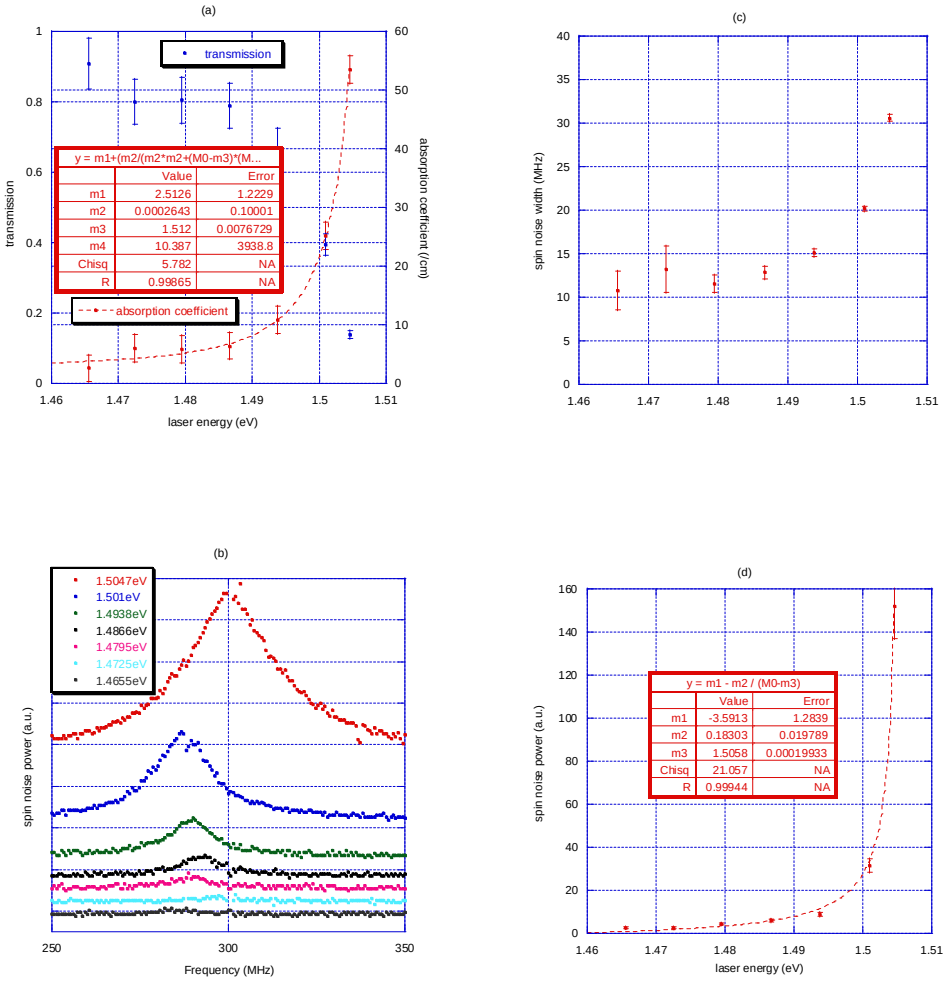

Figure 7.3 Laser energy dependence of the spin noise of the n-GaAs sample (with a laser intensity of about 169μW/μm^2 at 9.5K) (a) transmission and absorption coefficients of the n-GaAs sample over laser energy (b) spin noise spectra at different laser energies (c) spin noise width over laser energy (d) spin noise power over laser energy (Theory for the solid lines is described in the text)

The absorption of GaAs in this laser energy range is the Urbach tail caused by impurity absorption. The Urbach tail absorption we measured with our sample is similar to that measured by others [6-8]. A few models have been presented to describe the Urbach tail absorption [9-11].For simplicity we use a Lorentzian model to fit the laser energy dependent absorption coefficient, as illustrated by a

dashed line in Figure 7.3(a), which gives a peak absorption centered at $1.512 \pm 0.008eV$. This number matches the exciton absorption peak at 1.514eV, 5meV below the band gap in GaAs at low temperature. Rather than explaining the physics for the Urbach tail absorption, the Lorentzian model is a phenomenological model for absorption coefficient covering both the transparency and absorption regimes that can be used to explain the spin noise width and power measurements.

The measured spin noise spectra over the same laser energy range are plotted in Figure 7.3(b) as vertically shifted plots. The peaks are not aligned at the same frequency due to the difficulty of obtaining the same magnetic field in different measurements since the magnetic field is adjusted by physical positions of magnets. Spin relaxation time and spin noise power are extracted as curve fitting parameters and plotted over laser energy in Figure 7.3(c) and Figure 7.3(d).

Figure 7.3(c) shows that the spin noise width starts from about 10MHz at 1.465eV, and from 1.465eV to 1.49eV it increases slowly to about 15MHz in the transparency regime where the laser energy is far away from the GaAs band gap. When the laser energy approaches the GaAs band gap in the absorption regime, the spin noise width increases rapidly to 30MHz. By extrapolating the laser energy dependent spin noise width to the lower limit of the laser energy, it is expected that the width of the spin noise would be about 10MHz, which represents an upper limit of the electron spin relaxation time of about 32ns. If the laser energy dependence of the spin noise width holds for higher laser energy until the absorption peak, then by extrapolating the curve to the absorption peak of 1.512eV, the upper limit of the spin noise width could approach hundreds of MHz, which indicates the electron spin relaxation time could be reduced to a few ns when the laser energy hits the band gap.

Figure 7.3(d) shows that the spin noise power is very small at 1.465eV, it increases linearly and slowly in the transparency regime from 1.465eV to 1.49eV, and it goes up very rapidly in the absorption regime from 1.49eV to 1.505eV. The laser energy dependent spin noise power can be fitted with a detuning effect as in Equation (7-4), which supports the Lorentzian model we used for the laser energy

dependent absorption we measured. Similar results have been observed for the spin noise measurement in atomic gas [1] and GaAs [5]. In Reference [5], the same laser energy dependent absorption, spin noise width and power have been observed for n-GaAs. A Lorentzian model based on near band gap absorption is presented to explain the laser energy dependence of the spin noise power. But there is significant discrepancy between the measurement and the calculation results. Our Lorentzian model based on the measured absorption coefficients gives a better fit between the measurement and calculation results.

The laser energy dependence of the spin noise indicates that the spin noise power is optimized at high laser energy close to the absorption peak with the side effect of broadening spin noise width. To minimize the spin noise width broadening caused by the near resonance excitation, it is desirable to measure the spin noise with far off resonance detuning, with a cost of reduced spin noise power.

7.2.2 Laser intensity dependence of the spin noise in n-GaAs

This subsection explores how the spin noise is affected by the laser intensity. We choose the laser energy of 1.501eV, which gives a proper absorption to obtain the spin noise signal over a wide laser intensity range on our sample. When the laser energy is too high (close to the GaAs band gap), the absorption is too strong to get enough transmitted laser power to measure the spin noise. When the laser energy is too low, the absorption is too weak to provide enough spin noise signal. To adjust the laser intensity we change the laser power in front of the cryostat from 2mW to 200mW with a fixed focal spot size. The transmission and absorption coefficients of the n-GaAs sample over a laser intensity range from 28 $\mu W/\mu m^2$ to 1121$\mu W/\mu m^2$ are plotted in Figure 7.4(a). When the laser intensity increases from 28 $\mu W/\mu m^2$ to 200$\mu W/\mu m^2$ the transmission increases linearly and the absorption coefficient drops with the laser intensity. When the laser intensities go above 200$\mu W/\mu m^2$, the transmission remains constant and the absorption coefficient becomes saturated. This laser intensity dependent absorption

coefficient can be well fitted with a two level saturation model as Equation (7-3), as shown by the dashed line in Figure 7.4(a).

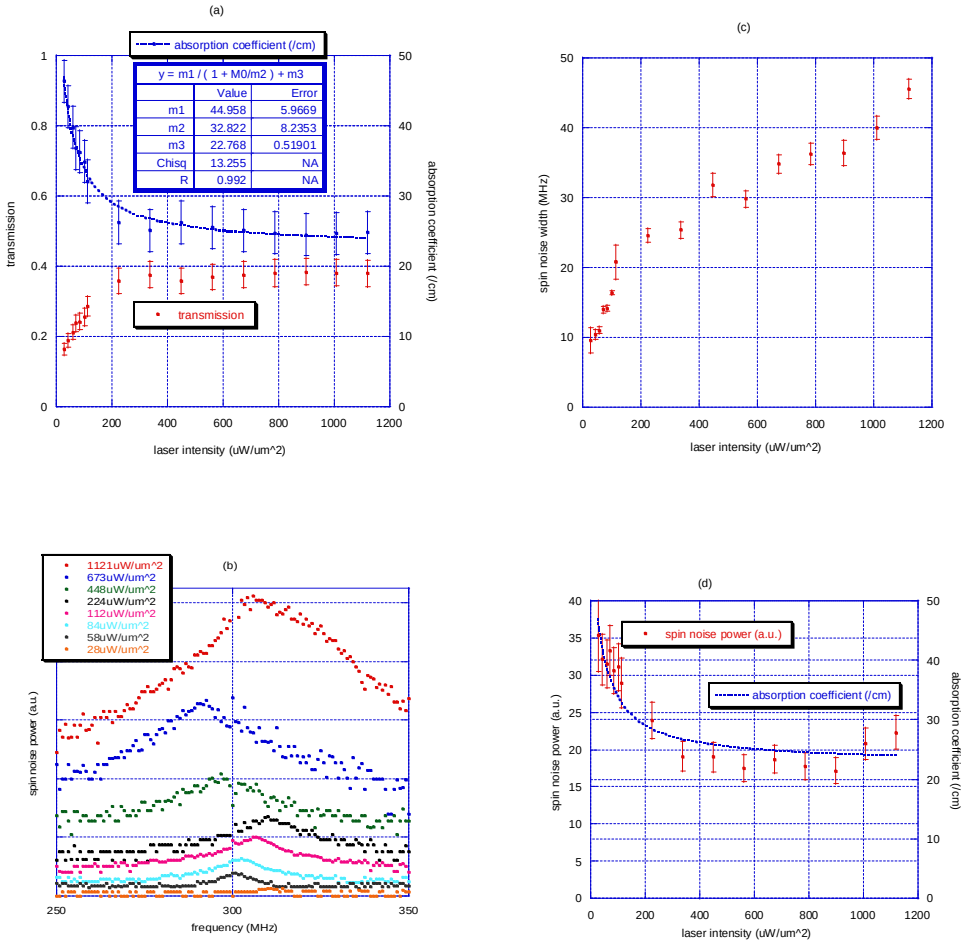

Figure 7.4 Laser intensity dependence of the spin noise of the n-GaAs sample with laser energy about 1.501eV at 9.5K (a) transmission and absorption coefficients of the n-GaAs sample as a function of laser intensity (b) spin noise spectra at different laser intensity (c) spin noise width as a function of laser intensity (d) spin noise power as a function of laser intensity (e) spin noise power vs. absorption coefficient

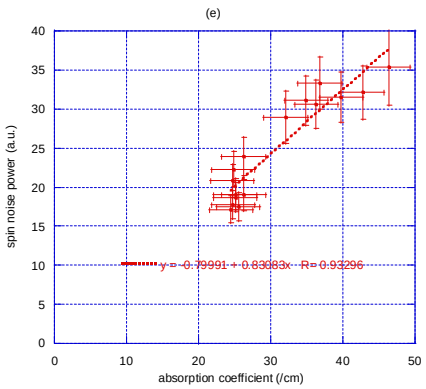

It gives a zero laser intensity absorption coefficient of $\alpha_0 = 45 \pm 6cm^{-1}$, a saturation intensity of $I_{sat} = 33 \pm 8\mu W / \mu m^2$, and a non-saturating absorption coefficient about $\alpha_{ns} = 23 \pm 1cm^{-1}$.

The spin noise spectra at different laser intensities are shown in Figure 7.4(b) with vertically shifted plots for clarity. The peaks are not aligned at the same frequency due to difficulty of repeating the same magnetic field in different measurements. Spin noise width and power are extracted as curve fitting parameters and plotted over laser intensity in Figure 7.4(c) and Figure 7.4(d). Figure 7.4(c) shows that the spin noise width starts from about 10MHz and increases linearly at a relatively high rate in the low laser intensity regime, and it increases linearly at a relatively low rate in the high laser intensity regime. By extrapolating the laser intensity dependent width to the lower limit of zero laser intensity, the width of the spin noise becomes about 5MHz, which represents an upper limit of the electron spin relaxation time of about 63ns. By extrapolating the laser intensity dependent width to the upper limit of an infinite laser intensity, we estimate the spin noise width which can either increase to hundreds of MHz or saturate at somewhere between 50MHz and hundreds of MHz, which indicates a reduced spin relaxation time of a few ns at high laser intensities.

In the laser intensity dependence measurement, there is no noticeable intensity dependence of the sample temperature in the low laser intensity regime. In the high laser intensity regime, we observed that the laser causes the sample temperature to increase, which indicates a heating effect caused by the laser power absorbed by the sample. The temperature sensor shows that temperature increases from about 8K at low laser intensity to 9.5K at the maximum laser intensity. The temperature dependence of spin noise measurements discussed later shows that an increasing temperature of a few K may cause spin noise width to increase by a few MHz. Even with a small thermal effect in the measurement, the main effect is still caused by the laser intensity rather than the temperature change.

A similar laser intensity dependent result was verified at low laser energy where absorption is weak and the thermal effect is negligible.

The spin noise power over laser intensity is plotted in Figure 7.4(d), with a dashed blue curve showing the laser intensity dependent absorption coefficients we measured in Figure 7.4(a). The spin noise power starts from a relatively large number, then it drops quickly in the small absorption regime, and it stays constant in the transparency regime. The spin noise power follows a similar trend as the absorption coefficient, as we expected from Equation (7-4). Figure 7.6(e) gives a linear fit between the absorption coefficient and the spin noise power. To verify that the effect is caused by the laser intensity rather than laser power, we also adjusted the laser intensities by changing the focus spot size through lenses with different focus length under a fixed laser power. Similar laser intensity dependent results were observed and confirmed that the spin noise depends on the laser intensity rather than the laser power. Similar laser intensity dependent results have also been measured with a lower laser energy in the transparency regime.

Compared with the laser energy dependence of the spin noise width, a comparable lower limit of 5MHz to 10MHz is obtained at either lower laser energy (i.e. long wavelength) or in the limit of zero laser intensity. Both are associated with minimal absorption of the laser power by the sample. Any increase of optical absorption, either by moving the laser energy to the strong absorption regime or by increasing laser power, increases the spin noise width. This indicates that the 5MHz to 10MHz spin noise width is associated with the upper limit of the electron spin relaxation time of about 32ns to 63ns in the n-GaAs sample without optical excitation. Spin relaxation is enhanced under optical excitation, reducing the electron relaxation time to a few ns.

An optical effect on spin noise power is observed because the spin noise power is proportional to the change of the refractive index, which depends on the laser energy and intensity. The maximum spin noise power can be obtained with near resonance excitation.

7.3 Thermal effects on the spin noise in n-GaAs

To study the thermal effect, we measure spin noise over the temperature range of 1.4K to 50K, which is the temperature range when the spin noise is big enough to be measured. The laser energy is 1.501eV with an intensity of about 200μW/μm^2.

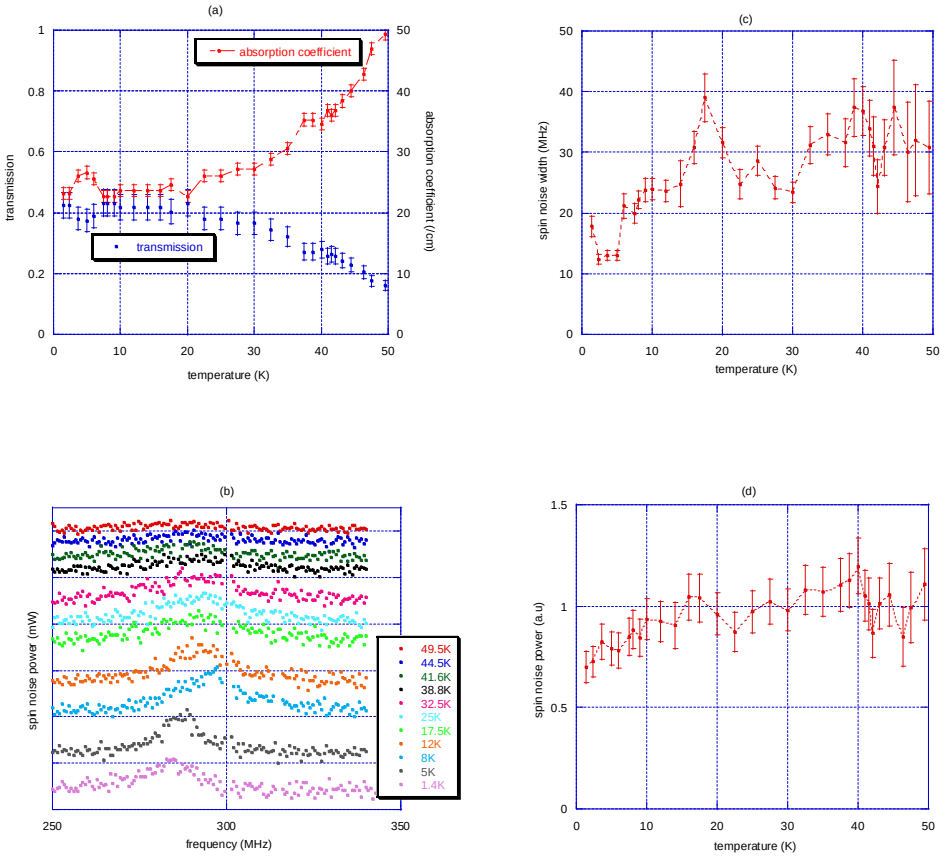

Figure 7.5 Temperature dependence of the spin noise of the n-GaAs sample with laser energy at 1.501eV and intensity about 200μW/μm^2 (a) transmission and absorption coefficients of the n-GaAs sample as a function of temperature (b) spin noise spectra at different temperature (c) spin noise width as a function of temperature (d) spin noise power as a function of temperature

The transmission and absorption of the n-GaAs sample over the temperature range 1.4K to 50K is plotted in Figure 7.5(a). At low temperatures below 20K, the absorption remains constant. As the temperature increases further above 20K, the

absorption gets stronger because the GaAs band gap shifts to a lower energy when the temperature increases. The spin noise data over the same temperature range is plotted in Figure 7.5(b) as vertically shifted plots. The peaks are not aligned at the same frequency due to difficulty of repeating the same magnetic field in different measurements, as discussed earlier. Spin noise width and power are extracted as curve fitting parameters, plotted as a function of laser energy in Figure 7.5(c) and Figure 7.5(d). Figure 7.5(c) shows that the spin noise width drops from 18MHz at 2.4K to 12MHz at 5K, then increases to 40MHz around 18K, and drops to 25-30MHz above 23K. In the temperature range 5K to 18K, the increase of the spin noise width could be associated with thermal excitation of impurities. There could be due to mixed complications of both thermal and optical effects. Further investigation is necessary to understand this temperature dependence.

Figure 7.5(d) shows that the spin noise signal strength slightly increases from 1.4K to 18K, drops and goes back from 18K to 25K, and stays same above 25K.

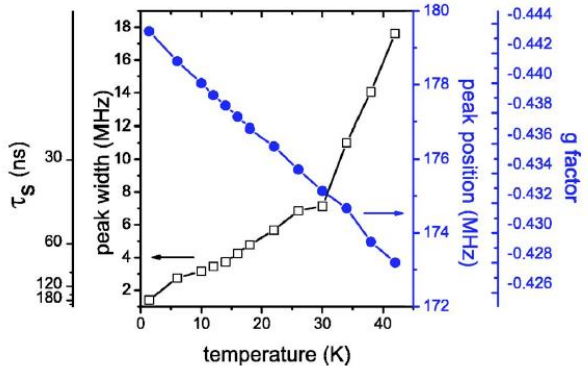

FIG. 4. (Color online) Temperature dependence of the peak position, i.e., g^*, and signal width, i.e., τ_s, for sample A with $n_d^A = 1.8 \times 10^{16}$ cm^{-3} at $\lambda = 835$ nm and $B = 30$ mT.

Figure 7.6 Temperature dependence of spin noise width and peak position measured by Romer (Figure Romer[5])

Figure 7.6 shows the spin noise width measured by Romer [5] with laser energy of 1.46eV. Romer's data gives much narrower spin noise width and shows a monotonic increasing of the spin noise width when the temperature increases from 3K to 40K. The difference between our data and Romer's data, measured with similar samples but different laser energy and intensity, indicates that at the

laser energy 1.501eV, where we measured the temperature dependence, the spin noise width is dominated by the optical effect rather than the thermal effect. From our study on the laser energy and intensity effect on the spin noise width, we learned that the spin noise width gets broadened with laser energy close to the bandgap energy and high intensity. To study the temperature effect, the spin noise need to be measured with laser energy far away from the bandgap energy, which we did not do due to the low signal level. Romer measured the temperature dependence with laser energy far away from the bandgap energy with a system with a higher sensitivity. Here the temperature dependence was measured with laser energy near the bandgap energy to verify whether the spin noise width we measured at high laser intensities is due to the optical or thermal effect. The temperature dependence supports the conclusion that the spin noise width we measured at high laser intensities is due to the optical rather than thermal effect.

7.4 Optical excitation induced spin relaxation

From the above experiments we found that the spin relaxation time in n-GaAs depends on laser energy, intensity and temperature. To understand how spin relaxation is affected by these parameters, spin relaxation mechanisms in semiconductors need to be discussed. In this section, first the three spin relaxation mechanisms in n-GaAs are briefly introduced. Then related experimental and theoretical work on spin relaxation time in n-GaAs is summarized. At the end of the section a possible explanation of optical effects on the measured spin noise width is presented.

7.4.1 Spin relaxation mechanisms in n-GaAs

There are mainly three spin relaxation mechanisms in semiconductors, and one may dominate over others depending on the material and temperature [12-14].

The Elliot-Yafet (EY) mechanism is a spin relaxation mechanism due to spin-orbit coupling [15]. The electron wave functions with opposite spin orientation mix due to spin-orbit coupling, which induces spin relaxation by momentum

scattering with photons and impurities. The spin relaxation time τ_s^{EY} caused by the EY mechanism is

$$\frac{1}{\tau_s^{EY}} = A\left(\frac{k_B T}{E_g}\right)^2 \eta^2 \left(\frac{1-\frac{2}{\eta}}{1-\frac{3}{\eta}}\right)^2 \frac{1}{\tau_p^{ii}(E)} \tag{7-7}$$

$$\eta = \frac{\Delta_{sos}}{\Delta_{sos} + E_g} \tag{7-8}$$

where A is a dimensionless constant varying from 2 to 6 depending on the scattering mechanism for the momentum relaxation, k_B is the Boltzmann constant, T is the temperature, E_g is the band gap energy, and Δ_{sos} is the spin-orbit splitting of the valance band.

The D'yakonov-Perel (DP) mechanism is a spin relaxation mechanism caused by the ionized impurity scattering in n-type III-V semiconductors [16]. For crystals without inversion symmetry, electrons in the conduction band with same k vector but opposite spin orientations have different energies, which depend on the k vector. This energy splitting is equivalent to the energy splitting caused by an internal magnetic field depending on the magnitude and orientation of the k vector. The electron spin precesses along the equivalent internal magnetic field, causing spin relaxation. When the electron scatters by an ionized impurity, the precession axis is randomized after scattering. When the spin precession period is longer than the momentum relaxation time, multiple scattering occurs before the spin relaxation is achieved. Therefore, spin relaxation is suppressed by the frequent scattering with ionized impurities, and the spin relaxation time is inversely proportional to the momentum relaxation time. The spin relaxation time caused by the DP mechanism is

$$\tau_s^{DP} = \frac{315}{16}\alpha^{-2}\frac{\hbar^2 E_g}{E^3 \tau_p(E)} \tag{7-9}$$

$$E = E_F = \frac{(3\pi^2\hbar^2 n_D)^{\frac{2}{3}}}{2m} \tag{7-10}$$

where α is a dimensionless factor (0.07 for GaAs), $\hbar$ is the Plank constant over 2π, E_F is the Fermi energy, $\tau_p(E)$ is the momentum relaxation time, and n_D is the doping density. The momentum relaxation time $\tau_p(E)$ is evaluated with the Brook-Herring method under the Born approximation by estimating the cross section of an electron scattering from a Coulomb potential screened by the degenerate electron gas.

$$\tau_p(E) = \frac{\varepsilon^2 E_F^{\frac{3}{2}} \sqrt{2m}}{\pi n_D e^4 \left(\ln(1+x) - \frac{x}{1+x} \right)} \tag{7-11}$$

$$x = \frac{8mE_F r_0^2}{\hbar^2} = 3^{\frac{1}{3}} \pi^{\frac{5}{3}} a_B n_D^{\frac{1}{3}} \tag{7-12}$$

$$r_0 = \frac{1}{2}\left(\frac{\pi}{3}\right)^{\frac{1}{6}} \left(a_B n_D^{-\frac{1}{3}} \right)^{\frac{1}{2}} \tag{7-13}$$

where x is a dimensionless number, and r_0 is the screening radius.

The Bir-Aronov-Pikus (BAP) mechanism is a spin relaxation mechanism due to electron-hole scattering through exchange and annihilation interactions [17]. BAP dominates in p doped semiconductors rather than n doped semiconductors.

These spin relaxation time in n-GaAs has been studied both theoretically and experimentally [13-14]. The Hanle effect can be used to measure the external magnetic field induced depolarization rate in luminescence. This method was used to study spin relaxation time of optically excited electrons in n-GaAs at different doping densities [13]. For n-GaAs with similar doping density as our sample, the spin relaxation time of optically excited electrons measured by the Hanle effect is in the same range as that of doped electrons measured by spin noise in the low laser power and weak absorption regime. It is found that increasing the doping density causes the spin relaxation time to drop linearly, explained as increasing the doping density increases the ionized impurity density and carrier momentum relaxation time. In the doping density range similar to our n-GaAs sample, the relation between the spin relaxation time and doping density was explained with the DP mechanism in Reference [13].

In the work of Song et. al [14], the spin relaxation time in III-V compound semiconductors was calculated by examining dominant spin relaxation mechanisms depending on the doping density and temperature. Reference [14] reinforces that for the doping density and temperature in our measurement, the dominant spin relaxation mechanism is the DP mechanism.

Based on the these works, we tried to explain the laser energy, power, and spot size dependent spin noise data with excitation induced spin relaxation by associating optical excitation with ionized impurity density.

7.4.2 Optical excitation induced spin relaxation in n-GaAs

From the above introduction, we learned that spin relaxation in sparely doped n-GaAs at low temperatures is dominated by the DP mechanism caused by electron scattering by ionized impurities. Due to the scattering mechanism, the electron spin relaxation time is inversely proportional to the electron momentum relaxation time. In this section, we will explore the excitation induced spin relaxation in n-GaAs due to impurity ionization to explain the laser energy and intensity dependence of the spin noise width we measured.

Without optical excitation, the momentum relaxation time depends on the concentration of the impurity, the temperature, and the electron effective mass. For a sample with a certain doping density, the electron momentum relaxation time is minimized at low temperature and no optical excitation. With optical excitation a laser beam tuned to the spectral range of the Urbach tail, where the impurity absorption dominates, causes impurities to be ionized, giving a laser energy and intensity dependent ionized impurity density. By studying the laser energy and intensity dependence of ionized impurity density in the n-GaAs sample, we can find the relation between the ionized impurity density and the spin noise width.

A simple model for the optical excitation effect on the ionized impurity density is to assume that the ionized impurity density $N_{ii}(\lambda, I)$ is proportional to the intensity of the absorbed light $I_{abs}(\lambda, I)$, which is exponentially attenuated when the laser propagates through the sample,

$$N_{ii}(\lambda, I) = N_{ii0} + \beta I_{abs}(\lambda, I), \tag{7-14}$$

$$I_{abs}(\lambda, I) = I_{in}(1 - e^{-\alpha(\lambda, I)z}), \tag{7-15}$$

where N_{ii0} is the ionized impurity density without optical excitation, β is the impurity ionization rate under optical excitation, I_{in} is the input laser intensity, $\alpha(\lambda, I)$ is the laser energy and intensity dependent absorption coefficient, and z is the propagation distance in the sample.

Depending on the laser energy and intensity, there are two regimes which give different optical excitation effects. One is the transparency regime, which appears at either low laser energy or high laser intensity (saturation regime). In this regime the absorption is small enough to be ignored, which gives laser energy and intensity independent absorption. In this regime, the ionized impurity density and the spin noise width are independent of the laser energy and intensity, which has been observed in atoms [1] and n-GaAs.

The other is an absorption regime, which occurs at laser energies near resonance (or band gap) or low laser intensity. Here the absorption is big enough that it can not be ignored and it shows a strong dependence on the laser energy and intensity, as we have seen in our spin noise measurement with n-GaAs. To treat the absorption regime correctly, we need to take into account the non uniformity of the intensity distribution within the sample, which gives different behaviors for laser energy dependence and laser intensity dependence.

With a fixed laser intensity, when the laser energy is tuned from low to high, the sample changes from a uniform transparency regime with a long interaction length but weak interaction strength into a non uniform absorption regime with a short interaction length but a strong interaction strength due to decreased penetration depth. In the transparency regime, where laser energy is low and absorption is weak, the laser beam passes through the sample with an almost uniform intensity, giving a low ionized impurity density due to the weak absorption. When the laser gets into the absorption regime where the laser energy is high and absorption is strong the laser beam is attenuated when it propagates

through the sample, giving a quickly increasing ionized impurity density as a function of laser energy due to the strong absorption.

With a fixed laser energy when the laser intensity increases from 0 to infinity the sample changes from a non-uniform absorption regime with a small interaction volume but relatively strong interaction strength to a uniform transparency regime with a large interaction volume but relatively weak interaction strength due to increased penetration area. In the small absorption regime, where laser intensity is low and absorption is relatively strong, the laser beam passes through the sample with small slightly attenuated laser intensity, giving a low ionized impurity density due to the weak laser intensity. When the laser gets into the saturation regime, where laser intensity is high and absorption is saturated, the laser beam passes through the sample with large slightly attenuated laser intensity, giving a slowly increasing ionized impurity density due to the strong absorption.

Based on the two level model with a Lorentzian line shape and saturation behavior, from experimentally measured absorption coefficients we numerically estimated the local laser intensity distribution along the laser propagation path for both cases, shown in Figure 7.7(a) and 7.7(b). Then the average ionized impurity is estimated, and it is found that the estimated ionized impurity density is proportional to the spin noise width, as shown in Figure 7.7(c) and 7.7(d). By plotting the spin noise width vs. the estimated optically excited impurity density, as shown in Figure 7.7(e) and 7.7(f), there are good linear fits between the spin noise width and the estimated optically excited impurity density. Figure 7.7(e) gives a y intersection of about 11.5MHz, which is close to the lower limit we measured for the laser energy dependent spin noise width. Figure 7.7(f) gives a y intersection about 5MHz, which is close to the lower limit we got for the laser intensity dependent spin noise width. The two lines give different slopes and y intersections indicating that the laser energy and intensity affect spin relaxation differently.

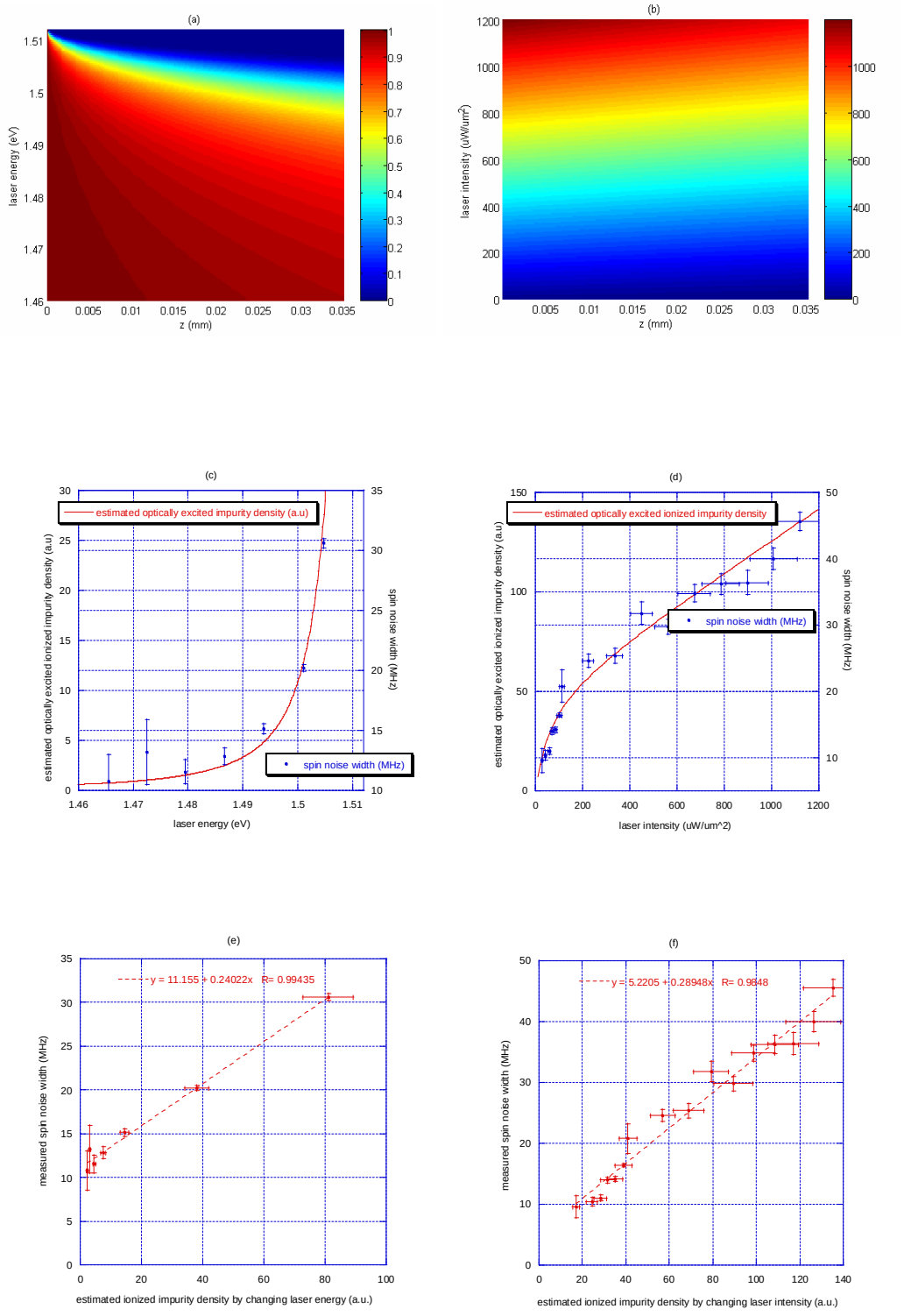

Figure 7.7 Optically excited ionized impurity density in n-GaAs (a) laser intensity in the sample with varying laser energy (b) laser intensity in the sample with varying laser intensity (c) estimated optically excited ionized impurity density

over laser energy (d) estimated optically excited ionized impurity density over laser energy (e) measured spin noise width vs. estimated optically excited ionized impurity density at different laser energies (f) measured spin noise width vs. estimated optically excited ionized impurity density at different laser intensities

From Figure 7.4(d), the experimentally measured absorption coefficients have a saturating term $\alpha_0 = 45 \pm 6cm^{-1}$ and a non-saturating term $\alpha_{ns} = 23 \pm 1cm^{-1}$. An interesting question is how much does the non-saturating term contribute to the optically excited ionized impurity density. Only part of the non-saturating term should contribute to the optically excited ionized impurity density because the non-saturating term exists even for pure GaAs with little impurity. Our calculation shows that the non-saturating absorption coefficient affects the shape of the optically excited ionized impurity density significantly. When the power absorbed by the non-saturating term is considered 100% contributing to the optically excited impurity ionization, the optically excited ionized impurity density increases linearly to the laser intensity. When the power absorbed by the non-saturating term is considered 0% contributing to the optically excited impurity ionization, the optically excited ionized impurity density gives saturation at high laser intensity. A background absorption coefficient α_{bg}, with a value between 0 and α_{ns}, is chosen to be a fitting parameter to obtain the best estimated optically excited ionized impurity density. The estimated optically excited ionized impurity density shown in Figure 7.7(d) was obtained with $\alpha_{bg} = 2.2cm^{-1}$. It might be interesting to study the laser intensity dependence at different laser energy to find if any relation exists between the non-saturating absorption coefficient $\alpha_{ns}(\lambda)$ and the background absorption coefficient $\alpha_{bg}(\lambda)$.

It is worth noting that the ionized impurity density remains a nonzero constant, determined by the doping density when the optical excitation effects approach zero. This can be approached experimentally by tuning the laser wavelength away from the band gap, reducing the laser intensity to zero, and

lowering the temperature. An even lower spin relaxation rate can be expected, which was recently measured [5].

In summary, the spin noise of n-GaAs under various laser energies, intensities and temperatures was studied to understand the effect of experimental parameters on the spin noise measurement in n-GaAs. It is found that the spin noise width approaches a maximum of 5MHz to 10MHz at low laser energy or low laser intensity, indicating an upper limit of the electron spin relaxation time of 32ns to 63ns. Optical excitation causes the spin relaxation time to drops to a few ns. With a two level system with Lorentzian line shape and saturation behavior, it is found that the spin noise width has a linear relationship with the optically excited ionized impurity density, and the spin noise power is associated with the absorption. In a spin noise measurement, experimental parameters need to be carefully chosen to measure the desired information.

Bibliography

[1] S. A. Crooker, D. G. Rickel, A. V. Balatsky, et al., Spectroscopy of spontaneous spin noise as a probe of spin dynamics and magnetic resonance, Nature 431, 49 (2004).

[2] M. Oestreich, M. Romer, R. J. Haug, et al., Spin noise spectroscopy in GaAs, Phys. Rev. Lett. 95, 216603 (2005).

[3] B. Mihaila, S. A. Crooker, D. G. Rickel, et al., Quantitative study of spin noise spectroscopy in a classical gas of 41K atoms, Phys. Rev. A 74, 043819 (2006).

[4] M. Braun et al., Faraday-rotation fluctuation spectroscopy with static and oscillating magnetic fields, Phys. Rev. B 75, 085310 (2007)

[5] M. Romer, J. Hübner, M. Oestreich, Spin noise spectroscopy in semiconductors, Rev. Sci. Inst. 78, 103903 (2007).

[6] M. D. Sturge, Optical Absorption of Gallium Arsenide between 0.6 and 2.75 eV, Phys. Rev. 127, 768 (1962).

[7] K. H. Goetz, D. Bimberg, H. Jürgensen, J. Selders, A. V. Solomonov, G. F. Glinskii, M. Razeghi, Optical and crystallographic properties and impurity incorporation of $GaxIn_{1-x}As_x$ ($0.44<x<0.49$) grown by liquid phase epitaxy, vapor phase epitaxy, and metal organic chemical vapor deposition, J. Appl. Phys. 54, 4543 (1983).

[8] K. Wei, F. H. Pollak, J. L. Freeouf, D. Shvydka, and A. D. Compaan, Optical properties of $CdTe_{1-x}S_x$ ($0<=x<=1$): Experiment and modeling, J. Appl. Phys. 85, 7418 (1999).

[9] R. J. Elliott, Intensity of Optical Absorption by Excitons, Phys. Rev. 108, (1957).

[10] F. Stern, Dispersion of the Index of Refraction Near the Absorption Edge of Semiconductors, Phys. Rev. 133, A1653 (1964).

[11] E. Y. Lin, T. S. Lay, T. Y. Chang, Accurate model including Coulomb-enhanced and Urbach-broadened absorption spectrum of direct-gap semiconductors, J. Appl. Phys. 102, 123511 (2007).

[12] G. E. Pikus and A. N. Titkov, in Optical Orientation, edited by F. Meier and B. P. Zakharchenya, North-Holland, Amsterdam, 1984.

[13] R. I. Dzhioev1, K. V. Kavokin, V. L. Korenev, M. V. Lazarev1, B. Ya. Meltser1, M. N. Stepanova1, B. P. Zakharchenya1, D. Gammon3, and D. S. Katzer, Low-temperature spin relaxation in n-type GaAs, Phys. Rev. B 66, 245204 (2002).

[14] Pil Hun Song, K. W. Kim, Spin relaxation of conduction electrons in bulk III-V semiconductors, Phys. Rev. B 66, 035207 (2002).

[15] Y. Yafet, in Solid State Physics, edited by F. Seitz and D. Turnbull, Academic, New York, 1963, Vol. 14.

[16] M. I. D'yakonov and V. I. Perel, Sov. Phys. JETP 33, 1053 (1971).

[17] G. L. Bir, A. G. Aronov, and G. E. Pikus, Sov. Phys. JETP 42, 705 (1976).

CHAPTER 8

Summary and Future Directions

This thesis work is a part of the effort to improve the experimental techniques to study the optical absorption properties of QDs for the ultimate goal of implementing optically driven QD based quantum computing. The experimental techniques are not limited to IFQDs and they can be applied to other QDs with bias structures. To conclude this thesis, here we summarize the thesis work and provide a few future directions.

8.1 Summary of thesis

Experimental techniques to measure the voltage dependent absorption of single QDs and optical effects on spin relaxation time in n-GaAs have been studied in this dissertation.

Differential reflectivity is studied to measure the nonlinear absorption of biased IFQDs to illustrate how a pump-probe experiment with optical modulation techniques measures a weak absorption signal below the limit set by laser power fluctuations with band width reduced lock-in detection. Under the condition of no transmission, DT is replaced by DR to measure the nonlinear absorption in reflection geometry. It was found that DR measures a combination of the real and the imaginary part of the nonlinear susceptibility, depending on a phase factor caused by the laser propagation related to the position of QDs below the sample surface. Bias voltage dependent nonlinear absorption of both ensemble of and single IFQDs are presented with DR on the biased IFQD sample.

Based on the bias voltage dependent nonlinear absorption of IFQDs measured by DR, both the QCSE and VM is studied to improve the SNR and measurement speed of the voltage and wavelength dependent absorption map of single IFQDs. The QCSE in both the strong and weak regimes were observed in a single QD by DR measurements. VM was studied to measure the linear absorption of single QDs with high SNR and measurement speed. The physics of VM was discussed with numerical simulations to explain how to extract useful information form VM signal. Experimentally measured a VM signal matches the voltage wavelength dependent absorption map on a single IFQD.

To explore the spin relaxation time in semiconductors and the measurement of the signal below the apparent laser shot noise, spin relaxation based on noise fluctuations was studied. The physics of spin noise is studied as revealed by the Faraday rotation effect due to the oscillating magnetic field caused by electron spin relaxation. The spin noise spectrum gives a Lorentzian shape, providing information about the Larmor frequency and spin relaxation time. The spin noise measurement on an n-GaAs at different magnetic fields gives an electron g factor value about 0.45 and electron spin relaxation time about 45ns.

A comprehensive study of the effects of experimental parameters, including laser energy, intensity and temperature, on spin noise measurement, shows optical excitation induced spin relaxation. With a two level model with a Lorentzian line shape and saturation behavior, the absorption coefficients depends on both laser energy and intensity. Measured spin noise spectra show that the spin noise power is proportional to the absorption coefficient, and the spin noise width is related to the optically excited ionized impurity density.

8.2 Future directions

Our study of spin noise in n-GaAs proved that spin noise measurement can be a sensitive experimental technique to study spin dynamic in semiconductors. Beside the effects of laser energy and intensity on spin noise width, we studied excitation dependent relaxation, future work can be extended into QDs with micro-cavities to enhance the optical interaction strength (see below), a larger

laser energy range, various doping densities, and effects of external fields on the spin relaxation time.

Our study of the spin noise in n-GaAs involved using a spin noise technique to study the spin relaxation in QDs. We tried to measure the spin noise of ensemble and single QDs, but the efforts were not successful. The main challenge of a spin noise measurement on QDs is the lack of adequate QD density to interact with laser beam. Compared with 350μm thick n-GaAs, the spin noise signal strength for QDs with a thickness of a few ns will be five orders weaker, which is far beyond the current measurement sensitivity. Even for the 350μm n-GaAs, the spin noise measurement is challenging due to the fact that the spin noise signal strength is an order of magnitude below laser shot noise and electric thermal noise. There are two approaches to solve this problem in the future. One approach is to grow multiple layers of uniform QD. Unfortunately, QDs produced by current technologies probably are not sufficiently uniform due to the limitation of QD growth techniques. Progresses have been made to improve the uniformity of QDs. At present it would take 10^5 layers of uniform QDs with a thickness of hundreds of microns to enable measurement of the spin noise with similar signal strength as our n-GaAs sample. Another approach is to use a high finess optical cavity to increases interaction length. It has been reported that small Faraday rotation effects can accumulate in a Fabry-Perot cavity [1-3]. This approach will work not only for ensemble QDs, but also for single QDs. However, the Q of the cavity will have to be extremely high.

In our spin noise measurement, we have seen that optical excitation reduced the spin relaxation time due to optically excited impurity ionization. The two level model with a Lorentzian line shape and saturation behavior will not work for excitation near above the bandgap energy. It would be interesting to study the electron spin relaxation time in this laser energy range. Due to the strong absorption close and above the GaAs band gap, micron thick n-GaAs samples with optical surface quality are required. Such samples were not available to us.

Even though spin noise has the advantage of not disturbing the system under study, we have seen clear evidence of optical excitation induced spin relaxation in

the spin noise measurement on n-GaAs. The non-disturbing condition resulted from detuning away from the transparency regime, where the spin noise width is independent of the laser energy and intensity, as observed in the spin noise measurement in atoms. To get into the transparency regime, the detuning needs be on the order of tens times of the width of the Lorentzian shaped absorption. For n-GaAs, we expect to obtain a similar transparency with far below band gap detuning, which may give the ultimate spin relaxation time much longer than what we have measured. For example, by detuning the laser energy to 1.48eV, spin noise width of 1MHz, corresponding to a spin relaxation time about 220ns, was measured in an n-GaAs with similar doping density as our sample [4].

As a useful tool to study the spin relaxation time, the spin noise technique can be used to study the effects of external fields on spin relaxation. An external electric field caused by a bias voltage or optical field may affect the electron spin relaxation time. By measuring the spin noise width of n-GaAs under an electric field or pump laser beam, the effect of the external electric field on electron spin relaxation time can be studied.

Here we only measured the spin noise of a sample with a low doping density. It is possible that much longer spin relaxation time may exist for electron in ultra low doping density. A spin relaxation time about 17us been reported for an ultra low doping density n-GaAs through the Hanle effect [4]. Even spin relaxation time in n-GaAs with different doping density have been studied by Hanle effect, the actual spin relaxation time could be even longer due the possible side effect of the above bandgap excitation. With the advantage of not disturbing the system under study, the spin noise technique can provide reliable spin relaxation time measurements as a function of the doping density dependence.

The future of QD quantum computing is promising with the efforts and progress being made. The ultimate goal of building a functional optically driven QD quantum computer is an unknown long term goal that our group has pursued as scientific research. The final result may deviate from the original plan depending on technological development and need. The beauty is that the

knowledge we learn along the path may benefit the scientific community and society in a way we may not expect.

Bibliography

[1] D. Jacob, M. Vallet, F. Bretenaker, A. L. Floch, R. L. Naour., Small Faraday-Rotation Measurement with a Fabry-Perot Cavity, Appl. Phys. Lett., 66, 3546, (1995).
[2] Y. Li, D. W. Steuerman, J. Berezovsky, D. S. Seferos, G. C. Bazan, and D. D. Awschalom, Cavity enhanced Faraday rotation of semiconductor quantum dots, Appl. Phys. Lett., 88, 193126, (2006).
[3] J. Liu, K. Chang, Tunable giant Faraday rotation of exciton in semiconductor quantum wells embedded in a microcavity, Appl. Phys. Lett., 90, 061114, (2007).
[4] M. Romer, J. Hübner, M. Oestreich, Spin noise spectroscopy in semiconductors, Rev. Sci. Inst. 78, 103903 (2007).